TOWARDS ATOMISTIC UNDERSTANDING OF CATALYTIC NANOPARTICLES ON AMORPHOUS SUPPORTS

by

Christopher S. Ewing

Bachelor of Science in Chemical Engineering, Pennsylvania State University, 2010

Submitted to the Graduate Faculty of

the Swanson School of Engineering in partial fulfillment

of the requirements for the degree of

Doctor of Philosophy

University of Pittsburgh

2015

UNIVERSITY OF PITTSBURGH

THE SWANSON SCHOOL OF ENGINEERING

This dissertation was presented

by

Christopher S. Ewing

It was defended on

July 21st, 2015

and approved by

Albert Chi Fu To, Ph.D., Associate Professor, Department of Mechanical Engineering and Materials Science

Joseph J. McCarthy, Ph.D., W.K. Whiteford Professor, Department of Chemical and Petroleum Engineering

Götz Veser, Ph.D., Nickolas A. DeCecco Professor, Department of Chemical and Petroleum Engineering

Dissertation Director: J. Karl Johnson, Ph.D., Professor, Department of Chemical and Petroleum Engineering

TOWARDS ATOMISTIC UNDERSTANDING OF CATALYTIC NANOPARTICLES ON AMORPHOUS SUPPORTS

Christopher S. Ewing, PhD

University of Pittsburgh, 2015

Metal nanoparticles (NPs) have attracted considerable attention in heterogeneous catalysis due to their unique nanoscale properties. However, rational design and optimization of supported NP catalysts requires an accurate description of metal-support interactions, which can significantly impact NP stability and catalytic activity. The ability to calculate NP interactions with amorphous supports, which are commonly used in industrial practice, has been inhibited by a lack of accurate atomically-detailed models of amorphous surfaces.

We have developed an approach for constructing atomistic models of amorphous silica surfaces, using a combination of classical molecular modeling and density functional theory (DFT) calculations. To experimentally validate our model, we developed an emulsion synthesis procedure yielding mono-disperse 6 nm silica NPs, and a simple approach for high-yield separation of stable NPs from solution. Remarkably, our model accurately reproduces the experimental silanol number and silanol distribution over a wide temperature range, without any adjustable parameters.

We next developed a systematic approach for generating distributions of model NP/SiO_2 structures using the discrete element method in conjunction with DFT. Using these structures, we

studied NP-support interactions between amorphous silica and metal NPs ranging from 0.7 – 1.7 nm in diameter (13 – 147 atoms). Both NP adhesion energetics and charge transfer are local in nature, and depend on the silica hydroxyl density. Because surface hydroxyl content is directly dependent on temperature, our results suggest that both electronic charge and catalyst stability can be tuned via the silica pretreatment temperature, the latter of which we have experimentally validated using in situ X-ray diffraction. Finally, exploiting the local nature of NP-support interactions, we developed a method for predicting NP-support effects of different NP sizes and geometries based on correlations calculated for 13-atom NPs.

In this work, we show that an accurate atomistic description of not only amorphous surfaces, but also interactions between NPs and those surfaces can be achieved. Additionally, we developed a similar method for generating model systems of single-atom catalysts on amorphous supports. Insights into the role of catalyst-support interactions on catalyst structure and function gained from these atomistic models may serve to guide the design/optimization of catalytic materials.

TABLE OF CONTENTS

LIST OF TABLES

LIST OF FIGURES

PREFACE

I am extremely grateful to many people who made this work a success. I would like to thank my advisors for their guidance, insight, and motivation. Dr. J. Karl Johnson helped me to stay continuously focused, specifically by questioning my questioning with “what’s your hypothesis?” Dr. Götz Veser was never without a new idea or perspective, and pushed me to always connect individual results to practical importance. Dr. Joseph J. McCarthy always kept my general studies in perspective, and pushed me to investigate for the sake of learning.

I am very grateful to Dr. Daniel S. Lambrecht for taking the time and effort to work closely with me in developing a project that would become half of my dissertation. I thank Dr. Albert To for taking the time and effort to read, listen, and provide helpful comments that enriched the quality of this work.

I am very grateful to all of the graduate and undergraduate students that have helped to make this work a success. In particular, I want to thank Dr. Saurabh Bhavsar for teaching me so much in the laboratory and Yung-Chieh Lai for experimental advice and excellent characterization of materials that contributed greatly to this work.

Finally, I want to thank my family, whose infinite patience and understanding are the foundation for my success. My wife Valerie, and my kids Autumn and Owen, have provided the support, inspiration, and motivation required for true success.

1.0 INTRODUCTION

Catalysis is responsible for essentially all transportation fuels and most chemicals produced today.[1] Scientific advancements in both computational methods[2-8] and experimental characterization techniques[9-11] have recently begun to enable the development of catalytic materials by rational design. Because catalysis occurs on atomistic length scales, an atomistic understanding of catalytic materials offers great promise for the tailoring of improved or even novel catalytic materials. Supported nanoparticle catalysts hold great potential as highly active stable catalyst materials. Significant advances in computational materials science over recent decades have provided atomistic-level understanding of numerous catalytic materials;[7,11-17] however, such studies of supported catalysts have been limited to idealized, perfectly crystalline supports.[18-22] Although amorphous oxides are widely used as catalyst supports, their lack of long-range order poses a major challenge to accurately describing such surfaces with atomistic resolution.

1.1 AMORPHOUS SILICA

Amorphous silica is an abundant material with a wide range of applications including pharmaceuticals,[23] optics,[24,25] coatings,[26] and biosensors.[27] It is also widely used as a catalyst support due to good thermal stability, ease of production, and tunable surface area. [28,29] An

accurate description of the amorphous silica surface could aid in the understanding and development of supported catalysts; however, such a description is beyond experimental capabilities due to the absence of both long-range order and electrical conductivity.[30-33] Despite this limitation, experiments have provided a wealth of information regarding the nature of amorphous silica surfaces.

Silanol groups are formed during the synthesis of amorphous silica and can also be produced by reaction of siloxane bridges (≡Si-O-Si≡) with water.[33] Experiments have shown that both surface hydrophobicity and reactivity are dependent on silanol content. [2,34] Surface silanols can be differentiated based on both hydrogen bonding status and number of OH groups per silicon atom. For the purpose of experimental observation these have been classified (Figure 1.1) as isolated (free single silanols), ≡SiOH; geminal free (silanediols), $=Si(OH)_2$; and vicinal (H-bonded single or geminal).[33]

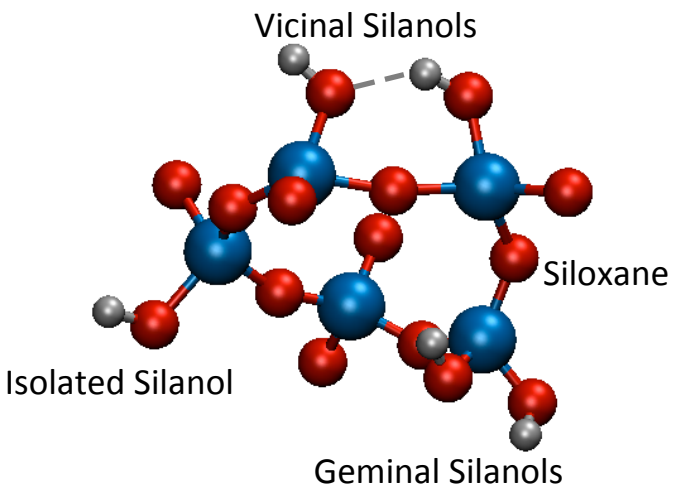

Figure 1.1. Classification of surface groups on amorphous silica.

Upon heating, silanol groups are known to react with one another to form a water molecule and a siloxane bridge in a process known as dehydroxylation. Even for samples of widely varying specific surface area and synthesis procedure, the surface silanol density (silanol number (OH nm^{-2})) and distribution of silanol types depend quite predictably on temperature. [33,35,36] Hence while the atomic structure of the silica surface is not known, a number of predictable descriptors have been measured.

The absence of long-range order has long been a stubborn barrier to accurately modeling the structure and energetics of amorphous materials.[37] Recent advances in computing power, improved parallelization, and algorithm development have allowed for systems of ever-increasing size to be studied using *ab initio* methods. As a result, attempts have been made at using DFT calculations to model the surface of amorphous silica, providing valuable insight

regarding the local structure and energetics of surface features.[30-32] However, despite the accomplishments of recent studies no single surface model has been able to accurately describe the evolution of amorphous silica surfaces upon heating.

1.2 SUPPORTED CATALYSTS

Metal nanoparticles (MNPs) have attracted considerable attention in the field of heterogeneous catalysis due to their large surface-to-volume ratios and low-coordinated active surface sites.[13,16,28,38-44] These MNPs are typically immobilized on oxide supports, which can affect the activity and selectivity of the MNPs by altering their morphology and electronic structure.[13,41-43,45,46] As pointed out by Norskov et al.,[7] there is a critical need for a fundamental atomic-scale understanding of catalyst-support interactions because they can dramatically impact the electronic properties of the supported MNP. The majority of computational catalysis studies have used extended surfaces or unsupported NPs as model catalyst particles.[41,44,47] Atomistic studies of supported catalysts have been limited to MNPs supported on ideal surfaces with point defects.[20,45,46] Technical catalysts used in industry, however, are not ideal and many oxide supports are typically used in an amorphous state.[48] The ability to calculate MNP interactions with amorphous supports, however, is hampered due to a general lack of accurate atomically detailed models of amorphous surfaces.

2.0 ACCURATE AMORPHOUS SILICA SURFACE MODELS FROM FIRST PRINCI-PLES THERMODYNAMICS OF SURFACE DEHYDROXYLATION

The content of this chapter is taken from C. S. Ewing, S. Bhavsar, G. Veser, J. J. McCarthy, and J. K. Johnson, "Accurate Amorphous Silica Surface Models from First-Principles Thermodynamics of Surface Dehydroxylation" *Langmuir* 18 (2014) 5133-5141.

2.1 INTRODUCTION

The advances in computational materials science over recent decades have resulted in the availability of accurate models for a wide range of crystalline materials. While this had a profound impact on our capability to computationally screen and predict physical and chemical properties of crystalline materials,[7,49,50] many materials, oxides in particular, are utilized in technical practice in their non-crystalline amorphous state. The lack of long-range periodicity of amorphous surfaces, however, poses a major challenge in accurately describing such surfaces computationally and hence has largely precluded the use of computational models for advancing our understanding and development of this important class of materials. Silica is a typical example from this class of materials; it is an abundant material with a wide range of applications including pharmaceuticals,[23] optics,[24,25] catalysis,[51] coatings,[26] and biosensors.[27] Surface properties dictate the reactivity and hydrophobicity of amorphous silica.[52] An accurate atomistic

description of the surface is therefore central to the development of applications involving amorphous silica. For example, accurate models of *amorphous* silica surfaces are prerequisite to the reliable study of metal-support interactions for realistic silica supported catalysts. Due to its amorphous nature, however, the microstructure of such surfaces is difficult to obtain experimentally.[30-32,52] While model surfaces of crystalline materials can be constructed via cleavage of the bulk structure obtained using X-ray scattering techniques, the lack of long-range order prohibits this approach for amorphous materials.[31] Despite this limitation, experiments have provided significant information regarding the nature of amorphous silica surfaces.

2.1.1 What we know from experiments.

Silanol groups are formed during the synthesis of amorphous silica and can also be produced by reaction of siloxane bridges (≡Si-O-Si≡) with water.[52] Experiments have shown that both surface hydrophobicity and reactivity are dependent on silanol content. For example, the rate of deposition and quality of Al_2O_3 films grown on wet silicon oxides has shown dependence on the surface silanol content.[2,34]

The surface of amorphous silica exhibits a diverse range of features ranging from siloxane bridges to hydrogen bond networks between multiple silanols. Surface silanols can be classified as single, meaning that there is a single OH group on a Si atom, or geminal (twin) indicating two OH groups bound to the same Si atom. Each silanol can be further designated as free, indicating not hydrogen bonded to other OH groups, or vicinal (proximate), meaning the OH group is hydrogen bonded to a neighbor. For the purpose of experimental observation these have been classified as isolated (free single silanols), ≡SiOH; free geminal (silanediols), $=Si(OH)_2$; and vicinal (either single or geminal).[52]

Upon heating, silanol groups are known to react with one another via condensation to form a water molecule and a siloxane bridge. This process is known as dehydroxylation. Due to the hydrophilic nature of silanols, amorphous silica adsorbs a significant amount of water. Zhuravlev determined that physisorbed water is completely removed at 190 ± 10 °C, after which dehydroxylation begins to occur.[52-54] Total surface silanol content is typically referred to as the silanol number (OH nm^{-2}). Using the deuterium exchange method, silanol number as a function of temperature in vacuum has been reported for many different amorphous silica samples. Remarkably, despite widely varying specific surface areas and disparate synthesis procedures, a suite of experimental studies of amorphous silica have shown that this material exhibits very consistent temperature-dependent silanol numbers, as shown in Figure 2.1.[52] By combining IR and ^{29}Si NMR spectroscopies and the deuterium exchange method it has been shown that the distribution of silanol types, as a function of temperature is likewise highly consistent across a wide range of amorphous silica samples.[35,52-55] Moreover, the energy of dehydroxylation must be a strong function of the chemical microenvironment of the surface, because otherwise dehydroxylation would occur over a narrow temperature range, instead of over a considerably wide range as seen in Figure 2.1. *Hence, the thermodynamics of dehydroxylation, i.e., the temperature dependences of the silanol number and distribution of silanol types, are key descriptors of the microstructure, and thus the physics and chemistry of amorphous silica surfaces.* Thus, it is necessary for any accurate model of amorphous silica to be able to predict the silanol number and distribution of silanol types as functions of temperature.

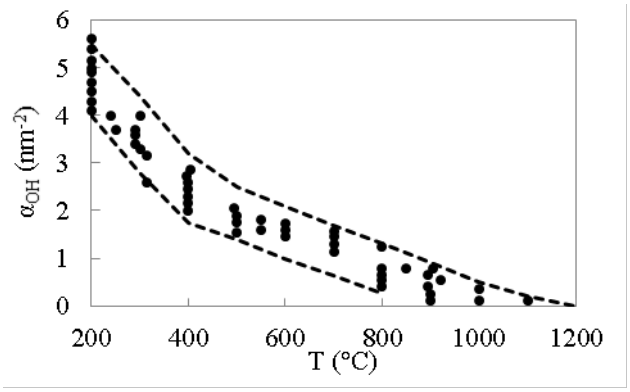

Figure 2.1. Experimentally measured silanol number as a function of temperature for 16 samples having different synthesis procedures and specific surface areas spanning 9.5 – 905 m^2/g.[52]

2.1.2 Previous Amorphous Silica Surface Models.

The absence of long-range order is a persistent barrier to accurately modeling the structure and energetics of amorphous materials.[56] While there are a number of force fields developed for silica systems,[57-65] to the best of our knowledge, none have been parameterized to account for the structure and energetics of amorphous silica throughout the process of dehydroxylation. Recent advances in computing power, improved parallelization, and algorithm development, however, have allowed for systems of ever-increasing size to be studied using *ab initio* methods. As a result, attempts have been made at using density functional theory (DFT) calculations to model

the surface of amorphous silica, providing valuable insight regarding the local structure and energetics of surface features.[30-32] Tielens and co-workers developed a model of the surface of amorphous silica by cutting a slab from a model of bulk amorphous silica that had previously been generated using molecular dynamics (MD) simulations using classical model potentials. They subsequently saturated all dangling bonds on the cleaved surface with terminating hydroxyl groups, and finally relaxed the system using DFT calculations.[31] While their model reproduces the silanol number for fully hydroxylated silica fairly well, it does not account for the temperature dependence of the silanol number and the silanol distribution was not compared to experimental data. Ugliengo and co-workers constructed a more comprehensive model, including multiple degrees of silanol coverage.[32] They first generated a fully hydroxylated slab of amorphous silica, similar to Tielens *et al.,* and incrementally condensed nearest silanol neighbors. While intuitive, this methodology does not follow correct physics, as we show in this work that the nearest neighbors do not always have the lowest dehydroxylation energy. Furthermore, the model lacks a connection between model state and system temperature. Rozanska and co-workers postulated that amorphous silica could be modeled as a combination of the (100), (101), and (111) surfaces of crystalline silica (β-cristobalite).[30] They used this approach to model the dehydroxylation of amorphous silica surfaces.[30] Adapting a statistical thermodynamics model originally developed for alumina surfaces,[66] individual dehydroxylation steps were directly related to system temperature and the partial pressure of water via the Gibbs free energy of reaction. Their model was able to correlate experimental silanol numbers as a function of temperature fairly well by taking a linear combination of the three surfaces with adjustable parameters for the weighting of each surface at each temperature. However, their model not only lacks any information on the actual structure of the amorphous silica surface

(since they use crystal surfaces as a surrogate), but it also yields no predictive power due to the *a posteriori* fitting.

2.1.3 Significance.

Despite the accomplishments of recent studies, no surface model has been experimentally confirmed to accurately represent the microstructure of the real amorphous silica surface. Indeed, it seems unreasonable to expect that a periodic atomistic model of a few square nanometers can accurately represent amorphous macroscopic surfaces, with their attendant heterogeneity. However, as noted above, the nearly universal behavior of the silanol number as a function of temperature for a wide range of amorphous silica samples[52] provides some evidence that a reasonably simple model may be achievable.

It is known from experiments that dehydroxylation of the silica surface occurs over a wide range of temperatures,[52] indicating that the enthalpy of each dehydroxylation step is highly dependent on the microscopic environment of the surface. Therefore, an atomistic model that accurately describes the temperature dependence of the silanol number should also accurately describe the surface microstructure. We thus constructed amorphous silica surface models by using both DFT and empirical models to generate a series of candidate surfaces and used these surfaces to simulate the thermodynamics of dehydroxylation, a process that can be easily validated experimentally. Using this methodology, we have generated reliable and *predictive* models of amorphous silica surfaces for a range of temperatures. Moreover, we have demonstrated that a small periodic atomistic model of the amorphous silica surface can accurately represent the physics and chemistry of the real surface, as characterized by

macroscopic measurements of the temperature dependence of the silanol number and silanol type.

2.2 MODELING AND EXPERIMENTAL METHODS

2.2.1 Generation of Amorphous Silica Surfaces.

A model of bulk amorphous silica was constructed using a reactive potential for silica and water, ReaxFF,[60,67] that allows for bond breaking and bond formation events. The simulations were carried out using the LAMMPS molecular dynamics engine.[68] The ReaxFF potential was parameterized using quantum mechanics calculations considering both reaction barriers and equilibrium configurations. Simulations were carried out in the constant temperature, constant volume ensemble with a timestep of 0.5 fs. We started with quartz structures using a supercell with dimensions of 23.742 Å × 18.276 Å × 17.404 Å containing 456 atoms and a modified lattice constant corresponding to the density of amorphous silica reported using this force field (2.14 g/cm^3). [60,67] Similar to Fogarty et al.,[60] the system was then annealed at 4000 K for 75 ps during which the system reached sufficient mobility to eliminate any artifacts due to the original modified quartz structure. The system was then simulated for an additional 50 ps at 4000 K during which snapshots of the system configuration were taken every 10 ps. The mobility at this high temperature allowed for sufficient diffusion of atoms to produce 5 independent structures (see Figure A1.5). The configurations from each of the five snapshots were then cooled from 4000 K to 300 K at a rate of 25 K/ps followed by energy minimization using a conjugate gradient algorithm, resulting in a family of model bulk amorphous systems. This annealing procedure

allows for overcoming potential barriers that simple relaxation would encounter, making it more likely to identify near-ground state energies, but this method does not guarantee finding ground state structures. Mass density, bond lengths, and bond angles of the bulk periodic systems showed good agreement with previous ab initio calculations and experimental observations (see Table A1.1).

Each bulk system was then used to generate a surface slab by removing all atoms with a Z-value greater than 7.5 Å. We made the bulk systems 10 Å larger than the resulting slab in the Z-dimension in order to mitigate the interaction between the top and bottom surfaces of the slab. The surfaces were hydroxylated by saturating *all* under-coordinated Si atoms with O atoms followed by saturation of all under-coordinated O atoms with H atoms. We did not consider the presence of surface defects, e.g. dangling oxygen bonds, because they are very rare at the low temperatures of the systems we are modeling.[69] This approach avoids the need for resolving surface defects present following bulk cleavage.[69,70] Our purpose is to generate accurate structures of precipitated amorphous silica surfaces in contact with (low humidity) gas phases, as commonly encountered in applications such as catalyst supports. We therefore do not consider surface ionization, which is important for silica-water interfaces,[65,71-73] because surface ionization is highly improbable for solid-gas interfaces. The hydroxylated structure was fully relaxed using a conjugate gradient algorithm within the CP2K code.[74-78] The code employs a Quickstep[78] implementation of the DFT method using pseudopotentials and planewaves as well as localized Gaussian basis sets. Goumans *et al.* showed that a slab that is 11.25 Å thick is sufficiently thick to represent a quartz surface and that the PBE functional more accurately describes hydrogen bonded silica surfaces than B3LYP.[79] We used hydroxylated surface slabs approximately 12 Å thick and consisting of almost 300 atoms in this work. All calculations with

CP2K used the PBE functional[80] and GTH pseudopotentials[81,82] in conjunction with triple-ζ basis sets with polarization functions (TZVP).[83] We used a 350 Rydberg cutoff energy for the plane wave basis set. All surface slabs were relaxed using CP2K treated as periodic in the X, Y and Z directions with at least 15 Å of vacuum between the slab surfaces in the Z direction. Validation of the planewave energy cutoff, slab thickness, XY dimensions, and vacuum spacing can be found in the appendix (Figures A1.1, A1.2, A1.3, and A1.4 respectively).

2.2.2 Synthesis and Characterization of Silica Nanoparticles.

We adapted the procedure of Wang et al. for synthesis of silica nanoparticles with low polydispersity.[84] Briefly, a catalyst stock solution was prepared by mixing ammonia with water to a pH of 11.4. 2.6 g of tetraethyl-orthosilicate was diluted in 5 ml ethanol, mixed thoroughly, and added to 34.75 g of catalyst stock solution. The solution was then stirred for 3 hours at 60 °C. The resulting nanoparticles were then separated from solution, dried, and calcined at 350 °C. Finally, the particles were soaked in water for 24 hours at room temperature in order to re-hydroxylate the surface. Further details of the synthesis procedure can be found in the appendix.

Transmission electron microscopy (TEM) images were taken on a JEOL JEM2100F with an accelerating voltage of 200 keV. Specific surface area was measured by nitrogen adsorption using a Micromeritics ASAP 2020. The surface area of N_2 was taken to be 1.47 nm^2/mol as determined previously.[85] Weight loss as a function of temperature was measured using a thermogravimetric analyzer (TGA). Details of the TGA procedure used can be found in the appendix.

2.3 RESULTS AND DISCUSSION

2.3.1 Simulating Dehydroxylation.

Experiments have shown that the kinetics of dehydroxylation is sufficiently fast that the state of surface silanols can be described thermodynamically.[52] In order to accurately model dehydroxylation we first determined which silanols would condense from each of our five model surfaces and in what order. The distance between silanols must be small enough to allow for a siloxane bridge to form between the two Si atoms involved (Figure 2.2a). Due to local structural rearrangement upon dehydroxylation, this distance can be significantly larger than the length of the resulting siloxane bridge. Based on the results of preliminary studies, we considered silanol pairs with Si-Si and O-O distances of less than 5.5 and 4.5 Å, respectively. We found that distances larger than these did not give realistic ending structures. For each such silanol pair, we found the enthalpy of reaction (dehydroxylation energy) by facilitating the condensation of water in the following manner: 1. The OH groups were removed and a single O atom was placed at an estimated equilibrium position, based on known bond lengths and angles (Figure 2.2b). 2. Siloxane bridge formation was then facilitated by fixing the position of the inserted O atom while relaxing only the two participating Si atoms and their nearest neighbors (including hydrogens when the nearest neighbor was an OH group). In order to reduce computational cost we performed these constrained relaxations using ReaxFF to provide reasonable starting points for subsequent relaxations with DFT. The inserted O atom was fixed to avoid the formation of defects that result when only one Si-O bond is formed (i.e., one dangling oxygen and one undercoordinated Si atom). We restricted this relaxation to only participating Si atoms and nearest neighbors because the slight error of ReaxFF bond lengths and angles cause the

subsequent DFT relaxation to take longer. 3. After siloxane bridge formation we allowed the O atom to relax as well as participating Si atoms and nearest neighbors (still fixing all other atoms). This was done because the siloxane bridge structures were often high energy under the constraints used to facilitate their formation. 4. The entire system was then fully relaxed using DFT (Figure 2.2c).

An alternate approach is to use ReaxFF to perform all relaxations and energy calculations. We tried this approach and found that while the geometries were qualitatively correct, the calculated enthalpies of dehydroxylation using only ReaxFF were both quantitatively and qualitatively incorrect (see Figure A1.6), demonstrating the need to use DFT for generating accurate results.

We applied this procedure to every silanol pair within our distance criteria and calculated the corresponding dehydroxylation energy, ΔE_{DFT}, for removing only that pair by:

$$\Delta E_{DFT} = E_f + E_{H_2O} - E_0, \qquad (2.1)$$

where E_0 and E_f are the DFT energies of the system before and after the silanol pair dehydroxylation, respectively, and E_{H_2O} is the DFT energy of an isolated water molecule calculated using the same parameters (size of supercell, energy cutoff, etc.) as the silica slab systems. We then selected the silanol pair with the lowest (most favorable) dehydroxylation energy and assumed that this pair condenses first on the surface. The post-condensation relaxed system for this lowest energy silanol pair then serves as the starting point for the next step in the dehydroxylation process.

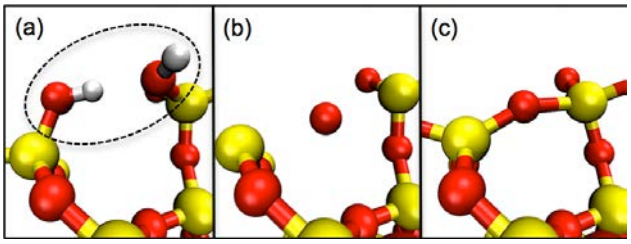

Figure 2.2. Procedure for simulating dehydroxylation. (a) Silanol groups within range to condense are identified. (b) OH groups are removed and an oxygen atom is inserted at an estimated equilibrium position. (c) First and second neighbors are relaxed with ReaxFF to form a siloxane bridge, followed by relaxation of the entire system with DFT.

A simple approach would be to calculate the dehydroxylation energies for each silanol pair on the surface and assume that these energies are independent of one another. We have found, however, that the energetics of dehydroxylation can be significantly affected by the presence or absence of neighboring silanols (see Figure A1.3). We therefore simulated the condensation of every available silanol pair, as described above, for each dehydroxylation step. This procedure gives models of the silica surface for a range of silanol numbers, as shown for one of the five model surfaces in Figure 2.3. One might assume *a priori* that silanol pairs that are farther apart would have higher dehydroxylation energy; this is the approached used by Ugliengo et al. for determining the order of silanol pairs that condense.[32] However, we found only a weak correlation between silanol separation and dehydroxylation energy, as illustrated in Figure A1.7. Therefore, a rigorous approach must explicitly compute (and recomputed) the dehydroxylation energy, as included in our approach.

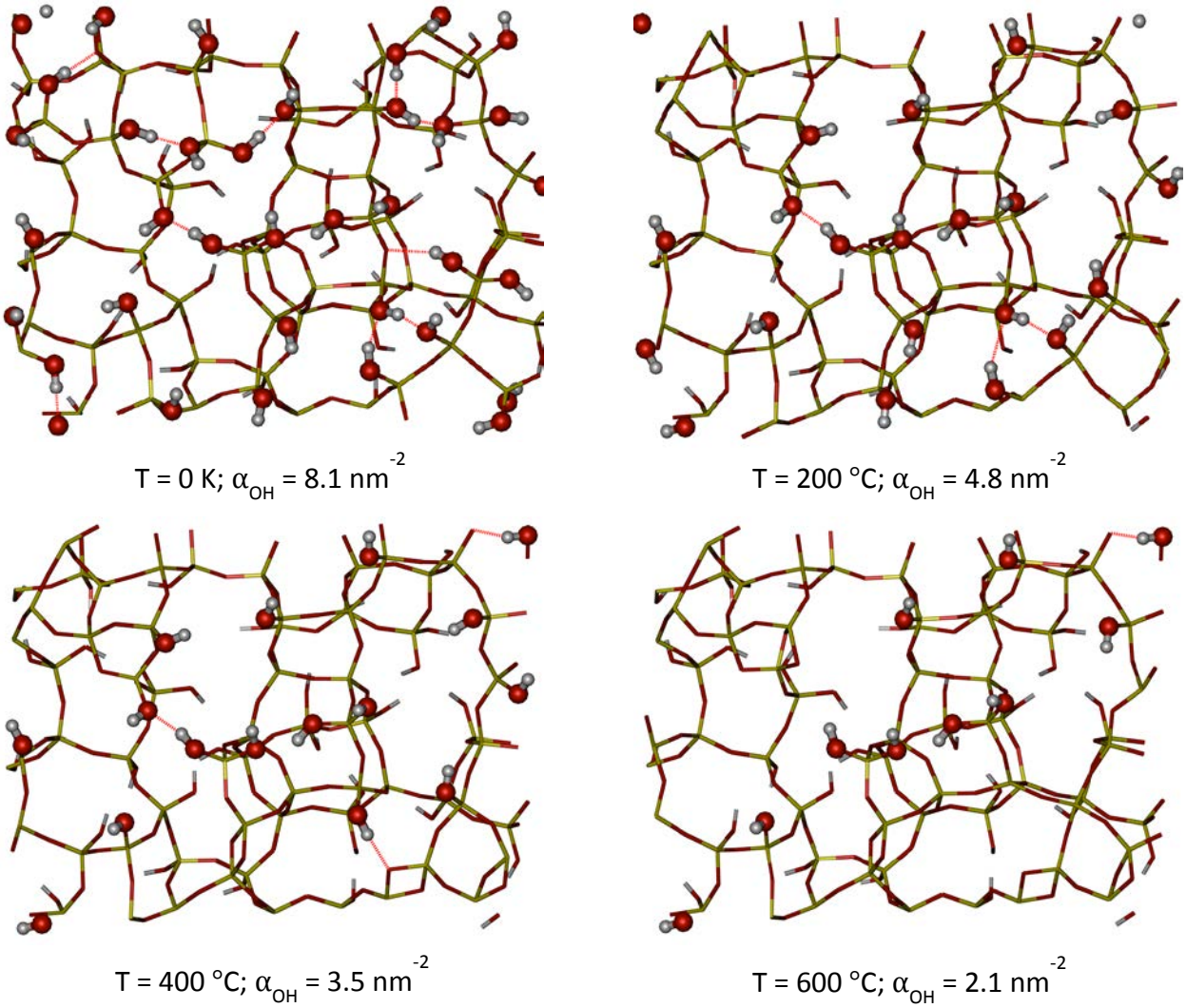

Figure 2.3. Representative images of amorphous silica surface models (surface E of Figure 2.4) at various temperatures. Silanols on the top surface are depicted with space filling models; only the bonds between the remaining atoms are shown. Hydrogen bonds are shown as pink lines. As temperature is increased silanols condense and the surface begins to exhibit small hydrophobic regions (containing no silanols). Hydrogen bonding silanols are removed at lower temperatures.

2.3.2 Statistical Thermodynamics Model.

The different surface silanol coverages of our model can be connected to the physical conditions of a real system by implementing a thermodynamic model similar to those used for alumina and crystalline silica surfaces.[30,86-88] The Gibbs free energy of dehydroxylation for the removal of two silanols in the form of one molecule of water vapor is given by:

$$\Delta G_{rxn} = \Delta E_{\mathrm{DFT}} - kT\ln\left(\frac{kTq_r}{P_{\mathrm{H_2O}}\Lambda^3}\right) \tag{2.2}$$

where ΔE_{DFT} is the reaction energy computed from DFT given by eq 1, $P_{\mathrm{H_2O}}$ is the partial pressure of water, and q_r and q_t are the translational and rotational partition functions of water in the ideal gas state, respectively. Here we make the approximation that the dehydroxylation process does not significantly change the phonon modes and density of states of the surface (see appendix for a detailed derivation). While this assumption is not strictly valid, the resulting error is expected to be less than the errors inherent in DFT. Moreover, this approximation has been found to be reasonably accurate for β-cristobalite surfaces and should hold true for amorphous silica as well.[30]

2.3.3 Accurate Reproduction of Experimentally Measured Silanol Number.

It is not obvious *a priori* that a small surface slab can adequately represent the complexity of a macroscopic amorphous surface. We therefore constructed five independent initial surface

configurations as described above in order to capture a wider range of surface heterogeneity. Surprisingly, we found that all five independent surface models exhibit temperature dependence of the silanol numbers that are in close agreement with each other and with experimental data reported in the literature,[52] as can be seen in Figure 2.4a. This is a remarkable and unexpected outcome. Significant deviation between surfaces at low temperatures, specifically between surface E and the others, is due to the random nature of the annealing and cutting procedures. As experimentally relevant temperatures are approached, however, discrepancy between surface models is significantly reduced. The procedure for computing the silanol number is described in detail in the appendix.

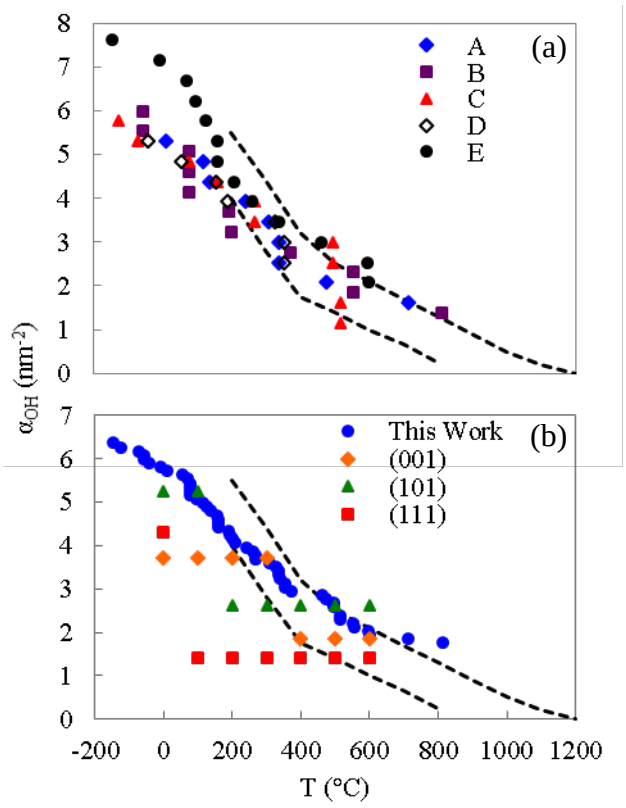

Figure 2.4. Silanol number as a function of temperature for (a) the five individual surfaces of this study (labeled A-E) and (b) the average of all surfaces compared with surfaces of β-cristobalite calculated previously.[30] (P_{H_2O}=10^{-6} bar) Dashed lines indicate the bounds for 16 disparate samples reported in the literature.[52]

In order to obtain an "average" surface, we analyzed the five model surfaces in combination. This was done by summing the number of silanols across all five surfaces for a given temperature and dividing by their combined surface area. Physically, this is analogous to measuring the silanol number of five distinct areas on a single sample and averaging them. Our

model shows excellent agreement with experimentally measured silanol numbers from the literature, as shown in Figure 2.4b. The silanol numbers for individual surfaces of β-cristobalite are also plotted in Figure 2.4b. Here we see very poor agreement for any one of the individual crystal surfaces with experiments, indicating that crystalline surfaces are not valid representations of amorphous silica surfaces. The correct trend of silanol number with temperature can only be reproduced by a linear combination of the three crystal surfaces with ad-hoc weighting of each surface at each temperature. Our model requires no such weighting and no adjustable parameters. In fact, in our approach the only model parameter not derived from first principles is the partial pressure of water, P_{H_2O}. We chose a value corresponding to high-vacuum conditions consistent with experiments and found that the silanol number is not particularly sensitive to this parameter in the range of conditions used for experimental dehydroxylation measurements (Figure A1.8).

Experimental studies have concluded that vicinal silanols are completely removed at around 400 °C.[52] The dehydroxylation of the remaining (isolated) silanols has been attributed to proton mobility across the surface at higher temperatures, which is not included in our thermodynamic model. Based on this explanation, we expect to see significant deviation between our model and experiments above 400 °C. Our results suggest, however, that significant proton mobility may not be needed to explain experimental observations until above 600 °C, as seen in Figure 2.4b. We therefore expect that our model may not be accurate above about 600 °C because we do not account for proton mobility.

Following Rozanska et al.,[30] we derived a silanol stability diagram from which the silanol number can be predicted based on only system temperature and partial pressure of water (Figure 2.5). This was done by recalculating silanol number vs. temperature for a very wide range of P_{H_2O}

values. The diagram can be interpreted as a silanol coverage landscape where the steepness of the silanol number vs. temperature curve is described by the color gradient.

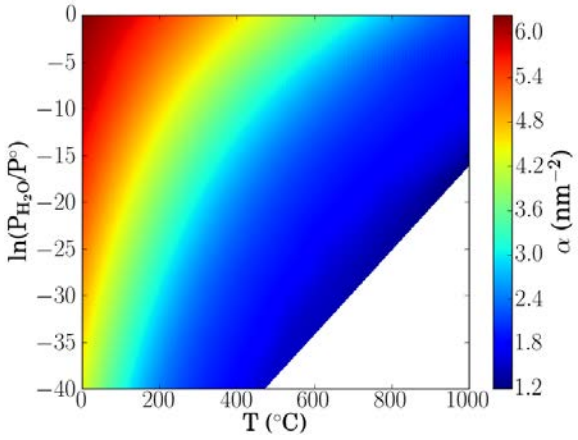

Figure 2.5. Silanol number as a function of temperature and partial pressure of water. The white area indicates no silanol groups are within range to condense directly.

2.3.4 Accurate Reproduction of Measured Silanol Distribution.

Along with silanol number, we quantified the silanol distribution for each model surface after every dehydroxylation step. Our model is again in good qualitative agreement with experiments[52] and is the first such rigorous comparison over a range of temperatures (Figure

2.6). Furthermore, silanol distributions for the individual (*i.e.*, non-averaged) model surfaces also agree quite well with experiments (Figure A1.9).

Significant quantitative error between isolated and vicinal silanols is evident below 400 °C. This is likely due to differences in how the silanol types were defined in experiment and computation. We defined vicinal silanols as exhibiting a hydrogen bond with another silanol, where the hydrogen bond is defined as having O-O distance < 3.5 A and H-O-H angle > 110 °, based on general findings reported by IUPAC.[89] Experimentally, isolated and vicinal silanols are differentiated based on their IR frequencies. This requires significant approximation, however, as the relative proportions of IR modes must be deconvoluted from a single spectrum and the frequencies assigned to isolated and vicinal silanols vary in the literature.[90-93]

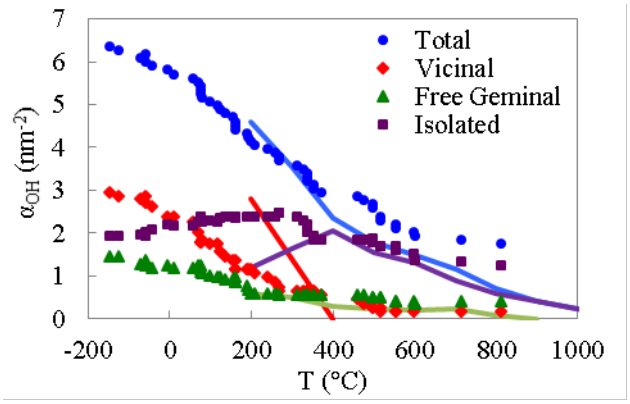

Figure 2.6. Distribution of silanol groups as a function of temperature (P_{H_2O}=10^{-6} bar) for simulation results (points) and experimental averages[52] (lines).

2.3.5 Dehydroxylation of Silica Nanoparticles.

We synthesized silica nanoparticles in order to conduct further comparisons between experimental observations and our model. Very small (~6 nm) silica particles were chosen for the comparison due to their large surface-to-volume ratio, *i.e.* the particles are sufficiently small that their behavior is dominated by their surface properties and yet large enough to exclude pronounced "nanosize effects". Furthermore, the extensive experimental studies by Zhuravlev and coworkers[52] showed that the temperature dependence of the silanol number is consistent across a very wide range of surface areas (see Figure 2.1). This indicates that curvature of the surface has a secondary effect on silanol number because samples with varying (high) surface area would necessarily exhibit significant local curvature differences due to the variety of porosities reported. Nevertheless, all of these varied experimental surfaces result in consistent silanol numbers. Analysis of TEM images and the N_2 adsorption isotherm indicated that the nanoparticles were non-porous (Figure 2.7a). Measured silanol numbers were within the range of values reported in the literature[52] and are thus consistent with a silica sample containing only surface silanols. (The procedure for calculating silanol numbers from TGA curves is described in the appendix.)

Silanol numbers observed for our nanoparticles are in good qualitative agreement with our model, as seen in Figure 2.7b. Most notably, the slope decreases at both high and low temperatures. The change in slope at high temperature has previously been attributed to an increase in the activation energy of dehydroxylation due to the requirement of proton mobility for condensation of isolated silanols to occur (as previously mentioned).

The flattening of the slope at low temperatures has only been reported in more recent studies, likely owing to significant advances in instrument sensitivity.[94-96] Unfortunately, the

majority of knowledge regarding the fundamentals of silanol interactions was determined from much older studies, and no explanation for this effect can hence be found in the literature.[52] However, the source of the decrease in slope at low temperature can now be explained by examining our model surfaces.

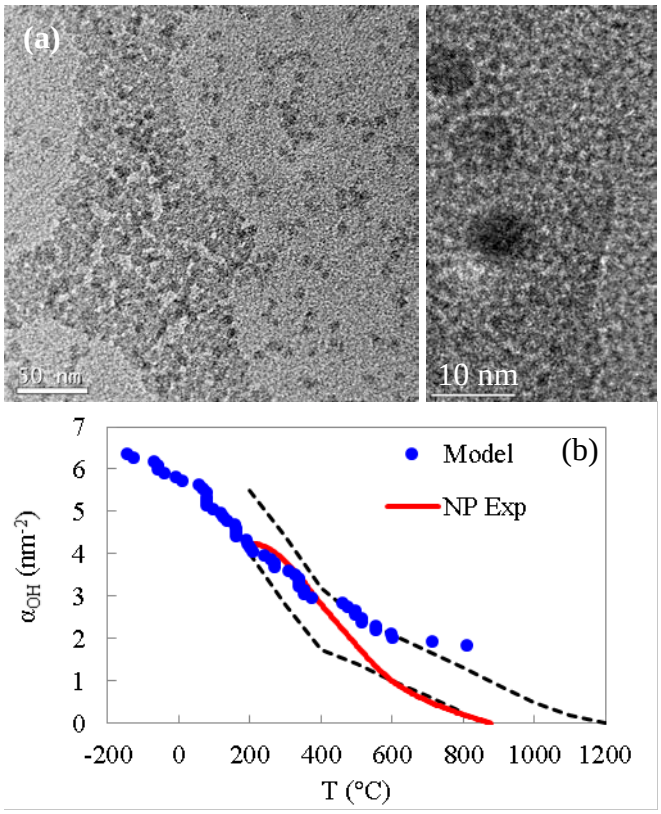

Figure 2.7. Experimental data for silica nanoparticles used in this study. (a) TEM images showing uniform size (left) and spherical shape (right). Particle diameter is ~6 nm, corresponding to a specific surface area (SA) of 460 m^2/g (assuming spherical shape and a density of 2.2 g/cm^3). SA = 488 m^2/g as measured by the BET method. (b) Silanol number as a function of temperature measured for 6 nm silica nanoparticles (solid line) and calculated from our model surfaces (points) assuming $P_{H_2O}=10^{-6}$ bar. Dashed lines indicate the bounds reported in the literature.[52]

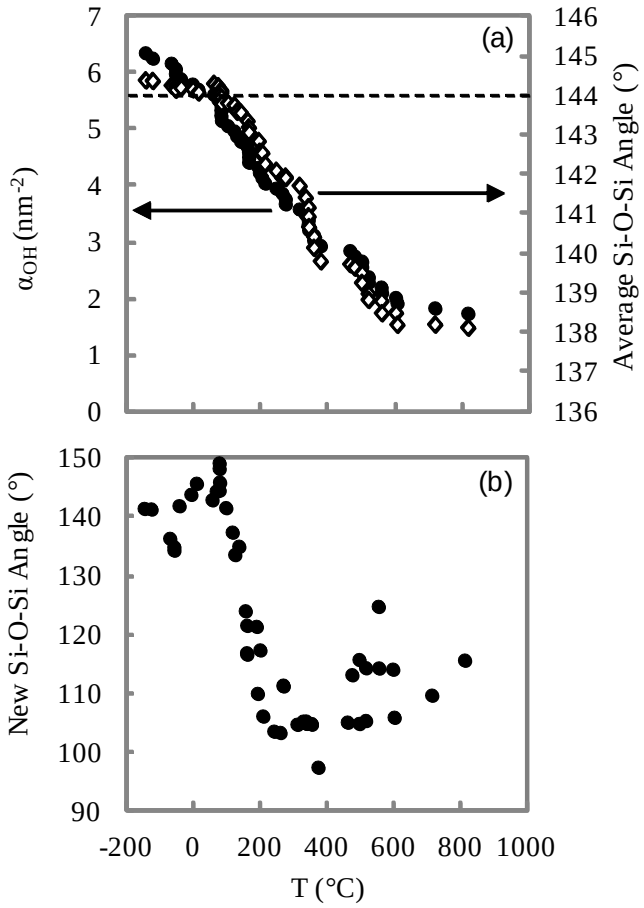

Figure 2.8. (a) Silanol number (filled circles) and average angle of existing Si-O-Si bridges (open diamonds) and (b) Si-O-Si angle of newly formed siloxane bridges, as a function of temperature. Dashed line indicates the equilibrium Si-O-Si bond angle for α-quartz (144 °), the most thermodynamically stable silica polymorph.

The slope of the silanol number curve depends on the energetics of dehydroxylation as a function of temperature. A Van't Hoff plot clearly indicates a significant temperature dependence of the dehydroxylation energy (Figure A1.10). This temperature dependence along with the widely varying energies of dehydroxylation for different silanol pairs on the surface (Table A1.2) indicates a relationship between the silanol number as a function of temperature and the local environment on the surface. Indeed, we observed a direct correlation between the average Si-O-Si angle and silanol number, shown in Figure 2.8a. As dehydroxylation proceeds, the average Si-O-Si angle diverges from the equilibrium value, indicative of a buildup of stress with decreasing silanol number, resulting in an energy penalty (stress penalty) for dehydroxylation. Changes to the average Si-O-Si angle upon dehydroxylation are not explained by simply accounting for newly formed siloxane bridge angles (Figure 2.8b). This indicates that the stress associated with the dehydroxylation of a single silanol pair is propagated non-locally throughout the silica network via significant restructuring of surrounding atoms. This is not as prevalent at low temperatures, however, where the slope of the silanol number curve appears to flatten. Both the average Si-O-Si angle and the angle of newly formed siloxane bridges remain fairly constant below ~50 °C. These observations are consistent with low-temperature silanols existing in a configuration that allows for condensation and siloxane bridge formation without significant stress to surrounding bonds.

We found that every dehydroxylation step that occurred under T = 50 °C involved at least one geminal silanol and all steps below T = 0 °C occurred exclusively between geminal silanols. Geminal silanols are anchored to the surface by only two siloxane bridges, in contrast to single silanols, which are anchored by three. As a result, geminal silanols have more freedom to rearrange during siloxane bridge formation than single silanols. The presence of neighboring

geminal silanols, which are unique to low temperature dehydroxylation steps, thus offering a plausible explaination for the flattened slope of the silanol number curve at low temperatures.

2.4 CONCLUSIONS

We demonstrate that a theoretical model consisting of less than three hundred atoms can accurately predict macroscopically measured properties of amorphous silica surfaces. By simulating the thermodynamically limited dehydroxylation process, the described methodology allows for direct comparison and validation with experimental data. Our method thus results in representative surface models for a range of temperatures, which can be used for computational studies of real systems using DFT calculations, in particular, for the study of catalyst-support interactions. The general methodology we developed to build our model is applicable to other complex surfaces, requiring only a measurable thermodynamic process for validation purposes. For example, the method could be adapted to determine the oxidation state of amorphous ceria in different reactive environments. Our general approach should hence prove valuable for constructing increasingly accurate molecular models of disordered and complex systems.

3.0 STRUCTURAL AND ELECTRONIC PROPERTIES OF PT_{13} NANOCLUSTERS ON AMORPHOUS SILICA SUPPORTS

The content of this chapter is taken from C. S. Ewing, M. J. Hartmann, K. R. Martin, A. M. Musto, S. J. Padinjarekutt, E. M. Weiss, G. Veser, J. J. McCarthy, J. K. Johnson, and D. S. Lambrecht, "Structural and Electronic Properties of Pt13 Nanoclusters on Amorphous Silica Supports", *J. Phys. Chem. C* 119 (2015) 2503-2512.

3.1 INTRODUCTION

Metal nanoparticles (NPs) have attracted considerable attention in the field of heterogeneous catalysis due to their large surface-to-volume ratios and low-coordinated active surface sites.[11-13,15,16,28,39,40,43,97] These NPs are typically immobilized on oxide supports, which can affect the activity and selectivity of the NPs by altering their morphology and electronic structure.[12,13,21,29,43,97] As pointed out by Norskov et al.,[7] there is a critical need for a fundamental atomic-scale understanding of catalyst-support interactions because they can dramatically impact the electronic properties of the supported NP. This information cannot be obtained from experiments alone[98] and current modeling approaches almost always ignore the amorphous nature of the support.[12,13,15,18,19,21] Generating atomistic models of supported NPs on amorphous supports poses challenges not faced when using crystalline surfaces, because of the diversity of

surface features and atomic surface roughness. The present work focuses on the development of a transferable methodology for studying the relaxation of catalytic nanoparticles on amorphous supports; we apply this methodology to investigate catalyst-support interactions for amorphous silica.

Amorphous silica is a widely used catalyst support due to its good thermal stability, tunable porosity, and highly tunable specific surface area. [28,29] Silica supported Pt has shown promise for methane conversion[99] as well as low temperature oxidation of formaldehyde[28] and ethylene.[40] Although silica is relatively inert, it can be expected that its diversity of surface features will result in a wide range of metal-support interactions involving both physisorption and covalent Pt-O and Pt-Si bond formation at higher temperatures. A number of experimental studies have shown that the characteristics of the silica support, such as the concentration of surface silanols,[28] significantly affect Pt dispersion, catalytic activity, and thermal stability.[11,28,29,40,43,97,100,101] The atomistic origins of these effects, however, have remained elusive to-date. Experiments have moved toward an atomistic understanding of these interactions by attempting to produce highly mono-disperse supported NPs in order to probe the intrinsic catalytic activity as a function of size and shape. [102] However, given the importance of NP-support interactions, it is unclear whether—for amorphous supports—these interactions will induce a level of heterogeneity into the system that would make it impossible to reliably ascribe catalytic activity to a given NP size or shape. We aim to address these issues in this study for very small Pt NPs.

Silica has a large number of possible surface motifs that can be controlled in a straightforward way via the calcination temperature. Silanol groups (Si-OH) are typically formed on silica surfaces during synthesis and by exposure to water. Surface silanols can be classified as

single, Si-OH, or geminal, $Si(OH)_2$. Each OH group can further be either vicinal, meaning that it is hydrogen bonded to a neighboring silanol, or free, meaning that it is not hydrogen bonded (see Figure 3.1). Silanol groups condense to form water vapor and siloxane bridge structures as the surface is heated, resulting in a reduction of the silanol number, $\alpha_{OH,}$ (total surface silanol content, OH/nm^2).[52] Above ~1200 °C the surface is exclusively terminated by siloxane bridges (Si-O-Si). It has been observed from experiments and modeling that α_{OH} and the silanol type (single, germinal, etc.) are strong functions of the thermal pretreatment (calcination) temperature, T_{pre}, of the silica support.[52,103] The interactions between NP and support depend on the silica surface groups present at the time of NP deposition, which in turn directly depend on T_{pre}. An atomistic understanding of metal-support interactions may thus allow for the optimization of stability and/or activity of silica supported NPs via the surface pretreatment conditions.

In this study we use density functional theory (DFT) calculations to investigate the impact of metal-support interactions on the morphology, electronic structure, and energetics of 13-atom Pt NPs supported on amorphous silica. Platinum clusters of this size (d = 0.7 nm) are small enough that metal-support interactions can significantly impact cluster morphology.[98] Crystalline surface models do not constitute realistic surrogates for amorphous silica because they exhibit only a small fraction of the configurations of surface features found on the real surface of amorphous silica. We therefore developed a procedure for generating supported Pt systems using accurate model structures of amorphous silica surfaces[103] to sample metal-support interactions for a large number of silica surface sites. Using this approach, we investigate the dependence of geometric and electronic properties of the supported Pt clusters on the variability of the amorphous silica surface. Our ultimate goal is to understand metal-support interactions and their role in catalysis for realistic model systems.

3.2 METHOD

3.2.1 Computational Details.

For all DFT calculations we used the CP2K code, which employs a Quickstep[78] implementation of the DFT method using plane waves/pseudopotentials and localized Gaussian basis sets (see appendix for details). Calculations used the revised PBE functional (revPBE)[104] and GTH pseudopotentials[81,82] in conjunction with short range double-ζ basis sets with polarization functions (SR-DZVP).[105] All surface slabs were relaxed using CP2K treated as periodic in all directions with at least 20 Å of vacuum between slabs to eliminate interactions between the periodic images of the surface slabs. Validation of the planewave energy cutoff, basis sets, vacuum spacing and spin-restricted relaxation can be found in the appendix (Figure A2.1, A2.2, and A2.3, respectively).

3.2.2 Model Amorphous Surfaces.

We used model amorphous silica surfaces developed by Ewing et al.[103] to investigate NP-surface interactions. Briefly, the model amorphous silica surface structures were generated as follows: bulk amorphous silica structures were generated using reactive molecular dynamics with the ReaxFF formalism parameterized for silica and water.[106] The structures were then cut into periodic surface slabs, which were hydroxylated by saturating undercoordinated atoms, followed

by full relaxation using periodic DFT. Surface structures representing a range of temperatures were generated by simulating the thermodynamics of dehydroxylation using DFT. The temperature corresponding to each particular surface structure was computed based on the energetics of dehydroxylation using a statistical thermodynamics model. For more details, refer to the original published work.[103] These model surfaces have been validated against experimentally measured silanol number and silanol distributions and found to accurately predict silanol number as a function of temperature.[103]

The sizes of the surfaces we used were 23.7 Å × 18.3 Å × ~12 Å comprising between 250 and 270 atoms. We primarily use the cuboctahedral geometry for Pt_{13}, supplemented by a few calculations using the gas phase global energy minimum structure for Pt_{13}.[107] Experimental characterization of sub-nanometer clusters, such as Pt_{13}, is challenging and data regarding the atomic structure of Pt_{13} is hence scarce in the literature. However, a number of experimental studies of Pt_{55} (the next larger magic number cluster) supported on amorphous silica surfaces report a cuboctahedral structure,[10,108-111] motivating the use of this structure in theoretical studies.[13,15,112] Moreover, there are reports of the existence of cuboactahedral Pt_{13} clusters.[113] We hence chose to base most of our calculations on a cuboctahedral structure due to experimental evidence as well as a planned future extension of the present study on the size dependence of catalyst-support interactions, for which the cuboctahedral structure is particularly suitable because it exhibits surfaces that are representative of multiple relevant crystal facets, (100) and (111), as well as steps and corners. We have verified that key results of the present study hold also for the lowest energy gas phase configuration of the Pt_{13} cluster (see discussion in the results section). Starting from vacuum optimized NP structures, shown in Figure 3.1b, we simulated the

adsorption of NPs onto the silica surface using discrete element method[114] (DEM) simulations followed by DFT calculations.

In contrast to supported NPs on crystalline surfaces, generating initial structures of the NPs on the support is non-trivial when modeling amorphous supports; if the NP is too close to the surface then initial repulsive forces will cause artificial restructuring; if the NP is not close enough to the surface, no relaxation will occur because of the lack of long-range forces in DFT. Simulating NP adsorption—even in the gas phase—onto a support using DFT (e.g., *ab initio* molecular dynamics) would be computationally expensive. Hence, the use of DEM to generate reasonable starting NP-surface structures is crucial to our methodology. Similar to classical molecular dynamics, particle trajectories are obtained in DEM simulations via Newton's laws of motion for each particle at discrete time. In their simplest form the forces on particles, described by contact mechanics,[115] include normal, Hertzian, repulsion and gravitational forces, along with tangential friction. For the purpose of our study, the forces in DEM can be limited to only gravity, hard-sphere interactions, and tangential friction, where rebounding of particles (atoms) is completely avoided by tuning the viscoelasticity of the particles in the simulations. This allows for the generation of reasonable initial structures, using negligible computational effort, which can be followed by full relaxation using DFT.

3.2.3 Generating Initial Structures.

We generated starting geometries that sample different initial conditions. We considered two different possible orientations of the NP with respect to the silica surface, one with the (100) facet and one with the (111) facet facing the silica surface; these two facets are shown in Figure 3.1b. Additionally, we considered two different amorphous silica surfaces corresponding to T_{pre}

of 200 and 570 °C, shown in Figure 3.1a. These surfaces correspond to silanol numbers of 4.4 and 1.6 nm^{-2}, respectively.[52] We divided the surfaces with a 5-by-4 grid, resulting in 20 uniformly distributed adsorption sites. Altogether, this resulted in 80 initial geometries that span a range of different local surface sites, NP orientations, as well as different silica pretreatment temperatures corresponding to different silanol numbers.

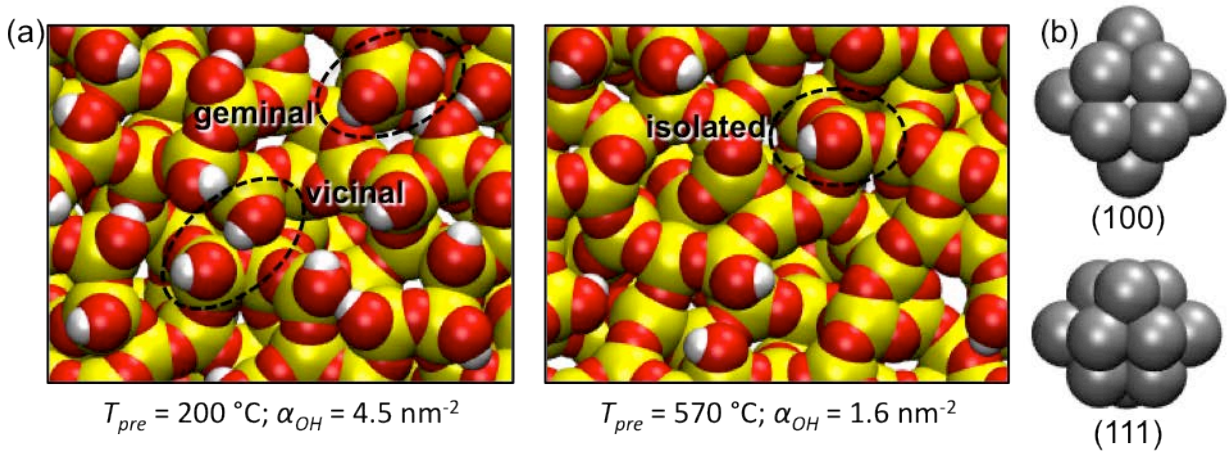

Figure 3.1. Top-down view of the structures used in this study: (a) Amorphous silica surfaces corresponding to pretreatment temperatures of 200 °C and 570 °C, based on analysis of experimental data by Zhuravlev.[52] Different types of silanol groups are illustrated. (b) Two initial orientations of cuboctahedral Pt_{13} corresponding to (100) (top) and (111) (bottom) surfaces facing downward upon adsorption. Images were rendered using VMD.[116]

3.2.4 Simulating NP Adsorption.

We simulated the adsorption of Pt on silica using a procedure, illustrated in Figure 3.2, that generates physically reasonable structures by relaxing all atom positions with DFT. We automated the procedure using a series of Perl and Python codes that perform the following steps for ***each*** of the systems initialized in the previous step: (a) *Initialization of the cluster/support system*. Gas-phase optimized cuboctahedral Pt_{13} was placed on a grid point in the *xy* plane above the silica surface. (b) *Dropping the cluster onto the surface*. The cluster was then dropped onto the surface, by imposing a gravitational force, using a discrete element code[117] invoking the following approximations: (i) all atoms were treated as hard spheres with radius equal to their respective van der Waals radii; (ii) the cluster and surface were treated as rigid bodies; (iii) the particles (i.e., atoms) dissipated energy quickly enough during collisions to avoid any rebounding. The clusters typically rotated to some degree as a result of gravity and a point of hard-sphere contact between NP and surface. These steps generated configurations with sufficiently close NP-surface distances to facilitate relaxation (local optimization) with DFT to strongly bound physisorption states. Typical relaxation energies for physisorbed clusters were 2-3 eV (i.e., the relaxed structures were 2-3 eV lower in energy than the starting configurations). We also verified that these initial configurations were not so close that the NP-surface interaction was repulsive. We confirmed that the energy of each initial condition was lower than the combined energies of the isolated NP and silica slab, indicating that the DFT relaxed geometries are not a result of an initially repulsive NP-surface interaction. The average NP-surface energy, prior to relaxation with DFT, was -0.9 eV for all physisorbed systems. (c) *Cluster-silica bond formation*. Experiments have indicated that noble metal clusters (such as Pd_n) supported on silica form metal-oxygen bonds with the support during preparation of the NP-silica catalyst systems,

whereas metal-silicon bonds are only formed at higher than typical calcination temperatures.[100,118,119] Our initial calculations confirmed that Pt-O bond formation is also energetically favorable for Pt/silica. Specifically, we found that H migration from silanol to the Pt cluster accompanied by Pt-O bond formation yields a ~2.4 eV decrease in system energy per Pt-O bond formed. This can be expected because the process involves breaking one bond (O-H) and forming two new bonds (Pt-O and Pt-H). We do not consider kinetic limitations in this process, which are beyond the scope of this study, but rather we assume that the formation of Pt-O bonds occurs whenever there is close contact between the Pt NP and a silanol group. For these reasons, we incorporated a step in our initial geometry preparation that facilitated Pt-O bond formation by removing hydrogen atoms from surface silanols within range to bond to Pt (see appendix for details). For systems with an even number of Pt-O bonds, we assumed that the hydrogen would desorb in the form of H_2. For systems with an odd number of Pt-O bonds formed, a single hydrogen atom was placed on top of the platinum cluster. This was done to allow for spin-restricted DFT calculations, which significantly reduced computational effort. When surface hydrogens were removed, we repeated DEM calculations in step (b) to allow for better initial geometries for the formation of NP-surface bonds. During this step, the hard sphere radii for Pt and O atoms involved in potential Pt-O binding were set to the covalent radii. (d) *Relaxation of the cluster/silica system*. Finally all atoms in each system were locally relaxed using DFT using a conjugate gradient algorithm.

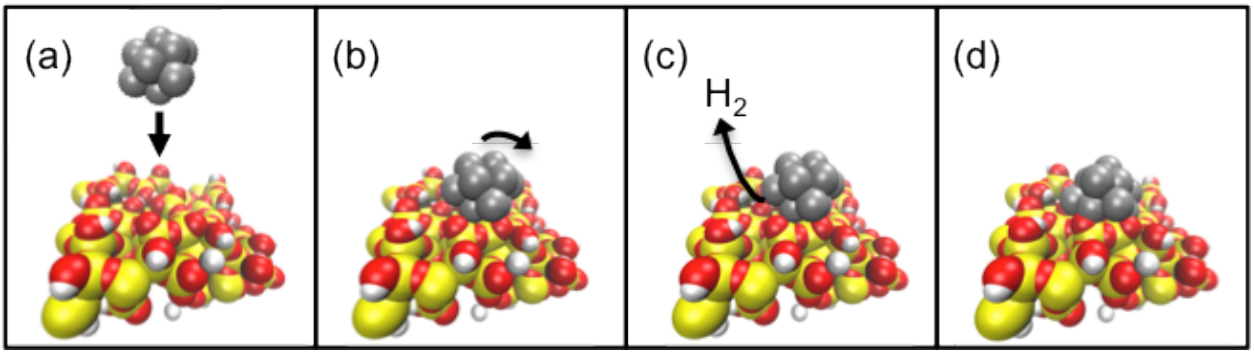

Figure 3.2. Procedure for simulating NP adsorption. (a) An NP having one of two different orientations is dropped to the surface from one of 20 *xy* grid points. Two surfaces are used, each having a different pretreatment temperature, giving a total of 80 different systems. (b) The NP is allowed to rotate using rigid-body approximations and hard-sphere interactions. (c) Pt-O bonds are facilitated by removing H atoms in contact with Pt. (d) The entire system is locally relaxed using DFT.

3.3 RESULTS AND DISCUSSION

3.3.1 NP-Support Binding Interactions.

Platinum NPs can bind to the support surface via physisorption or via covalent Pt-O and Pt-Si bonds. We characterized bonding using the simple distance rules for a ball-and-stick molecular model (see appendix for details). Due to the heterogeneity of the silica surface, there is a wide

distribution of the number of covalent bonds between Pt and silica, shown in Figure 3.3. The number of Pt-silica bonds for a single system depends on the local silica surface structure at the adsorption site: sites with only siloxane termini typically result in only physisorption while sites with high silanol density result in multiple Pt-support interfacial bonds. This reflects our assumption that during catalyst preparation O-H bonds are broken but Si-O bonds are not, which is in agreement with experimental observations.[100,119] On average, this approach yields 3.1 and 1.4 covalent Pt-silica bonds for surfaces with T_{pre} = 200 and 570 °C, respectively. In a few cases, we observed Pt-Si bond formation via rupture of a siloxane bridge during relaxation. When visualized, it appears that a Pt atom bonds with both the Si and O atoms involved in a siloxane bridge followed by dissociation of the Si-O bond. Interestingly, the relaxation did not reveal an energy barrier; however, it is unclear whether this is an artifact of the relaxation scheme or not. Interpreting this observation is not within the scope of this study and these occurrences were rare enough (only 4 cases in 80 systems) that they do not significantly impact the results of this study. Overall, the number of covalent NP-Silica bonds formed is inversely related to silica surface pre-treatment temperature. This is an expected result because the dehydroxylation of silica results in a lower surface hydroxyl density at higher temperatures. Generally, we expect that the effect of metal-support interactions on the Pt-NP's geometry, electronic properties, and stability will depend on the number of bonds formed between Pt and silica.

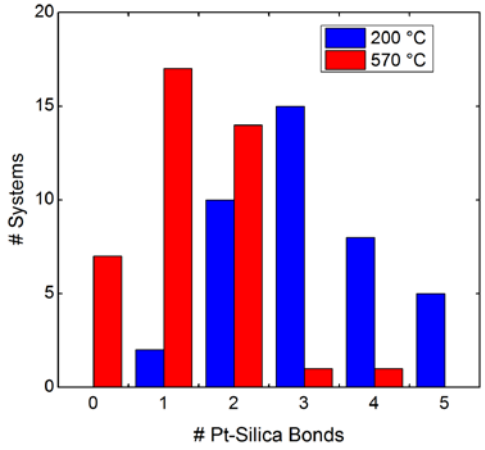

Figure 3.3. Distribution of the number of Pt-silica bonds (both Pt-O and Pt-Si) for silica surface pretreatment temperatures of 200 and 570 °C, having α_{OH} values of 4.4 and 1.6 nm^2, respectively.

3.3.2 Nanoparticle Stability Depends on Support Preparation.

Next we consider the impact of silica support properties on nanoparticle stability. Campbell and Sellers have shown that the metal NP chemical potential is fundamental to understanding NP stability because it represents a measure of the thermodynamic driving force for sintering. Rate equations derived from microkinetic models for sintering have shown that the chemical potential of the metal is inversely related to the apparent activation energy of the sintering process, whether the sintering occurs via Ostwald ripening or particle diffusion/coalescence.[11] Furthermore, the chemical potential of a supported metal NP is directly related to its adhesion energy, E_{adh}, defined as the work required to separate the metal/oxide interface in vacuum per

interfacial area.[11] Stronger NP adhesion (i.e., more negative E_{adh}) results in lower metal chemical potential. Experiments have indicated that by tailoring the support material, and thus the adhesion energy, NP sintering can be mitigated.[120,121] We calculated the energies associated with distortion of the Pt and silica structures, i.e., deformation energies (see appendix Figure A2.4), and found that they are small compared to the interaction energies for bonded systems (see appendix Table A2.1). The adhesion energy times the area of metal-support contact is therefore equivalent to the Pt-silica interaction energy, E_{int}, defined as

$$E_{int} = E_{Pt-S} - E_{Pt}^{fixed} - E_{S-H}^{fixed} \quad (3.1)$$

where E_{Pt-S} denotes the energy of the NP bound to the silica support, with all atoms relaxed. E_{Pt}^{fixed} and E_{S-H}^{fixed} denote the energies of the NP and support fixed in the relaxed geometries of the Pt-support system. Note that if H atoms were removed from the support surface during the binding procedure then E_{S-H}^{fixed} involves a surface with dangling bonds.

A linear fit of the data in Figure 3.4 shows a strong correlation (R^2 = 0.97) between interaction energy and the number of NP-support bonds. The slope of the line is -3.3 eV and gives an estimate of the average bond energy between the NP and the silica surface; these are mainly Pt-O bonds although a small number (less than 5%) of Pt-Si bonds are also included in this correlation. This value is essentially identical to the bond energy for a $Pt\text{-}O^+$ diatomic cation, but about 1 eV less attractive than the bond energy of the neutral Pt-O dimer (-4.3 eV).[122] We do not expect that the NP-surface bond energy to be the same as the Pt-O dimer bond energy because both Pt and O atoms share bonds with other atoms in the NP-silica system. Nevertheless, the fact that the NP-surface bond energy is very similar to the Pt-O dimer bond energy is

reassuring. Figure 3.4 implies that the adhesion energy of supported Pt NPs can be correlated with surface pretreatment temperature because the number of Pt-surface bonds is inversely correlated with T_{pre}. Average interaction energies of -12.4 and -6.8 eV for the T_{pre} = 200 °C and 570 °C surfaces, respectively, demonstrate the impact pretreatment temperature could have on NP adhesion. These results suggest that support pre-treatment temperature may be used to tune catalyst stability; however, further studies will be necessary to elucidate the exact correlation. To determine whether our results were specific to cuboctahedral Pt_{13}, we simulated the adsorption of the theoretical gas phase global minimum Pt_{13} structure[107] using the same procedure that was used for cuboctahedral structures. We used the T_{pre} = 200 °C surface, one orientation, and 20 *xy* gridpoints. We found that the total energies of the supported systems, as functions of the number of Pt-silica bonds (i.e., normalized by the number of atoms in the system), were the same regardless of initial Pt_{13} structure, as shown in Figure A2.5. The energy of the final structure is thus essentially independent of the energy of the unsupported structure used for the initial conditions. This unexpected result is due to the dominating influence of the interfacial interactions for Pt_{13} NPs.

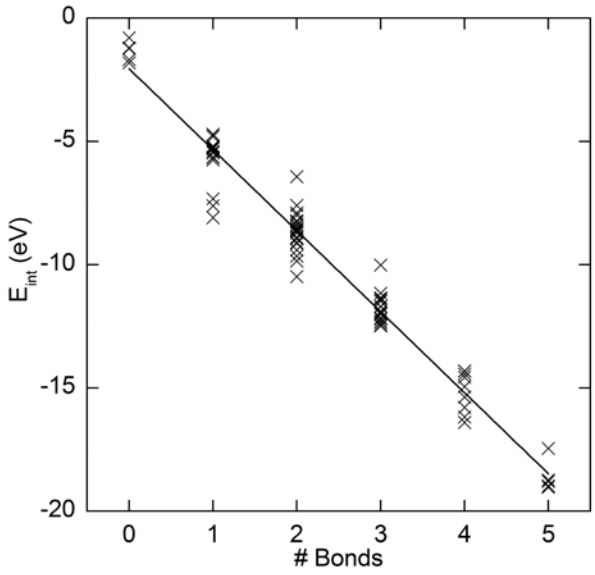

Figure 3.4: Pt-silica interaction energy as a function of the number of bonds formed between the silica surface and the Pt cluster. The line is a least-squares fit to the data. The coefficient of determination is $R^2 = 0.97$, the slope, which is an estimate of the energy per bond, is -3.3 eV.

3.3.3 Metal-Support Interactions Significantly Affect Pt Structure.

In this study we aim to gain quantitative insight into Pt-silica interactions by investigating properties that have previously been shown to correlate with catalytic activity. The coordination number (CN) of a metal active site has consistently been shown to correlate strongly with adsorbate binding energy,[12,13,15,49] which can be related to catalytic activity. Figure 3.5a shows the average distribution of CNs for all 80 supported clusters in this study compared to the

unsupported cluster. We calculated both metal-metal coordination (Pt-Pt) and total CN (Pt-*), which includes coordination with Pt, Si, O, and H atoms. We found that the distribution of CNs changed dramatically upon adsorption on the support. The number of accessible low-coordinated sites can be assessed by comparing the Pt-Pt and Pt-* CNs. The number of 3- and 4-coordinated sites is significantly higher for Pt-Pt than Pt-*. However, there are still many more 3 and 4 Pt-* coordinated sites for the supported Pt than unsupported. We therefore conclude that although a significant number of low coordinated sites are inaccessible because they are buried at the interface, a large fraction remains available for binding. We found that the use of the gas phase theoretical global minimum Pt_{13} structue, instead of the cuboctahedral structure, gave almost identical CN distributions for both Pt-Pt and Pt-* (see Figure A2.6). This comparison shows that our results are not due to the use of a relatively high energy initial Pt cluster structure. Clusters with no Pt-silica bonds had CN distributions more similar to the unsupported cluster (i.e., greater number of 5 and 6 coordinated sites) than clusters bonded to the support. However, we did not find clear correlations between structural parameters (such as CNs) and the number of Pt-silica bonds (see appendix Figure A2.7) except for two general trends: (1) The distribution of CNs becomes broader in systems with Pt-silica bonds. (2) Figure 3.5b shows that on average, CNs are smaller for supported than for unsupported systems. The reason for the apparent lack of correlation between CN and Pt-silica bonds can be explained by the finding that NP-silica binding has opposite effects on CN of Pt atoms buried at the silica interface and at the exposed NP surface. In the former case, binding to silica leads to an increase of CN (as other Pt atoms are attracted to the Pt/Silica interface), and in the latter we observe a decrease of CN (as Pt atoms move away from the exposed surface). In summary, this gives rise to a complicated composite effect.

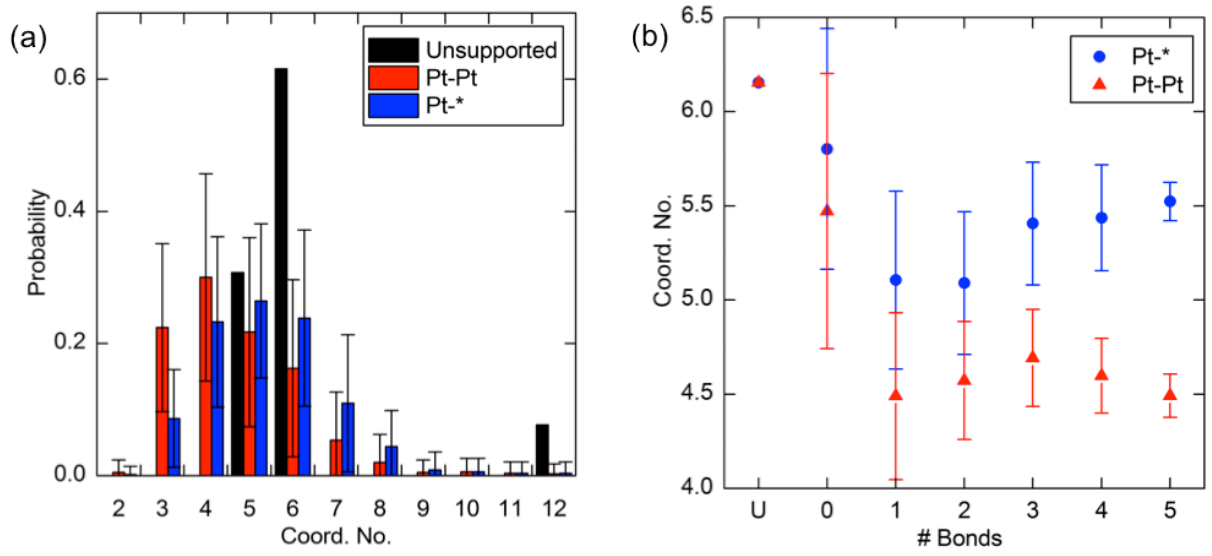

Figure 3.5. (a) Distribution of atomic coordination numbers for Pt_{13} clusters averaged over all 80 systems in this study. Black: unsupported Pt_{13} cluster; Red & Blue: cluster optimized after placement on silica support. (* denotes any atom type). (b) Average coordination number vs number of Pt-silica bonds for all 80 systems in this study. U indicates unsupported. Error bars show standard deviation for both (a) and (b).

Metal-metal bond length has been shown to correlate with adsorbate binding strength, and could therefore significantly affect catalytic reaction rates.[123] Experiments have shown that sub-nm Pt clusters undergo bond compression when supported on alumina and carbon.[9] Unfortunately, experiments probing metal-metal bonding (e.g., X-ray adsorption near-edge structure or X-ray adsorption fine structure) can only provide average bond lengths and coordination numbers for an entire supported NP at best, and hence cannot distinguish between

accessible and non-accessible (e.g., buried in the Pt-silica interface) sites.[9] Figure 3.6a shows that Pt-silica bonding results in significant Pt-Pt bond compression. This bond compression, furthermore, was consistent between surface, fully coordinated and interfacial atoms (see appendix Figure A2.8).

Figure 3.6b shows that there is an approximately linear relationship between bond compression and average Pt-Pt coordination number. Furthermore, the unsupported Pt_{13} cluster (red dot) lies on the same line as the supported clusters, suggesting that the observed bond compression is essentially a result of reduced (average) CN of the metal NP. This is not unexpected, as surface compression is well known to occur at solid-gas interfaces. The magnitude of the observed bond compression, however, suggests that the relationship between CN and adsorbate binding energy calculated using surfaces or fixed bulk geometries [12,13,15] may be significantly different than for fully relaxed small supported clusters, in particular, on amorphous supports. Based on our results, we expect the effects of metal-support interactions on adsorbate binding energies to be complicated because NP-support interactions give rise to two competing phenomena, namely an increase in bond compression, which generally weakens adsorbate binding, and a decrease in CN, which generally enhances adsorbate binding.

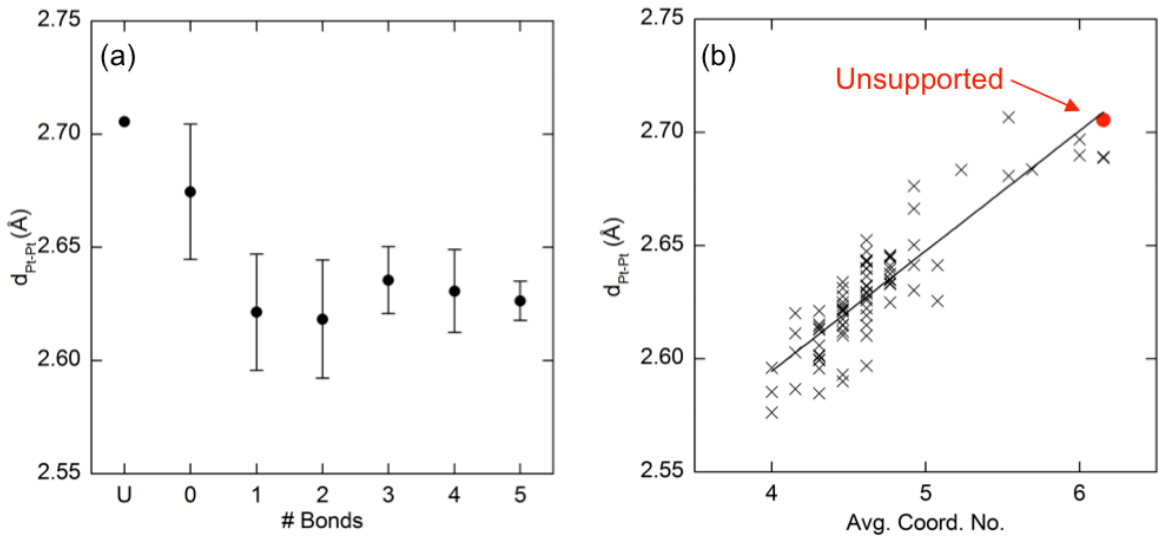

Figure 3.6. (a) Mean Pt-Pt bond length as a function of number of bonds between Pt and silica, averaged over all 80 systems in this study. U indicates the unsupported NP. Error bars show the standard deviation. (b) Mean Pt-Pt bond length, d_{Pt-Pt}, as a function of the average Pt-Pt coordination number for each of the 80 supported clusters. Red circle: unsupported Pt_{13} cluster. The line is a least-squares fit having $R^2 = 0.76$.

3.3.4 Electronic Structure is Affected by Both Reconstruction and Metal-Support Bonds.

Localization of electron density around active sites can affect adsorbate binding significantly. Generally, electron acceptors (e.g., O_2) bind preferentially to negatively charged sites while positive charge strengthens binding of electron donors (e.g., CO).[124] We calculated Bader charges for all optimized NPs with and without the support. Figure 3.7a shows that physisorbed clusters have a net charge close to zero and clusters become increasingly cationic with the

number of Pt-O bonds. Charge transfer from the cluster to support is linearly dependent on the number of Pt-O bonds, reaching over 2 *e* for clusters with 5 Pt-O bonds. This magnitude of charge transfer has been shown to dramatically impact catalytic reactions.[22] We therefore expect that this charge transfer may significantly impact adsorbate binding and hence catalytic activity. Pt-Si bonding results in significant charge transfer from the silica surface into the Pt_{13} (blue points in Figure 3.7a). The magnitude of charge transfer is considerable for Pt-Si and Pt-O bonds, resulting in individual Pt atomic charges of (up to -1.0 and +0.6 *e*, respectively). Figure 3.7b shows that in general, for non-interfacial atoms, atomic charge is more positive with increasing CN. Pt atoms at the Pt-silica interface can have a significant positive charge and many of these have relatively small Pt-* CN, indicating that they are accessible to adsorbates, as illustrated in Figure 3.8. This suggests that electron donor molecules may preferentially bind at the perimeter of the Pt-silica interface. The linear relation between nanoparticle charge and both number of Pt-silica bonds and coordination number, respectively, has important consequences for experimental probes of CNs or NP-Silica bonds. For example, the IR frequency of the CO stretch is known to be sensitive to surface charge[125] and could be used to experimentally probe for CNs and number of NP-Silica bonds via the correlation observed in Figure 3.7b.

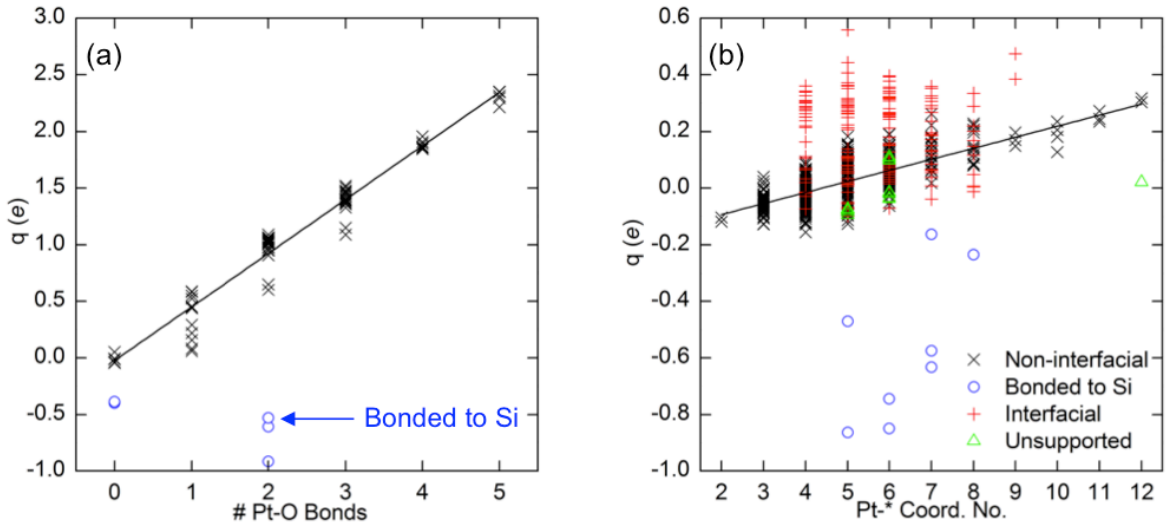

Figure 3.7. (a) Net charge of Pt cluster (Bader charges) as a function of the number of silica O atoms bonding to the Pt cluster. Data for clusters with one Pt-Si bond are shown as blue circles. The line is a linear fit to the data (excluding systems with Pt-Si bonds). The coefficient of determination is $R^2 = 0.98$. The slope, which is an estimate of the charge transferred per Pt-O bond, is 0.47. (b) Atomic charge on individual Pt atoms as a function of Pt-* coordination number for all Pt atoms in all supported clusters. Red plus signs, blue circles, green triangles, and black x symbols correspond to atoms at the Pt-silica interface, bonded to Si, unsupported cluster, and all other atoms, respectively. The line is a linear fit to the data points represented as x symbols.

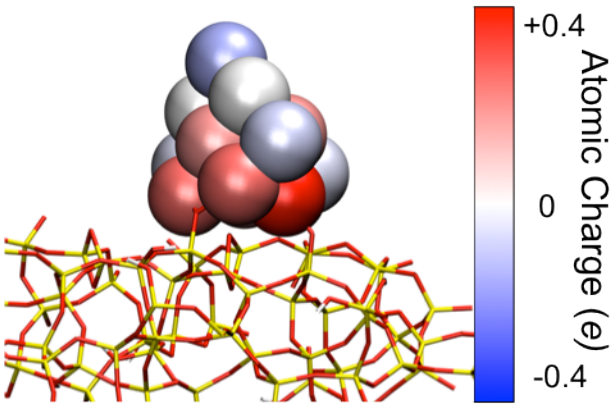

Figure 3.8. Distribution of charges on a supported Pt_{13} cluster with two Pt-O bonds. Atoms bonding to hydroxyls and their neighbors clearly undergo charge depletion whereas low coordinated atoms not near the silica surface have slightly negative charges.

Although Pt_{13} is small enough that the d-density of states (DOS) is discretized,[13] the d-band center (average energy of the d states) has been shown to correlate with adsorbate binding energies for 12 and 13 atom clusters.[12,15] In general, adsorbate-metal bonding for transition metals results in bonding and anti-bonding states. Lower d-band center corresponds to increased filling of the anti-bonding states upon adsorbate binding, and hence weaker binding strength.[126,127] We have calculated the density of states for each individual Pt atom, from which we calculated the d-band center, ε_d, as

$$\varepsilon_d = \frac{\sum \varepsilon_i \rho_i}{\sum \rho_i} \qquad (3.2)$$

where ε_i is the eigenvalue of state *i* and ρ_i is the density of state *i*. We considered states with eigenvalues between -8 eV and +6 eV. In agreement with previous studies,[12,15] we found that the d-band center for Pt atoms roughly correlates with CN, when considering all atoms in the isolated cluster. When analyzing Pt atoms for all supported Pt_{13} systems in this study, however, there is at best a weak correlation between d-band center and CN (see appendix Figure A2.9). To test if this lack of correlation is due to the wide range of geometries observed in this study, we analyzed each system individually. We fit the d-band center as a function of the CN for each individual system with a linear equation and calculated the coefficient of determination (R^2). We found that for almost all systems there was no clear correlation between the d-band center and the Pt-Pt CN. The results clearly indicate that it is not just the wide range of different geometries on amorphous supports, but that CN cannot be used to predict relative d-band centers for adsorption sites on silica-supported Pt_{13}, even when considering a single supported cluster (see appendix Figure A2.10).

Recent work has shown that it is more appropriate to treat small, supported metal clusters as molecules rather than small pieces of bulk metal.[21,39] We therefore considered the d-bands of entire Pt clusters. Supporting Pt_{13} on silica did not result in a consistent perturbation of the d-DOS; however, d-band centers for supported systems varied significantly from about -1.87 to -1.64 eV, compared to -1.75 eV for the unsupported cluster (see appendix Figure A2.11). When re-calculating the DOS for systems after removing the support (but fixing the reconstructed Pt geometry) we found that the d-DOS is unaffected by Pt-silica bonds. This means that the wide range of d-band centers observed is due to the degree of reconstruction caused by metal-support interactions upon adsorption of the NP and not electronic interactions with the support.

Supporting the notion that small supported metal clusters behave as molecules, previous theoretical investigations have shown that, for small metal clusters, the frontier orbitals—the highest occupied molecular oribital (HOMO) and lowest unoccupied molecular orbital (LUMO)—can be used to accurately predict relative binding energies of adsorbates.[39] In particular, binding properties of electron acceptors and donors are particularly well correlated with the localization of the HOMO and LUMO, respectively, on small metal clusters.[20,39] We therefore performed a qualitative analysis on a number of the systems in this study to investigate the effects of Pt-silica interactions on frontier orbitals. We found that supporting the cluster on amorphous silica can have a dramatic impact on the 'extent' (i.e., the size of an atomic orbital at constant iso-value) and directionality of both the HOMO and LUMO at different surface sites. These effects could be a result of multiple factors: (1) significant distortion of the cluster geometry, (2) Pt-O bond formation, and (3) non-covalent (van der Waals and electrostatic) interactions between cluster and support. To isolate the effects of these factors, Figure 3.9 shows a comparison of the HOMO and LUMO for Pt_{13} relaxed in vacuum (unsupported), relaxed on the silica surface, and relaxed on the silica surface followed by the removal of the silica support. This allowed us to discern the roles of geometric reconstruction (unsupported vs supported) and Pt-silica interactions (supported, with vs without silica atoms).

We discovered a number of general trends for all observed systems. First, it is clear by comparing the first two columns of Figure 3.9 that distortion of the cluster geometry due to NP-support interactions results in dramatic changes to both the extent and directionality of the HOMO and LUMO. Comparison of the supported Pt cluster with and without silica atoms (2nd and 3rd columns of Figure 3.9) demonstrates the effects of Pt-O bond formation on the frontier orbitals. In general, we found that Pt-O bonds significantly affect the extent of the HOMO and

LUMO in a consistent way. Near Pt-O bonds, the extent of the HOMO is increased while the LUMO is reduced. For atoms far from Pt-O bonds, however, the extent of the LUMO is increased while the HOMO is reduced. This can be interpreted as the formation of Pt-O bonds "pulling" the HOMO in while "pushing" the LUMO away. Analysis of supported Pt_{13} systems with no Pt-O bond formation show that non-covalent Pt-silica interactions have negligible effects on the frontier orbitals (see appendix Tables A2.2 and A2.3).

The effect of NP-silica binding on the frontier orbitals is expected to influence adsorbate binding in the opposite way to charge distribution, discussed above. In particular, the increase of the HOMO amplitude near Pt-O bonds suggests that the affinity to bind electron acceptors (e.g., O_2) at the Pt-silica interface is increased upon forming Pt-silica bonds. Conversely, the reduction of LUMO amplitude near Pt-O bonds suggests that the binding affinity for electron donors (e.g., CO) at the Pt-silica interface will be decreased. NP-silica binding thus results in competing phenomena: redistribution of the frontier orbitals and electron density distribution. As we have already seen for the geometric parameters, the correlation between structure (deformation) and NP-silica binding is quite complicated due to a superposition of multiple effects. It can therefore be expected that the impact of NP-support binding on catalyst-substrate adsorption may also be quite convoluted. A detailed study of NP-substrate binding thus requires significant development that goes beyond the scope of this work and will be presented in a future publication.

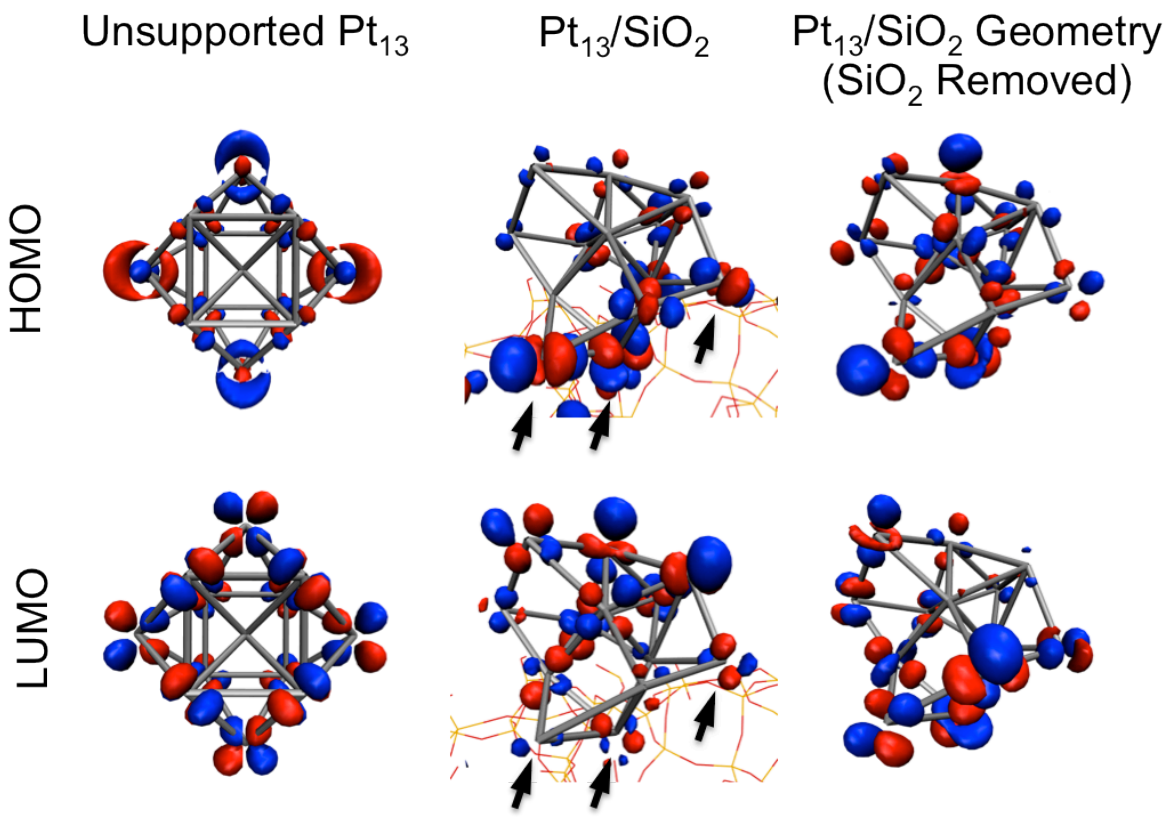

Figure 3.9. Representative images of the HOMO and LUMO for unsupported cuboctahedral Pt_{13}, Pt_{13}/SiO_2, and Pt_{13}/SiO_2 with silica atoms removed.

3.4 CONCLUSIONS

We have developed a methodology for studying metal nanoparticles on amorphous supports, which can be applied to a number of NP and support materials. Our approach uses a combination of the discrete element method and DFT calculations to generate model systems of supported NPs. We used this method to quantitatively investigate the impact of an amorphous silica surface on the morphology, electronic structure, and energetics of supported Pt_{13} clusters. Our results reveal that the support significantly alters the physicochemical properties of the adsorbed NP. A summary of our findings is as follows:

1. Our results suggest that surface pre-treatment temperature can be used to tune the Pt-SiO_2 interface and thus stability of silica-supported nanoparticles because the number of Pt-silica bonds is a function of the pre-treatment temperature. Experiments to validate this prediction are currently underway.
2. Charge transfer from Pt to silica, via Pt-O bonds, is strongly correlated with the silica silanol number, and results in charge depletion of Pt atoms near the perimeter of the NP-silica interface.
3. Adsorption of Pt_{13} NP clusters on amorphous silica results in considerable relaxation of the NP. The surface-mediated relaxation leads to substantial lowering of average Pt coordination numbers, significant Pt-Pt bond compression, and dramatically affects the d-band centers and frontier orbitals.
4. The frontier orbitals are significantly affected both by the distortion of the Pt NP cluster due to adsorption and electronic effects from the silica support. The effects of NP-silica binding on the frontier orbitals and charge distribution result in competing influence on adsorbate binding behavior.

The extent of the impact of support interactions with Pt_{13} NPs, i.e. the strong effect of the Pt-SiO_2 interface, means that experimental attempts to measure the innate properties of very small NP catalysts will likely fail because the measurable physical and chemical properties will depend critically on NP-support interactions, which will vary significantly across the surface of an amorphous support. Furthermore, the magnitude and complexity of the changes to NP properties induced by catalyst-support interactions indicate that the adsorbate binding properties of these systems cannot be accurately predicted by studying either the corresponding freestanding clusters or Pt_{13} on perfectly crystalline silica surfaces, i.e. the accurate description of the Pt-SiO_2 interface is critical. The range of effects observed in this study further indicates that single geometric and electronic descriptors for adsorbate binding may not hold much meaning for sub-nm clusters on amorphous supports. Many trends determined for larger or freestanding clusters, therefore, cannot be expected to extrapolate to very small (i.e., 13 atom and smaller) metal clusters on amorphous supports. In future work we will thus investigate the impact of metal-support interactions on NP properties as a function of cluster size.

4.0 EFFECT OF SUPPORT PREPARATION AND NANOPARTICLE SIZE ON CATALYST-SUPPORT INTERACTIONS BETWEEN PT AND AMORPHOUS SILICA

The content of this chapter is taken from C. S. Ewing, G. Veser, J. J. McCarthy, J. K. Johnson, and D. S. Lambrecht, "Effect of Support Preparation and Nanoparticle Size on Catalyst-Support Interactions between Pt and Amorphous Silica" *J. Phys. Chem. C*, submitted (2015).

4.1 INTRODUCTION

Recent developments in both computational methods[2-7,12-15,128] and experimental characterization techniques[9-11] have facilitated detailed characterization of catalytic materials at the atomic level. Insights relating structural and electronic properties to catalytic reactivity, selectivity, and stability have provided some general rules for tailoring catalyst properties via what is now ubiquitously termed "rational design."[7,11-16] Many computational results have been shown to agree quite well with experimental observations; in particular, correlations involving simple properties (e.g., coordination number and adsorbate binding energies) and simple systems (e.g., extended metal surfaces and diatomic reactants). Catalytic materials research, however, has recently shifted towards ever-smaller nanoparticles (NPs) and increasingly complex support materials. While approaches to understanding *simple* catalytic materials have been well established and researched in recent years,[7,11-17] atomistic studies of supported NP systems have

been limited to idealized, perfectly crystalline supports.[18-22] Numerous studies have exploited geometry constrained calculations to isolate the effects of coordination number and NP size.[12,13,15,129] This approach often provides clear trends and powerful insight regarding catalyst design. However, distortion of the support structure has been shown to significantly alter the structure and electronic properties of supported NPs.[18,130] Amorphous supports exhibit a diverse range of local surface structures, which result in a distribution of catalyst-support interactions. Capturing the entire distribution is important because small differences in structure can significantly affect catalyst reactivity and/or stability.[130,131]

In contrast to these approaches, we have recently embarked on a research program in which we aim to (a) examine catalyst-support interactions on amorphous supports (commonly used in practice), and (b) develop a transferable methodology for predicting the effects of metal-support interactions on physicochemical properties of the supported nanoparticle. Ultimately, an improved understanding of how support materials affect the properties of catalytic nanoparticles should provide a set of design rules that can be used as a guide for developing novel or improved catalytic materials.

We recently studied the catalyst-support interactions between Pt_{13} and amorphous silica supports using a first-principles-based approach. Our calculations revealed that the physicochemical properties of Pt_{13} (0.7 nm) are significantly altered when supported on amorphous silica. The results indicate that both the charge transfer and the adhesion energy of Pt_{13} are strongly, and linearly dependent on the surface hydroxyl density, suggesting that the pre-treatment temperature of the amorphous silica support can be used to tune catalyst-adsorbate interactions as well as NP stability.[130]

Here, we extend the methodology we developed to quantitatively analyze the impact of amorphous silica supports on the morphology, electronic structure, and energetics of cuboctahedral Pt NPs having 13, 55, and 147 atoms (0.7, 1.2 and 1.7 nm in diameter, respectively). Our studies reveal the impact of NP size on catalyst-support interactions, as quantified by the number of covalent catalyst-support bonds, charge transfer, and adhesion energy between Pt and amorphous silica. We furthermore introduce a new empirical approach for the prediction of adhesion and charge transfer properties of larger NPs that allows expedited predictions on large NPs without requiring explicit density functional theory (DFT) calculations.

4.2 METHOD

4.2.1 Computational details.

All DFT calculations performed in this work used the CP2K code, which employs a Quickstep[78] implementation of the DFT method using plane waves/pseudopotentials and localized gaussian basis sets (see appendix for details). Calculations used the revised PBE functional (revPBE)[104] and GTH pseudopotentials[81,82] in conjunction with short range double-ζ basis sets with polarization functions (SR-DZVP).[105] All surface slabs were relaxed using CP2K treated as periodic in all directions with at least 20 Å of vacuum between periodic images in the *z* dimension to eliminate interactions between the periodic images of the surface slabs. The plane wave energy cutoff, basis sets, vacuum spacing and spin-restricted relaxation for these systems have been validated for these systems previously.[130]

4.2.2 Model amorphous silica surfaces.

We used periodic amorphous silica surface structures constructed from a model developed by Ewing *et al.*[103] to investigate NP-surface interactions. These model surface structures are based on first-principles simulations and have been found to accurately predict hydroxyl density and distribution of hydroxyl groups as a function of temperature without any adjustable parameters.[103] Five distinct model surfaces were generated and the hydroxyl density of each system was adjusted using an algorithm to mimic a range of silica pretreatment temperatures T_{pre}, giving a total of 56 different surface structures.[103] For the DFT calculations in this work, we use surface structures having high (4.5 nm^{-2}) and low (1.6 nm^{-2}) hydroxyl densities, corresponding to low (200 °C) and high (570 °C) T_{pre}, respectively. For the discrete element method calculations described below we use all 56 surface structures. The size of the unit cell we used for Pt_{13} calculations was 23.7 Å × 18.3 Å × 32 Å having between 260 and 290 atoms, depending on the corresponding T_{pre} . For Pt_{55} and Pt_{147} systems we doubled the unit cell size by using two identical copies of the silica slab side-by-side in the *y* direction (resulting in unit cells containing 550 or 690 atoms and having dimensions of 23.7 Å × 36.6 Å × 37 Å for Pt_{55} and 23.7 Å × 36.6 Å × 42 Å for Pt_{147}). The minimum distances between Pt NPs and their periodic images were 11.3, 11.7, and 6.7 Å for Pt_{13}, Pt_{55} and Pt_{147}, respectively. We confirmed that 6.7 Å is sufficient separation to avoid significant error due to self-interaction of the cluster with its periodic image (see appendix Table A3.1).

4.2.3 Pt nanoparticles.

We chose magic number cuboctahedral NPs for the present study because they exhibit surfaces that are representative of (100) and (111) crystal facets, as well as steps and corners. The symmetry of the cuboctahedral structure is identical for the magic number NPs that we have chosen, allowing us to focus on the effects of NP size. Cuboctahedral Pt NPs around 1-2 nm in size have been observed experimentally in a number of studies,[10,110,111,132] including Pt_{55} on amorphous silica[118,133] and Pt_{13} on a zeolite.[113] Our earlier studies show that, while these structures are only local minima, results obtained for cuboctahedral structures and gas-phase global minima structures are in qualitative agreement. We divided each of the silica surfaces for Pt_{13}, Pt_{55}, and Pt_{147} into grids of 20 (5×4), 9 (3×3) and 6 (3×2) adsorption locations, respectively. Taking into account the 4 different sets of initial conditions (two NP orientations and two silica surface structures) we generated 80, 36, and 24 systems for DFT calculations of Pt_{13}, Pt_{55}, and Pt_{147}, respectively. More details regarding our methodology can be found in a previous publication.[130]

4.2.4 Simulating NP adsorption.

We simulated the adsorption of NPs onto the silica surface using discrete element method[110] (DEM) simulations followed by DFT calculations, as described in detail previously.[130] Particle trajectories were obtained in DEM simulations via Newton's laws of motion for each particle at discrete time. In their simplest form the forces on particles, described by contact mechanics,[115] include normal, Hertzian, repulsion and gravitational forces, along with tangential friction. For the purpose of our study, the forces in DEM were limited to only gravity, hard-sphere

interactions, and tangential friction, where rebounding of particles (atoms) is completely avoided by tuning the viscoelasticity of the particles in the simulations. This allowed for the generation of reasonable initial structures, using negligible computational effort.

Experiments have indicated that noble metal clusters supported on silica form metal-oxygen bonds with the surface hydroxyls during preparation of the NP-silica catalyst systems, whereas metal-silicon bonds are only formed at higher temperatures than typical for post-synthesis calcination.[100,119,134] To best represent experimentally observed Pt/silica systems we therefore facilitate Pt-O bond formation between the NP and any surface hydroxyls that are in contact with Pt atoms in the NP by removing the H atom from those hydroxyl groups and reducing the hard-sphere interactions between the interacting Pt and O atoms to their covalent rather than van der Waals radii. Each of the initialized geometries generated for the DFT studies was fully relaxed to its local minimum using DFT. In addition, we generated many other structures on each of the 56 surfaces using DEM in order to more fully explore the number of Pt-silica bonds as a function of NP size (see below).

4.3 RESULTS AND DISCUSSION

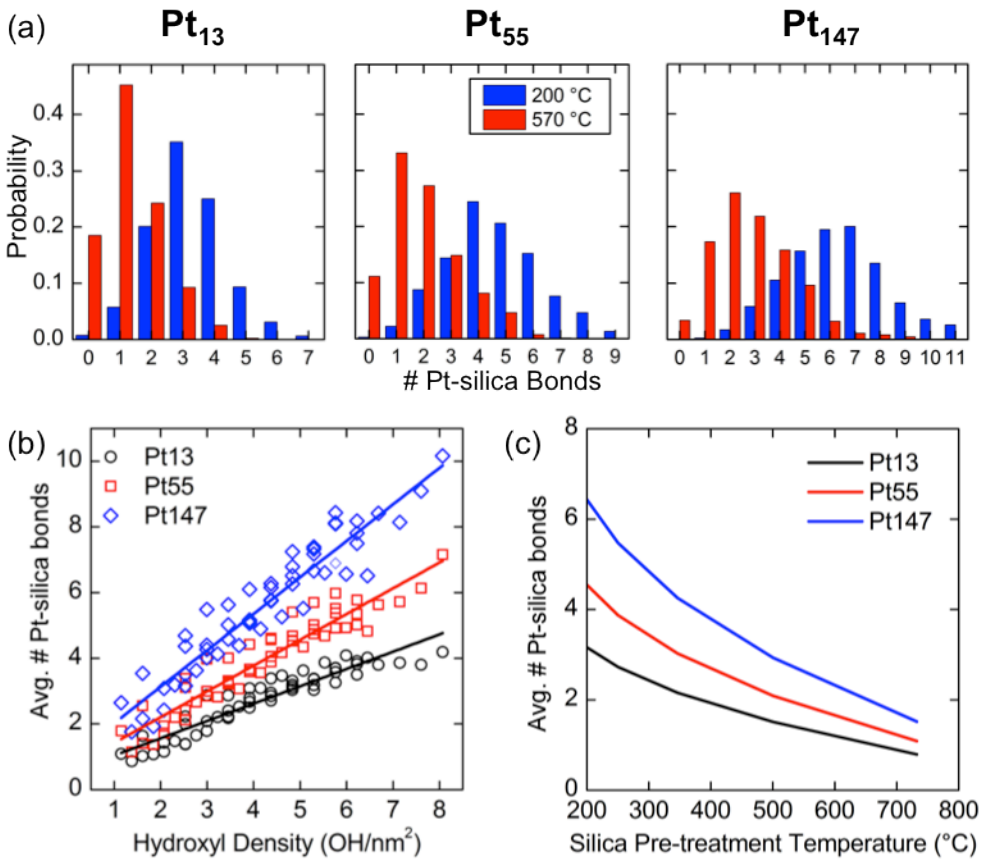

Figure 4.1. (a) Distribution of the number of Pt-silica bonds for Pt NPs with 13, 55, and 147 atoms. Data for each NP size are averaged over five different silica surfaces, with average silica pre-treatment temperature (T_{pre}) values of 200 and 570 °C. (b) Average number of Pt-Silica bonds (each point represents the average number of Pt-silica bonds for 80 grid points over two NP orientations on a single silica surface) as a function of the silica hydroxyl density. (c) Average number of Pt-silica bonds per NP as a function of T_{pre} calculated based on polynomial fits of data in (b).

4.3.1 Number of interfacial bonds depends on NP size and silica hydroxyl density.

In previous work[130] we have shown that catalyst-support interactions between Pt and amorphous silica are primarily governed by the number of Pt-O bonds, which depends directly on the silica surface hydroxyl density. To characterize NP-support binding, we used simple distance rules for a ball-and-stick molecular model[130] resulting in the number of Pt-O bonds per system being equal to the number of hydroxyls that are dissociated to facilitate bond formation during the DEM adsorption step. Due to the heterogeneity of the amorphous silica surface, there is a wide distribution of the number of Pt-silica bonds for a given surface structure, as shown in Figure 4.1a. This highlights the need to sample a variety of locations on the surface. Due to the relatively high computational cost of DFT calculations involving hundreds of atoms, we limited the number of silica structures and surface locations (as discussed in the Method section) used to generate initial conditions for DFT calculations. The DEM simulations used in the adsorption step of model generation, however, require negligible computational time relative to DFT (seconds vs days, per system). To determine the effects of NP size and silica surface pretreatment temperature (and hence hydroxyl density) on number and distribution of Pt-O bonds we therefore applied this DEM-simulated adsorption step for all 56 of the silica surface structures from our previous study[103] (representative structures of 5 independent surfaces corresponding to a range of temperatures). For these calculations we divided the surfaces into 80 grid points (10 × 8) for all three NP sizes. In all cases a gaussian distribution generally describes the distribution of Pt-silica bonds (see e.g., Figure 4.1a). By averaging the number of bonds for all 80 surface locations Figure 4.1b shows the relationship between the number of Pt-O bonds and the hydroxyl density for different Pt NP sizes. Finally, the well-established[35,52-55] relationship between hydroxyl density and temperature was used to determine how silica pre-treatment

temperature affects interfacial bonding, shown in Figure 4.1c. As expected, the number of interfacial bonds increases with Pt NP size. Furthermore, Figure 4.1a and 4.1b indicate that as the hydroxyl density is increased (i.e., for lower silica pre-treatment temperature), the effect of NP size on the number of interfacial bonds increases.

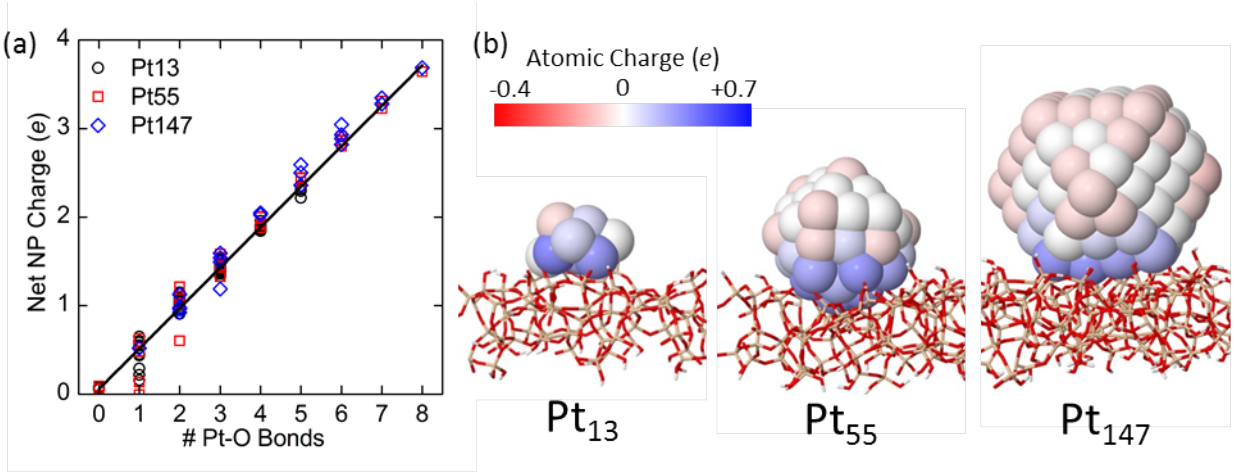

Figure 4.2. (a) Net charge on the Pt NP as a function of the number of Pt-O bonds for Pt_{13}, Pt_{55}, and Pt_{147}. The line is a least-squares fit to the Pt_{13} data with regression equation y = 0.457x + 0.0577 (R^2 = 0.978). (b) Atomic charge distributions for representative 13, 55, and 147 atom Pt NPs. Charge data were calculated from Bader analysis.

4.3.2 Pt-O bonds result in charge transfer from Pt to support.

Molecular binding energies are significantly affected by the electronic structure of active sites. Electronic structure properties–electron density, d-density of states, and shape and size of the HOMO and LUMO–often correlate with adsorbate binding energies. We limit our investigation to electron density and d-density of states because the larger NP systems have continuous band structures (see appendix Figure A3.1), prohibiting analysis of their frontier orbitals for comparison to Pt_{13}, for which the effects of amorphous silica supports has been examined previously.[130]

The accumulation or depletion of electron density at a metal active site–the atomic charge–can significantly alter adsorbate binding strength, and as a result, reactivity. [22,124] To analyze the effects of catalyst-support interactions on charge transfer we used Bader charge analysis.[135,136] We further verified that the observed trends are not a result of charge calculation method, observing a similar trend using Mulliken charge analysis,[137] (see Figure A3.2 in the appendix). As is typical for metals supported on hydroxylated oxides,[138] Pt-O bonding results in charge transfer from Pt to the silica support. The slope of the line in Figure 4.2a indicates significant charge transfer to the support of ~0.5*e* per Pt-O bond. Figure 4.2b shows a visual representation of Bader charge analyses, clearly indicating that the resulting effects on the electron distribution of Pt is local in nature; quantitative analysis of atomic charges for all NP systems of this study confirms these representative images (see Figure A3.3 in the appendix).

Positively charged metal atoms generally bind oxygen donors more strongly and oxygen acceptors more weakly.[124] Hence, a +0.5*e* charge is expected to significantly affect reactivity.[22] Although NP size does not affect the magnitude of charge transfer per bond, *NP size is expected to significantly impact catalytic properties* because the fraction of Pt surface sites that are

charged is inversely proportional to NP diameter. Interestingly, it has been observed on multiple occasions[102,139,140] that reactivity scales with NP-support interfacial perimeter; however, this has previously been attributed to explicit participation of the support in the reaction. *Our results suggest that a scaling of catalytic reactivity with the NP-support interfacial perimeter could, for some systems, be a result of catalyst-support interactions affecting the local electronic structure of the supported NP, without any direct participation of the support in adsorption or conversion of reactants.*

The d-band center (average energy of the d states) can be calculated from the projected density of states (PDOS). The d-band center has been shown to correlate with the strength of adsorbate binding on transition metals.[126,127] In addition, the d-band center has been shown to correlate with the coordination number of a metal active site, even for some unsupported transition metal nanoparticles.[12,15] These correlations provide one explanation for the observed correlation between adsorbate binding strength and active site coordination number observed on metals (higher coordination number corresponds to lower d-band center, and in turn, weaker adsorbate binding). Unfortunately, the latter of these correlations, relating electronic structure to coordination number, is not valid for Pt NPs supported on amorphous silica, as shown in appendix Figure A3.4. Pt atoms bonded to oxygen undergo electron donation to acceptor levels that are below the conduction band. [138] Furthermore, relaxation of NPs on the silica support results in significant distortion of the Pt lattice, giving a distribution of metal-metal bond lengths, even for a fixed coordination number. Two atoms having the same coordination number (defined by a cutoff distance) can thus have very different electronic structures. *As a result, the predictive power of coordination number is expected to diminish for small NPs supported on amorphous*

supports compared to more crystalline structures (i.e., larger NPs or those on crystalline supports).

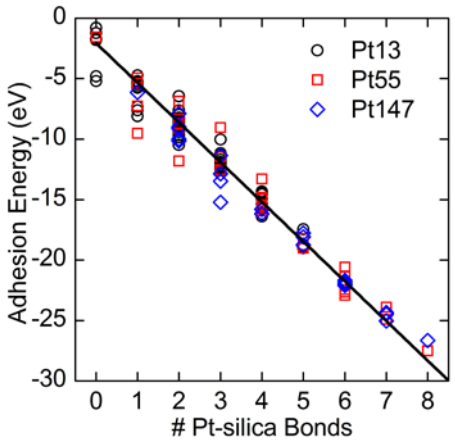

Figure 4.3. Adhesion energy vs number of Pt-silica bonds for Pt_{13}, Pt_{55}, and Pt_{147}. The line is a least-squares fit to the Pt_{13} data with regression equation y = -3.285x – 2.053 (R^2 = 0.965).

4.3.3 Silica surface hydroxyls strengthen nanoparticle adhesion.

When designing catalyst materials, thermal stability is of the utmost importance because even the most optimal activity and selectivity will be lost upon deactivation via catalyst sintering. However, an atomistic understanding of how support materials stabilize NPs is generally lacking,

and there are competing theories explaining observations regarding catalyst sintering.[11,100,141] Campbell and coworkers showed in a series of experiments and empirical modeling studies that the sintering rate is directly dependent on the NP adhesion energy, whether sintering occurs via agglomeration or Ostwald ripening.[11,17] Deformation energies for the systems in this work are small enough (see Figure A3.5) that they do not affect the general trends of adhesion energy vs number of Pt-silica bonds, i.e., the approximated adhesion energy, E_{adh}, can be defined as

$$E_{adh} = E_{Pt-S} - E_{Pt}^{fixed} - E_{S-H}^{fixed} \quad (4.1)$$

where E_{Pt-S} denotes the energy of the NP bound to the silica support, with all atoms relaxed. E_{Pt}^{fixed} and E_{S-H}^{fixed} denote the energies of the NP and support fixed in the relaxed geometries of the Pt-support system. Note that if H atoms were removed from the support surface during the binding procedure then E_{S-H}^{fixed} involves a surface with dangling bonds.

Figure 4.3 shows that adhesion energy is linearly dependent on the number of Pt-silica bonds, indicating that Pt-O bonds are significantly stronger than the net van der Waals force between Pt and silica, as expected. The number of Pt-O bonds is governed by the silica surface hydroxyl density, which can be easily modified by simple calcination prior to NP synthesis, i.e., through the pre-treatment temperature of the silica support. *This suggests that our previous prediction, that stability of silica-supported NPs can be tuned via the pre-treatment temperature of the amorphous silica support,*[130] *is not limited to sub-nm clusters.*

4.3.4 Pt_{13} results can be used to predict properties of larger NPs.

Both charge transfer and adhesion energy depend linearly on the number of Pt-O bonds (see Figures 4.2 and 4.3). Furthermore, the value of the dependent variable (net charge or adhesion energy) in both cases is independent of NP size. To demonstrate this we determined the linear least-squares best fit lines to the Pt_{13} data in Figures 4.2a and 4.3 and calculated the corresponding coefficients of determination (R^2) relating those lines to only the data points for each NP size. The resulting R^2 values, shown in Table A3.2, are close to unity. Consequently, the properties of larger NPs supported on amorphous silica can be predicted to a high degree of confidence based only on the results of Pt_{13} and the distribution of number of Pt-O bonds for the larger NP in question. Because we defined Pt-O bonding based on number of dissociated hydroxyls upon adsorption, the numbers of Pt-O bonds in the plots above were determined in the adsorption step, which requires only very efficient DEM simulations. In contrast to the costly DFT calculations used to explicitly calculate electronic structure and energetics. These DFT calculations require on the order of days per system using 64 CPUs. In contrast, the DEM simulations used in the adsorption step were completed in seconds using a single CPU. This allowed us to sample the surfaces of all five amorphous silica structures, previously developed by us,[103] as functions of temperature, with a very fine grid spacing.

We have combined the data on the number of Pt-silica bonds computed from DEM as a function of NP size and hydroxyl density with correlations relating the electronic structure and energetics computed from DFT to the number of Pt-silica bonds. These correlations can be used to produce models for the net NP charge and NP adhesion energy as functions of the silica pre-treatment temperature. These predictive correlations are shown in Figure 4.4. Figure 4.4a predicts the net charge on NPs of three different sizes as a function of the silica pretreatment

temperature. Similarly, the adhesion energy as a function of NP size and T_{pre} is given in Figure 4.4b. *More importantly, we can generate predictive curves like this for other NP sizes and shapes by carrying out very simple DEM calculations; no DFT calculations are needed.* We expect these relationships to hold for much larger NPs because our PDOS calculations indicate that Pt_{147} is metallic, demonstrating that the correlations apply to larger metallic NPs as well.

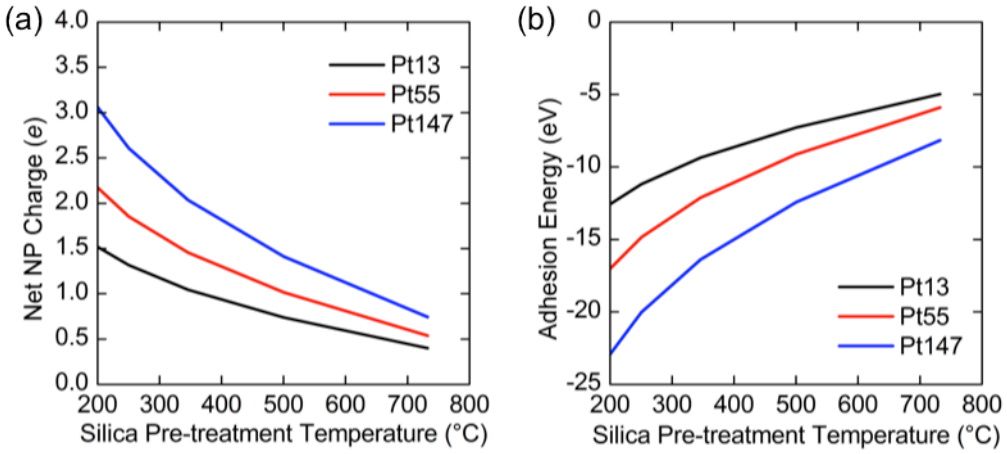

Figure 4.4. (a) Net charge on Pt NPs as a function of silica pre-treatment temperature. (b) Adhesion energy as a function of silica pre-treatment temperature for Pt_{13}, Pt_{55}, and Pt_{147}.

4.4 CONCLUSIONS

An atomistic understanding of how support materials affect the properties of catalytic nanoparticles should provide a set of design rules that can be used as a guide for developing novel or improved catalytic materials. Utilization of such design rules, however, also requires the development of more efficient predictive screening methods.

We have extended our methodology for generating NP-support models to study the effects of amorphous silica surfaces on supported Pt NPs as a function of NP size. Our results indicate that both the net charge on the NP and the adhesion energy are linear functions of the number of Pt-silica bonds formed during NP adsorption. Furthermore, the number of Pt-silica bonds can be estimated from the NP geometry and the silica surface hydroxyl density. Both the net charge and adhesion energy are important physicochemical properties, because the reactivity for nucleophilic/electrophilic reactants can be expected to scale with charge, and adhesion energy is directly related to NP sintering resistance.[11]

It has been previously noted that, for some supported NP systems, reactivity scales with NP-support interfacial perimeter.[102,139,140] Our results show that charge transfer from Pt to silica can significantly affect the local electronic structure of Pt surface sites at the Pt-silica perimeter. This suggests that reactivity scaling with NP-support interfacial perimeter may *not* be due to participation by the support material, but can rather be a purely electronic effect resulting from metal-support interactions.

We furthermore showed that the results obtained from DFT calculations of Pt_{13}/SiO_2 can be used to accurately predict the DFT results of larger Pt NPs using only additional DEM calculations, which are fast and simple to implement. This importantly circumvents the need for computationally expensive DFT calculations and could allow for the study of larger NPs than

could be studied purely from DFT. In future work we will expand this approach to other NP shapes as well as NP and support compositions.

5.0 PREDICTING CATALYST-SUPPORT INTERACTIONS BETWEEN METAL NANOPARTICLES AND AMORPHOUS SILICA SUPPORTS

The content of this chapter is taken from C. S. Ewing, G. Veser, J. J. McCarthy, J. K. Johnson, and D. S. Lambrecht, "Predicting Catalyst-Support Interactions between Metal Nanoparticles and Amorphous Silica Supports", in preparation.

5.1 INTRODUCTION

Control over nanoparticle (NP) catalyst-support interactions may offer a promising tool for tuning catalytic properties; however, at present, accurate prediction of these interactions is daunting. Furthermore, support effects are becoming increasingly important as catalytic materials research has begun to shift towards ever more complex support materials. Yet, despite significant progress in atomistic modeling methods, explicit inclusion of support effects remains a challenge.[7,8]

Amorphous silica is a commonly used catalyst support due to its good thermal stability as well as tunable porosity and surface area. [28,29] Additionally, the chemical and physical properties of silica can be further controlled via doping with transition metals such as Ti, [42,142-149] making it an attractive material for tuning catalyst-support interactions. Prediction of support effects of

amorphous surfaces, however, requires calculation of a broad distribution of catalyst-support interactions because amorphous supports exhibit a range of local surface structures.

We recently developed an approach for rapid prediction of NP-support interactions between Platinum and amorphous silica.[150] We developed linear correlations for the adhesion energy and net charge on a NP as a function of the NP size and silica support hydroxyl density based on density functional theory (DFT) calculations for a small set of Pt NPs. We demonstrated that these correlations are able to predict adhesion energies and charges for other Pt NPs through the use of fast discrete element method (DEM) simulations to predict the number of Pt-silica bonds. Here, we extend our methodology to NPs having different shapes and compositions. Specifically, we demonstrate that (a) correlations obtained for 13 atom Pt clusters are valid for NPs of larger sizes and different NP geometries, and (b) this approach can be successfully applied to other catalytic metals such as Pd, Au, Ni, and Fe NPs.

5.2 METHOD

5.2.1 Model amorphous silica surfaces.

We used periodic amorphous silica surface structures constructed from a model developed by Ewing *et al.*[103] to investigate NP-surface interactions. These model surface structures are based on first-principles simulations and have been found to accurately predict hydroxyl density and distribution of hydroxyl groups as a function of temperature without any adjustable parameters.[103] Five distinct model surfaces were generated and the hydroxyl density of each system was adjusted using an algorithm to mimic a range of silica pretreatment temperatures

T_{pre}, resulting in a total of 56 different surface structures.[103] For the DFT calculations in this work, we use two of these surface structures having high (4.5 nm^{-2}) and low (1.6 nm^{-2}) hydroxyl densities, corresponding to low (200 °C) and high (570 °C) T_{pre}, respectively. For the discrete element method calculations described below we use all 56 surface structures. Details of unit cell dimensions and system sizes can be found in the Supporting Information.

5.2.2 Metal nanoparticles.

For the majority of calculations in the present study we used magic number cuboctahedral NPs because the symmetry is independent of size. To investigate the effects of NP geometry on the catalyst-support interactions we also used a theoretical global minimum configuration for Pt_{13},[107] and "slab" Pt_{55} and Pt_{147} (elongated in the *y* dimension; 3 atomic layers thick). All NP geometries used in this study are shown in Figure 5.1. To calculate electronic structure correlations for NPs of different metals we used 13-atom cuboctahedral NPs of Au, Pd, Fe, and Ni and 147-atom cuboctahedral NPs of Au and Pd.

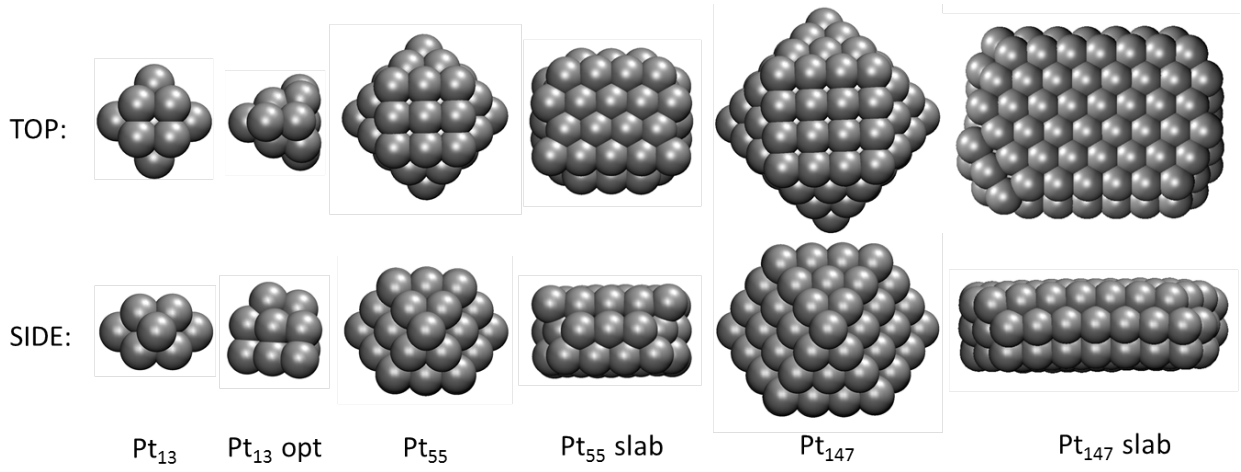

Figure 5.1: Top and side views of the NP geometries used in this study, from left to right: cuboctahedral Pt_{13}, theoretical gas phase global minimum Pt_{13} cuboctahedral Pt_{55}, slab Pt_{55}, cuboctahedral Pt_{147}, and slab Pt_{147}.

5.2.3 Simulating NP adsorption.

We divided each silica surface into grids to sample different adsorption locations on the surface. To calculate linear correlations using DFT, silica surfaces for 13-, 55-, and 147-atom NPs (of a given composition, geometry, and orientation) were typically divided into grids of 9 (3×3), 9 (3×3) and 6 (3×2) adsorption locations, respectively. Linear correlations relating adhesion energy and net charge to number of NP-silica bonds can be calculated based on a relatively small sample of configurations (e.g., 18 systems); however, all possible adsorption locations should be sampled for prediction of catalyst-support effects based on NP and support properties. To demonstrate how DEM simulations can be used to efficiently compare properties of different NP

sizes/geometries, we thus divided each silica surface into grids of 80 (10×8) adsorption locations. Specific details about the division of cells into grid points are provided in the Supporting Information.

We simulated the adsorption of NPs onto the silica surface using discrete element method[110] (DEM) simulations followed by DFT calculations, as described in detail previously.[130] The DEM simulations were used to generate reasonable initial structures for the placement of NPs on the silica surface and to compute an estimate for the number of metal-silica bonds. For the purpose of our study, the forces in DEM were limited to only gravity, hard-sphere interactions, [115] and tangential friction, where rebounding of particles (atoms) is completely avoided by tuning the viscoelasticity of the particles in the simulations. It is known experimentally that metal (M) NPs supported on silica form bonds between the metal and silica surface through Si-O-M linkages. .[100,119,134] We model M-O bond formation by creating bonds between the NP and any surface hydroxyls that are in contact with metal atoms in the NP by removing the H atom from those hydroxyl groups and reducing the hard-sphere interactions between the interacting M and O atoms to their covalent rather than van der Waals (vdW) radii. The DEM-initialized geometries were fully relaxed to their local minima using DFT for a select group of systems. In addition, many other NP structures were generated on each of the 56 silica surface structures using DEM in order to more fully explore the number of metal-silica bonds as a function of NP size and geometry (see below).

5.2.4 Density functional theory calculations.

All DFT calculations performed in this work used the CP2K code, which employs a Quickstep[78] implementation of the DFT method using a combination of plane waves and pseudopotentials

with localized gaussian basis sets (see Supporting Information for details). We used the revised PBE functional (revPBE)[104] and GTH pseudopotentials[81,82] in conjunction with short range double-ζ basis sets with polarization functions (SR-DZVP)[105] in our calculations. vdW interactions were included using the DFT-D3 method.[151] All surface slabs were relaxed using CP2K with supercells that were periodic in all directions with at least 20 Å of vacuum between periodic images in the *z* dimension to mitigate interactions between the periodic images of the surface slabs. The plane wave energy cutoff, basis sets, vacuum spacing and spin-restricted relaxation for these systems have been validated for these systems previously.[130]

5.2.5 Calculating nanoparticle properties.

NP adhesion energy and net charge are primary components of this study. We approximate the adhesion energy as the instantaneous pull-off energy of the NP from the support. Deformation energies for these systems have been shown to be small enough that they do not affect the general trends of adhesion energy vs number of Pt-silica bonds. We therefore calculated adhesion energy, E_{adh}, as follows

$$E_{adh} = E_{Pt-S} - E_{Pt}^{fixed} - E_{S-H}^{fixed} \quad (1)$$

where E_{Pt-S} denotes the energy of the NP bound to the silica support, with all atoms relaxed. E_{Pt}^{fixed} and E_{S-H}^{fixed} denote the energies of the (separated) NP and support fixed in the relaxed geometries of the Pt-support system. Note that if H atoms were removed from the support surface during the binding procedure then E_{S-H}^{fixed} involves a surface with dangling bonds. Atomic partial charges

were calculated using Bader charge analysis on valence electron density cube files generated using CP2K. [135,136] Net NP charge is simply the sum of NP atom partial charges.

5.3 RESULTS AND DISCUSSION

5.3.1 Adhesion energy and charge predicted from hydroxyl density and NP size/geometry.

In previous work we developed linear correlations relating both adhesion energy and net NP charge to the number of Pt-silica bonds for cuboctahedral Pt_{13} clusters. We furthermore showed that the correlations calculated from Pt_{13} data accurately predict the adhesion energies and NP charges for cuboctahedral Pt clusters containing 55 and 147 atoms.[150]

In the present work we have computed adhesion energies and NP charges for Pt_{13} clusters initially having the gas phase ground state structure[107] and for Pt_{55} and Pt_{147} clusters having a slab geometry. Figure 2b shows that the linear correlation of net charge vs number of Pt-O bonds calculated for cuboctahedral Pt_{13} accurately predicts the net charge of other 13-, 55-, and 147-atom Pt NPs, regardless of NP geometry. To quantify this result, we calculated coefficients of determination (R^2) relating the data points of each NP size and geometry to the linear least-squares best fit lines of the cuboctahedral Pt_{13} charge data. The resulting R^2 values (shown in Supporting Information Table S1) are all close to unity, indicating that our approach can be successfully applied to the calculation of net charge transfer using correlations from Pt_{13} data to other Pt NPs, regardless of NP size or geometry. Unfortunately, extrapolation of the adhesion energy correlation is not as straightforward.

A plot of adhesion energy vs number of Pt-O bonds (see Figure A4.1) shows that the adhesion energies of Pt_{147} slab geometry deviate significantly from the line fit to Pt_{13} adhesion energies. Results of DFT-D3 calculations using CP2K report vdW energies explicitly, which we used to calculated the contribution of vdW energy to the adhesion energy as

$$E_{adh,vdW} = E_{Pt-S,vdW} - E^{fixed}_{Pt,vdW} - E^{fixed}_{S-H,vdW} \quad (2)$$

The significant deviation of Pt_{147} slab adhesion energies from the linear correlation calculated for cuboctahedral Pt_{13} is due to substantially larger vdW adhesion energies for Pt_{147} slab (5.6 eV) than Pt_{13} (-1.4 eV). Contributions to adhesion energy from vdW forces is dependent on the Pt-silica interfacial area rather than the number of bonds. As a result, differences in vdW adhesion energy correspond to a shift in the y-intercept, and not the slope, of the adhesion energy plotted against number of Pt-O bonds. The vdW adhesion energies of cuboctahedral Pt_{13} and Pt_{147} differ by only 1.5 eV, which is approximately half the energy of a Pt-O bond, and less than the standard deviation of the adhesion energy vs number of Pt-O bonds (Figure 5.2a). The correlation relating adhesion energy and number of Pt-O bonds is thus only universal for NP geometries with similar values of $E_{adh,vdW}$. In order to predict adhesion energies based on the correlations calculated for cuboctahedral Pt_{13}, we calculate adhesion energy as:

$$E_{adh} = E_{adh,vdW} + E_{adh,non-vdW} \quad (3)$$

Figure 5.2a shows the Pt-silica adhesion energies after subtracting out vdW adhesion energies. Figure 5.2a shows that the non-vdW adhesion energy as a function of the number of Pt-

O bonds for of the new Pt NP geometries are predicted by the Pt_{13} correlation with remarkable accuracy. Calculated R^2 values relating the data in Figure 5.2a and the best fit line of cuboctahedral Pt_{13} non-vdW adhesion energy were close to unity (Appendix Table A4.1). Thus, our approach can be successfully applied to the calculation of non-vdW adhesion energy using correlations from cuboctahedral Pt_{13} data to other Pt NPs, regardless of NP size or geometry.

For simple calculation of vdW adhesion energy, we propose a simple approximation relating $E_{adh,vdW}$to the number of metal atoms on the bottom-most layer of a NP. The linear fit of $E_{adh,vdW}$ as a function of the number of interfacial metal atoms for all Pt cluster geometries in Figure 5.1 (see Figure A4.2) can be used to predict vdW adhesion energies for NPs of any shape or size. The total adhesion energy is then calculated by adding $E_{adh,vdW}$ for a given NP geometry to adhesion energy calculated from the correlation in Figure 5.2a.

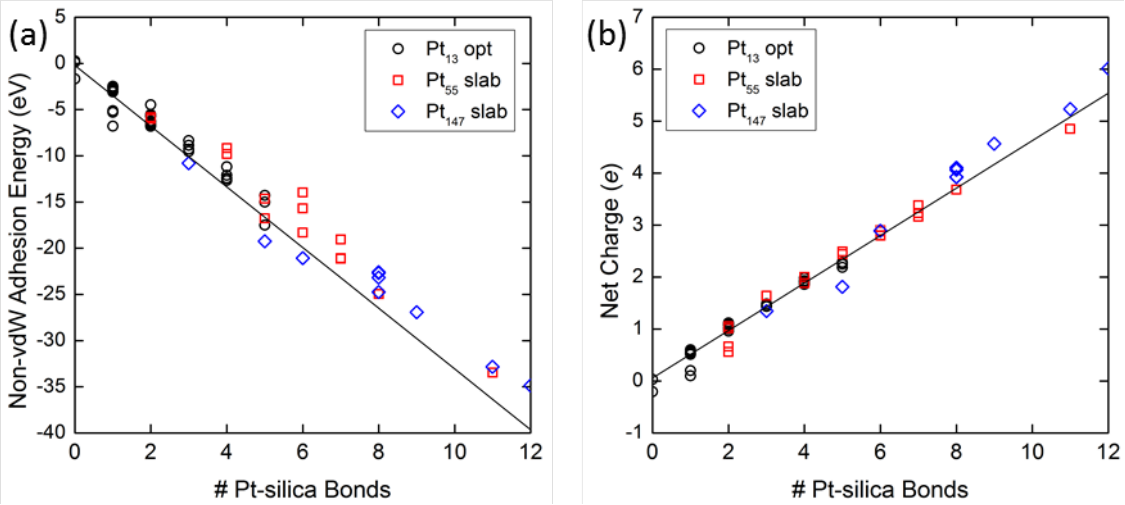

Figure 5.2: (a) Non-vdW adhesion energy and (b) NP net charge as a function of number of Pt-O bonds. The lines are predictions based on correlations from DFT calculations on cuboctahedral Pt_{13} NPs.

5.3.2 Predicting favorable NP geometries.

In order to model supported NPs with DFT calculations, the initial NP structure must be known. This is because *ab initio* molecular dynamics simulations are computationally expensive, and reconstruction of metal nanoparticles occurs on a relatively slow timescale. By calculating the relative energy of different NP geometries, however, the energetically favorable structure for a specific set of conditions (e.g., NP size and silica hydroxyl density) can be determined.

As a simple example, we calculated system energies referenced to the corresponding bulk Pt energy, E_{sys}, of cuboctahedral and slab geometries, of both Pt_{55} and $Pt_{147,}$ on 56 amorphous

silica surfaces representing a range of pretreatment temperatures (Figure 5.2). Here E_{sys} is defined as

$$E_{sys} = \frac{E_{adh}+E_{NP}}{n} - E_{bulk} \quad (4)$$

where E_{adh} is adhesion energy (including vdW adhesion energy), E_{NP} is total energy of the unsupported NP, n is the number of atoms in the NP and E_{bulk} is the energy of a single metal atom in the bulk phase. We exclude the deformation energies of both Pt and silica because they were shown to be small compared to E_{adh}.[152] The third term on the right hand side of eq 2 (E_{bulk}) is a constant. Hence, the relative energy is a balance between the energy of the NP geometry and adhesion energy.

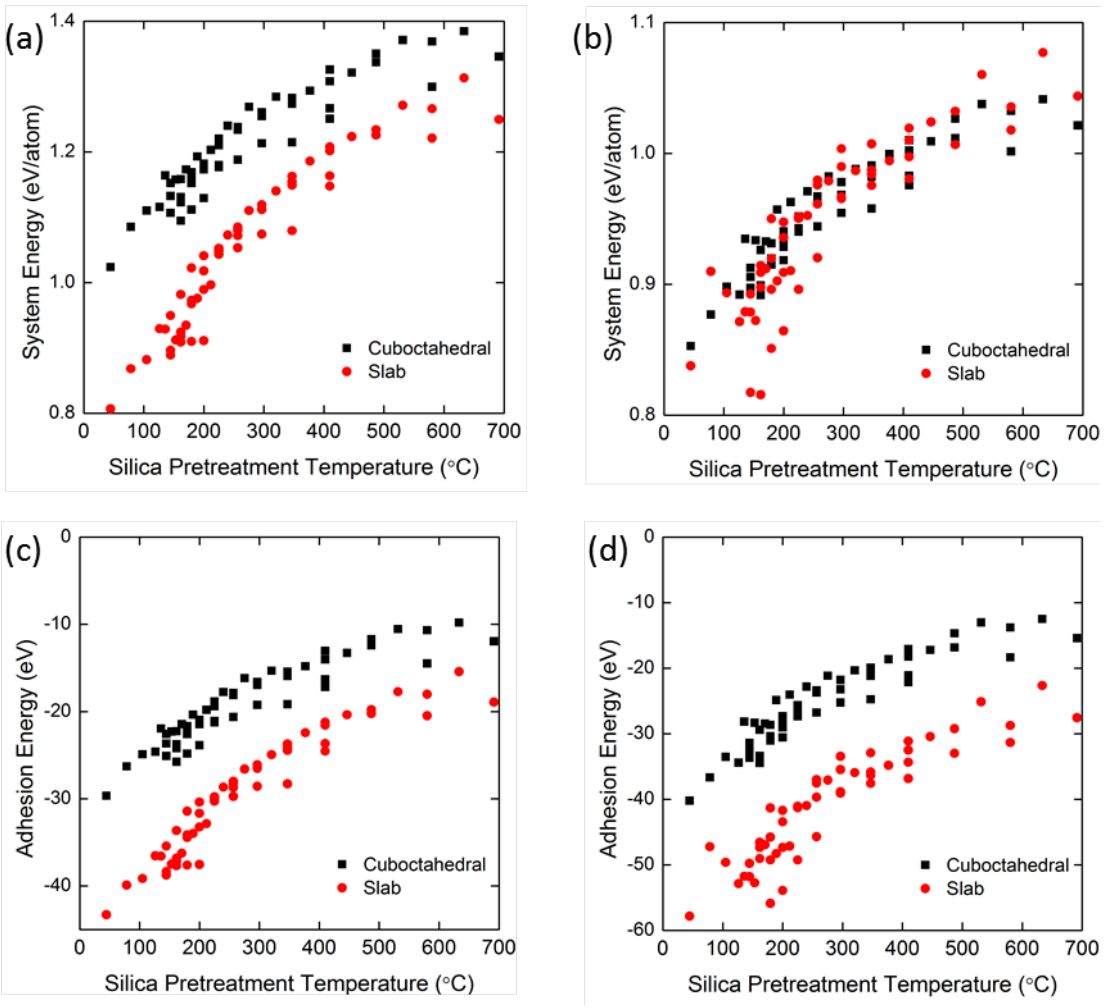

Figure 5.3. Nanoparticle energy plus adhesion energy normalized by corresponding bulk energy for cubeoctahedral vs slab (a) Pt_{55} and (b) Pt_{147}. Adhesion energy for cubeoctahedral vs slab (a) Pt_{55} and (b) Pt_{147}.

Figure 5.3a shows that, for Pt_{55}, the slab geometry is energetically preferred over cuboctahedral, regardless of silica pretreatment temperature. The total energy of unsupported slab Pt_{55} is 1.7 eV higher than cuboctahedral Pt_{55}, which is about the same magnitude as half of a Pt-O bond. However, slab Pt_{55} averages between 1.3 and 4.3 more Pt-O bonds over the entire range of silica surfaces than cuboctahedral P_{55}, so that the difference in adhesion energy is significantly greater than the difference between NP energies. Figure 5.3b shows that although the slab geometry of Pt_{147} results in significantly more bonds, the two geometries have very similar normal energies because E_{NP} for cuboctahedral Pt_{147} is 15.5 eV lower in energy than slab Pt_{147}. Note that all NP energies are positive, indicating that the bulk metal is still thermodynamically favorable to the supported nanoparticle despite strong NP-support adhesion.

Although we are not able to calculate energy barriers for NP reconstruction using this approach, we can gain important insight from the values of E_{norm}. In the above example, we can expect Pt_{55} to flatten to a 3-layer NP due to Pt-silica interactions, although we cannot determine at what temperature this will occur. Furthermore, Pt_{147} is only energetically favorable in a slab geometry over a cuboctahedral geometry on low T_{pre} silica. We therefore predict that if Pt_{147} is synthesized as cuboctahedral NPs, they will likely not wet amorphous silica supports. While slab Pt_{147} becomes energetically comparable to cuboctahdral Pt_{147} at low T_{pre}, the higher temperatures required to facilitate the cuboctahdral-to-slab NP reconstruction would result in higher T_{pre} values, and hence, prefer more compact, bulk-like NPs over a spread-out slab-like NP.

Calculation of the normal energies discussed above can be used to determine thermodynamically favored NP geometries; however, sintering by agglomeration is governed by the rate of NP diffusion, and hence NP adhesion energy.[11] Figures 5.3c and 5.3d show that both Pt_{55} and Pt_{147} are more stable against agglomeration in~~s~~ the slab geometry than cuboctahedral,

despite higher E_{NP}. This comparison of system and adhesion energies between cuboctahedral and slab geometries serves to demonstrate the predictions one can make using the proposed methodology. In future work, we will apply this approach to the screening of a range of NP geometries to predict favorable NP geometries and their relative resistance to sintering.

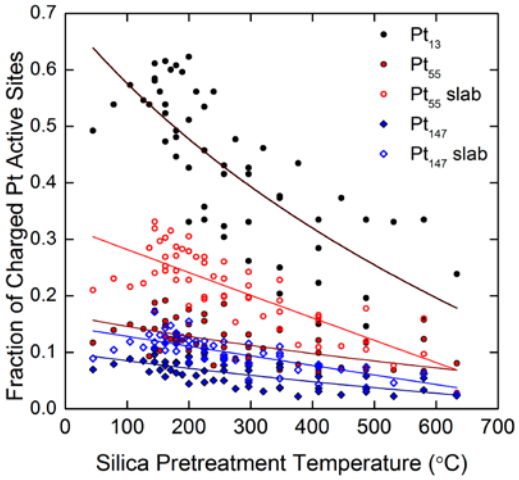

Figure 5.4: Relative fraction of charged surface Pt atoms for Pt_{13}, Pt_{55} cuboctahedral, Pt_{55} slab, Pt_{147} cubeoctahderal and Pt_{147} slab as function of silica pre-treatment temperature. Each data point is the average value of fraction of charged sites for 80 adsorption locations on a single silica surface. Logarithmic fits show general trends in the data.

5.3.3 Predicting effects of NP-support charge transfer.

With knowledge of reactant adsorption strength as a function of transition metal site partial charge, the same general approach can be used to predict the effects of Pt-silica charge transfer on catalytic reactions. For example, weaker CO adsorption is expected to result in increased reactivity for CO oxidation over Pt.[12] We recently showed that Pt-O bonds result in ~0.5 *e* charge transfer from metal to silica, resulting in a positive partial charge on the O-bonded Pt atom. The rate increase of CO oxidation over Pt due to charge transfer should hence be proportional to the fraction of *active* sites that are bonded to the silica support, which depends on (a) the silica hydroxyl density *and* (b) the circumference of the NP-support interface. The silica hydroxyl density dictates what fraction of Pt atoms is bonded to silica at the NP-support interface, and the circumference of interfacial contact is proportional to the number of atoms that can be bonded to silica *and* accessible by gas molecules.

Figure 5.4 shows the fraction of *active* sites that are positively charged due to Pt-O bond formation for Pt_{13} and both cuboctahedral and slab geometries of Pt_{55} and Pt_{147}. Pt_{13} relaxes significantly on amorphous silica supports exposing almost all atoms to gas phase reactants.[152] As a result, a large fraction of Pt atoms are positively charged (over half on low T_{pre} silica). These results suggest that the optimization of Pt/SiO_2 catalyst for CO oxidation is achieved by minimizing NP size and maximizing silica hydroxyl density.

5.3.4 Linear correlations apply to other metals.

To test the transferability of our approach, we relaxed 13-atom Au, Pd, Ni, and Fe clusters, as well as 147-atom Au and Pd, supported on amorphous silica. Figure 5.5 shows that as with Pt,

both non-vdW adhesion energy and net charge are linearly related to the number of NP-support bonds. Furthermore, as with Pt, linear correlations determined using 13-atom calculations are sufficient to obtain good estimates for corresponding 147-atom NPs. The slopes of non-vdW adhesion energy curves vary significantly among the metals studied (Figure 5.5a). The metal-oxygen bond strengths (i.e., adhesion energy per bond) correlate with the experimentally measured heat of formation of the corresponding metal oxide (see Figure A4.3).[11,153,154] Because iron has multiple oxide forms, we averaged the different heats of formation, each normalized by the respective number of Fe-O bonds, as follows:

$$\Delta H_{f,\mathrm{Fe\ Oxide}} = \frac{\Delta H_{f,FeO} + \frac{2}{3}\Delta H_{f,Fe_2O_3} + \frac{4}{3}\Delta H_{f,Fe_3O_4}}{3} \quad (3)$$

As expected, Au binds most weakly to silica whereas Fe has relatively strong adhesion energy. Based on our calculations, we predict that the effects of NP-silica interactions on NP stability will decrease in the following order Fe > Ni > Pd ~ Pt > Au. These results are qualitatively in agreement with experimental results from Campbell *et al.*[11] including the observation that Pd has slightly weaker adhesion energy than Pt, despite having a more negative oxide heat of formation. It is important to note that surface hydroxyls have been observed by adsorption calorimetry experiments to weaken adhesion;[11] however, our studies reflect very different experimental conditions. In particular, these experiments measure adhesion energy upon contact between NP and support whereas our models represent NPs bonded to the support after calcination. Figure 5.4b shows that charge transfer, however, does not significantly depend on NP metal composition. This is in agreement with previous experimental results, which

showed that metal nanoparticles on amorphous silica supports donate approximately 0.5 eV per bond.[138,155]

Ni_{13} and Fe_{13} have continuous band structures around the Fermi level, (see Supporting Information Figure A4.4) and hence their electronic properties—including metal-oxygen bond strength and charge transfer—are expected to be the same (per bond) as NP size is increased. Pd has slight discontinuity at the Fermi level, and that of Au_{13} is even more pronounced. We thus tested the effects of NP size on adhesion and charge correlations by generating 12 systems each of silica-supported Pd_{147} and Au_{147}. As with Pt NPs of different geometries, we tested the predictive power of Au_{13} and Pd_{13} by calculating coefficients of determination (R^2) for comparing linear least-squares best fits of adhesion energy and net charge for Au_{13} and Pd_{13} to data points from Au_{147} and Pd_{147}, respectively. Table S2 shows that despite the small number of 147-atom systems relaxed, the R^2 values are all close to unity. Finally, parameters for the correlations relating adhesion energy and net charge to number of bonds for Pt, Pd, Au, Ni, and Fe are shown in Table S3 and S4, respectively.

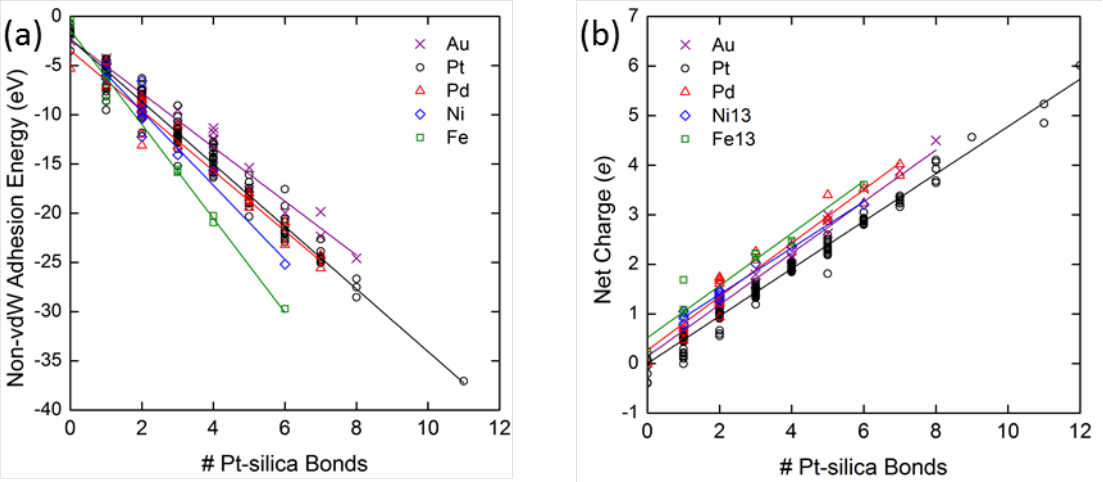

Figure 5.5: Adhesion energy (a) and NP charge (b) as a function of number of M-O bonds, for Pt, Pd, Au, Ni, and Fe. Fits for all data available (13, 55, and 147 atom systems).

CONCLUSIONS

The ability to predict NP catalyst-support interactions offers potential dial for the rational design of catalytic materials. These interactions can be exploited to tune both catalytic activity[156,157] and stability[42,147-149] of supported NPs. Herein we demonstrate that linear correlations calculated from 13-atom clusters using DFT can be used to predict the adhesion energy and net charge for NPs of larger size. Furthermore, by separately accounting for vdW adhesion and bond energies, this approach can be successfully extended to NPs of various geometries.

Although the dynamics of NP reconstruction are computationally prohibitively costly, thermodynamically favorable NP geometries for a given NP size and silica preparation temperature can be determined using this approach. Furthermore, the relative stability of

different NP sizes/geometries can be estimated by screening with fast DEM simulations. Additionally, we show how this approach can be used to predict the effects of support interactions on electronic properties of supported NPs, and hence catalytic activity. Finally, we have demonstrated that, this methodology is transferrable to metals other than Pt, and we provide linear correlations relating adhesion energy and NP net charge to number of M-O bonds, for Au, Fe, Ni, and Pd.

6.0 IMPACT OF SUPPORT INTERACTIONS FOR SINGLE-SITE MOLYBDENUM CATALYSTS ON AMORPHOUS SILICA

The content of this chapter is taken from C. S. Ewing, E. G. Patriarca, A. B. Bagusetty, G. Veser, J. J. McCarthy, and J. K. Johnson, "Impact of Support Interactions for Single-Site Molybdenum Catalysts on Amorphous Silica", in preparation.

6.1 INTRODUCTION

Catalyst materials consisting of isolated metal centers dispersed on amorphous surfaces (silica and silica-alumina) are promising for a number of hydrocarbon reactions.[131,158] Such isolated metal center catalysts include: Mo(VI), W(VI), and Re(VII) supported on any of a number of oxides for olefin metathesis, Cr(VI) for olefin epoxidation, and oxide-supported V(V) for partial oxidation of methanol. Although many of these catalysts have been studied for decades,[131,158-166] the combination of amorphous support structure and single metal atom catalytic site has severely limited the information attainable via experiments.[30-33] Furthermore, first principles calculations of catalyst materials with amorphous surfaces have been prohibitively difficult,[131,158] until recently.[103,152] A better understanding of these catalyst materials will allow for catalyst optimization and may provide valuable insight for the development of similar catalyst materials for other reactions.

Primary challenges of modeling single atom catalysts on amorphous supports center on the difficulty of obtaining an accurate atomically resolved description of the active site. Unfortunately, isolated metal centers on amorphous supports cannot be accurately described using a single atomistic model structure. The local atomic structure varies significantly across amorphous silica surfaces.[103] As a result, individual single-atom sites on amorphous silica can differ dramatically in electronic structure, and hence stability and reactivity. It is therefore important for models of such systems to accurately capture the entire distribution of active sites because the reactivity of single-atom catalysts is likely dominated by few sites.[131,167]

Despite their shortcomings, ab initio models based on cluster models have allowed for tremendous advances in our understanding of isolated metal center catalysts.[31,131,159-161,167,168] Recently, Goldsmith *et al.* developed a novel approach for modeling isolated metal sites on amorphous supports, which accounts for surface structure heterogeneities.[131] This complex algorithm was used to calculate the low energy Mo/SiO_2 cluster model structure for a given ethene metathesis activation energy. Using this approach Goldsmith *et al.* calculated the average reactivity, based on a Boltzmann distribution of sites, and revealed clear correlations relating both reaction energy and Si-Si distance to ethene metathesis activation energy. Due to the size of the cluster model used, however, this method neglects the effects of local structure beyond the anchoring Si atoms on site energetics.

In this work we studied isolated Mo centers for ethene metathesis on recently developed realistic amorphous silica support structures using density functional theory (DFT) calculations. First, a method for rapid generation of Mo sites on model amorphous surface structures, based on constrained cluster model calculations, was developed. We then examined the effects of support structure on Mo site energy and reaction energy. Our results indicate that while many

correlations can be identified for the cluster model, explicit inclusion of the support material reveals a very complex structure-energy relationship. In particular, we show that both site and reaction energies depend more strongly on the O-Mo-O bond angle than Si-Si distance. In general, the complex interplay between site energy and surface structure is a result of the wide variation of hydrogen bonding, silanol types, bond lengths, and bond angles, many of which cannot be captured without explicit treatment of the surface.

6.2 METHOD

6.2.1 Model amorphous silica surfaces.

We used periodic amorphous silica surface structures constructed from a model developed by us[103] to study single atom Mo/SiO_2 catalysts. These model surface structures are based on first-principles simulations and have been found to accurately predict hydroxyl density and distribution of hydroxyl groups as a function of temperature without any adjustable parameters.[103] Five distinct model surfaces were generated and the hydroxyl density of each system was adjusted using an algorithm to mimic a range of silica pretreatment temperatures T_{pre}. The surface structures are 23.7 Å × 18.3 Å × ~12 Å comprising between 250 and 270 atoms. In this work, we use three different silica surface structures from each of the five distinct model surfaces, corresponding to T_{pre} values of 210, 340, and 540 ℃ and a total of 15 silica surfaces. Details of unit cell dimensions and system sizes can be found in the Supporting Information.

6.2.2 Generating isolated metal center sites.

In a recent theoretical study, it was determined that MoO_2 sites on amorphous silica are almost exlusively anchored to two silanol groups.[168] In order to obtain a distribution of surface sites, we first determined which silanols were within range to form a Si-O-Mo-O-Si structure. Based on the results of preliminary studies, we considered silanol pairs with Si-Si and O-O distances of less than 6.8 and 4.5 Å, respectively. We found that distances larger than these resulted in very high energies and/or unrealistic ending structures. A Mo site was generated at every silanol pair, based on the previously defined Si-Si and O-O cutoff distances. The details of site generation are explained in detail in the Results and Discussion.

6.2.3 Density functional theory calculations.

All atomistic calculations performed in this work used the CP2K code, which employs a Quickstep[78] implementation of the DFT method using plane waves/pseudopotentials and localized gaussian basis sets. Calculations used the PBE functional[80] and GTH pseudopotentials[81,82] in conjunction with short range double-ζ basis sets with polarization functions (SR-DZVP).[105] Van der Waals interactions were described using the DFT-D2 method,[169] which has been shown to accurately describe MoO_2.[170] All surface slabs were relaxed using CP2K treated as periodic in all directions with at least 20 Å of vacuum between periodic images in the *z* dimension to eliminate interactions between the periodic images of the surface slabs. The vacuum spacing for the silica surfaces has been validated previously.[130] Validation of the plane wave energy cutoff, plane wave energy relative cutoff, and basis sets can be found in the Supporting Information. (Figures A5.1, A5.2, and A5.3, respectively.)

6.3 RESULTS AND DISCUSSION

6.3.1 Generating low-energy isolated metal center sites.

To sample a wide distribution of surface sites, it is necessary to generate Mo sites at a large number of surface locations. The use of annealing for the generation of each surface site is therefore not practical. We hence limited our utilization of DFT in generating Mo sites to local relaxation. It is extremely important that the initial geometry for local relaxation is sufficiently accurate so that the system is not optimized to an incorrect local energy minimum. Generating the correct initial conditions for amorphous structures is particularly non-trivial because the energy landscape is disordered and hence often difficult to predict.

We developed a transferable method for generating low-energy Mo/SiO_2 sites, representing an intermediate structure in ethene metathesis, based on atom positions taken from cluster models. First, we generated two Mo/SiO_2 cluster models, shown in Figure 6.1: a six-membered Mo/SiO_2 cluster, denoted as bridged, and a minimal Mo/SiO_2 cluster model,[131] denoted as non-bridged. These two structures were chosen to represent Mo sites anchored to silanol groups that are directly connected via a siloxane bridge (bridged) and those that are not (non-bridged). Both cluster models are terminated with basis set deficient fluorine atoms, which mimic the size and electronegativity of oxygen atoms in an extended silica network.[131,158] Hence forth we will denote the Si atoms and their nearest neighbors as “anchoring” atoms and the remaining Mo site atoms as “moiety” atoms (shown explicitly, for cluster models, in Figure 6.1).

To sample a distribution of potential Mo sites, we mapped atom coordinates for cluster models having a range of Si-Si distances, obtained via optimization with fixed Si-Si positions. This procedure resulted in cluster models representative of a wide range of surface site

geometries, from which the positions of Mo moiety atoms relative to anchoring atoms can be extracted.

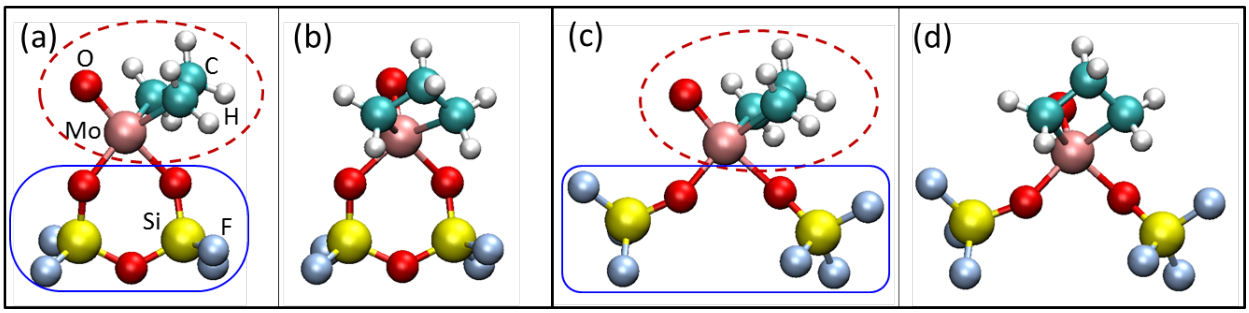

Figure 6.1. Bridged Mo/SiO_2 cluster model in the (a) trigonal bipyramidal and (b) square pyramidal geometries, and non-bridged Mo/SiO_2 cluster model in the (c) trigonal bipyramidal and (d) square pyramidal geometries. Atoms within the dashed line are denoted "moiety" and atoms within the solid blue line are denoted "anchoring".

After identifying silanol pairs on the silica surface models, we generated Mo sites based on the atomic positions of the corresponding cluster models (i.e., bridged or non-bridged and having similar Si-Si distance). First, hydrogen was removed from the anchoring silanol groups. Then, the distance between silanol group O atom positions was reduced to that of the corresponding cluster model. Using the anchoring O atoms and the Si-Si midpoint as a reference, the moiety atoms were then generated on the surface model with the same relative positions as those of the corresponding cluster model. As a result, the initial structures for geometry

optimization are relatively close to equilibrium. In order to avoid artifacts of slight non-equilibrium initial conditions, the moiety, Si atoms, and first neighbors were first relaxed while fixing the remaining atoms. Finally, the entire system was fully relaxed to a local minimum.

To test the reliability of this approach, we performed energy minimum searches for two of the Mo sites using *ab initio* molecular dynamics simulations. Each system was annealed at 750 K for 6 ps while holding all atoms fixed except for the moiety and anchoring atoms. After every 1 ps of simulation, a snapshot of the system geometry was taken and relaxed following the same procedure used for site generation (i.e., local atom relaxation followed by full system relaxation). In both cases, annealed structures had energies either higher than, or within 0.1 eV of structures obtained using our approach, confirming the effectiveness of our method (Figure A5.4).

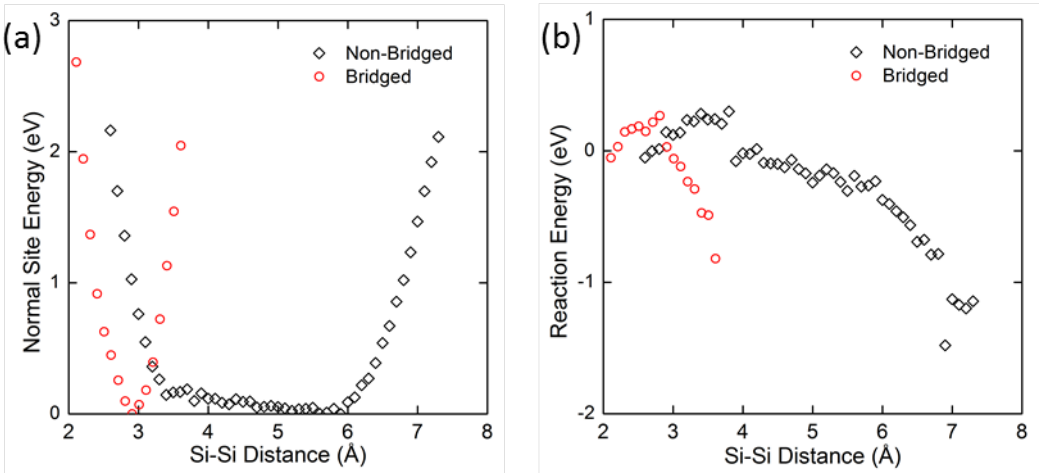

Figure 6.2. (a) Site energy as a function of Si-Si distance for Mo/SiO_2 cluster models, normalized by the lowest cluster energy. (b) Reaction energies as functions of Si-Si distance for Mo/SiO_2 cluster models.

6.3.2 Cluster model site energies are correlated with Si-Si distance.

Using the approach described above, we generated model systems representing two different off-pathway intermediates in ethene metathesis: the trigonal pyramidal and square pyramidal geometries. During ethene metathesis, Mo/SiO_2 sites can deactivate via metallacycle rotation from trigonal bipyramidal geometry to less active but more stable square bipyramidal geometry.[160,161] Figure 6.2a shows site energy as a function of Si-Si distance for both bridged and non-bridged cluster models in this study. Both cluster models are continuously dependent on Si-Si distance.

The energy profile of the bridged cluster is sufficiently explained by bond angles and the bond lengths, shown in Figure 6.3a and 6.3b, respectively. At small Si-Si distances, both the both Si-O-Si and O-Mo-O bond angles are compressed, resulting in increased site energy due to bond angle strain. As Si-Si distances increase, the siloxane bridge approaches linear and bond stretching results in increased site energies. Furthermore, as the siloxane bridge angle increases, the O-Mo-O angle is increased, due to steric hindrance, causing further steric hindrance with inter-moiety bonds.

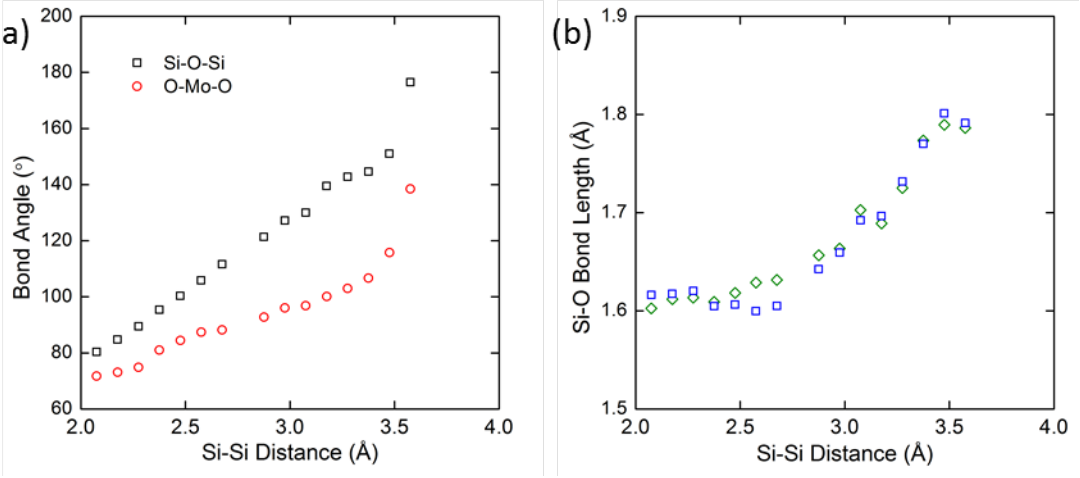

Figure 6.3. (a) Siloxane and O-Mo-O bond angles and (b) siloxane bond lengths vs Si-Si distance for the bridged cluster model.

The energy profile of the non-bridged cluster, however, is the result of different interactions. O-Mo-O bond angle and Si-O bond lengths for the non-bridged cluster are shown in Figure 6.4a and 6.4b, respectively. At small Si-Si distances, energy increases are not due to bond angle strain or bond compression, but rather to steric hindrance between F (i.e., O atoms in the silica network). At large Si-Si distances, the sources of rising site energy are increasing O-Mo-O angle and Si-O bond stretching, both due to stretching of the Si-O-Mo-O-Si unit. From Si-Si distances of about 3 to 6 angstroms, however, the site energy is relatively constant. Here the bond lengths and angles in the Si-O-Mo-O-Si unit remain near equilibrium because F atoms are free to rotate around Si to accommodate any Si-O configuration (except at very small Si-Si distances). On a real silica surface, the Si atoms are bonded to O atoms within the solid silica network, and hence do are not able to rotate freely. As a result, movement of Si bonded O atoms,

to accommodate a Mo atom, will result in bond angle strain and/or bond stretching, which are not accounted for in the non-bridged cluster model. While the bridged cluster model accounts for the expected phenomena that are expected to affect site energetics, the non-bridged cluster model neglects vital interactions that likely significantly impact calculated site energetics.

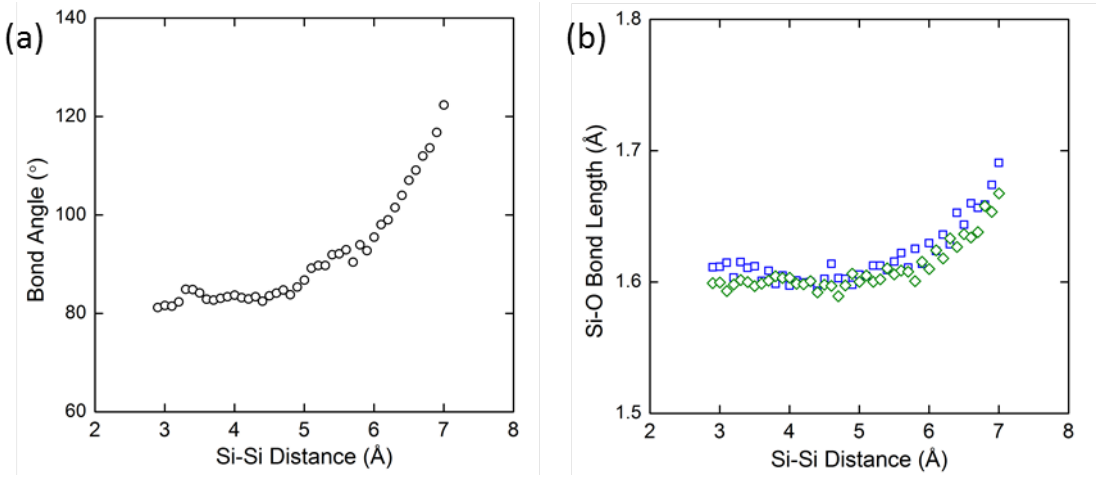

Figure 6.4. (a) O-Mo-O bond angle and (b) Si-O bond lengths vs Si-Si distance for the non-bridged cluster model.

Using a non-bridged cluster model, Goldsmith *et al.* showed that reaction energy is linearly related to ethene metathesis activation barrier. Reaction energies calculated for both clusters in this study are shown in Figure 6.2b. The energy profiles of bridged and non-bridged clusters are qualitatively similar. Due to the difference in site energy profiles, however, the reaction energy vs site energy curves are significantly different (Figure A5.5). In particular, low

energy bridged sites generally have higher reaction energy than low energy non-bridged sites. If the linear relationship between activation barrier and reaction energy for non-bridged clusters (activation barrier decreases with increasing reaction energy) holds for bridged sites, this indicates that bridged sites may be more active than non-bridged, on average.

6.3.3 Mo sites on periodic surface models.

To examine the effects the surface structure not accounted for by cluster models, we generated Mo sites on periodic amorphous silica surfaces. When heated, silanol groups are known to react with one another via condensation to form a water molecule and a siloxane bridge in a process called dehydroxylation.[33,53,171] As a result of dehydroxylation, both the number of silanol groups and the local structure of the silica surface changes.[33,53,103,171] It is thus likely that the properties of Mo sites may differ on silica surfaces that have been treated at different temperatures and hence undergone different degrees of dihydroxylation. Sites were hence generated at all possible anchoring locations on 15 different surface structures, which represent three average silica pretreatment temperatures (5 surfaces per temperature): 210, 340, and 540 °C.

For cluster models with a constant number of atoms, the relative stability of different sites can be calculated as the difference in system energies.[131] For sites on a surface, however, this definition does not suffice–even for different sites on the same surface–because the Mo moiety replaces atoms on the surface (OH groups). Typically, this problem is solved by calculating reaction energy where the net stoichiometry of the system is conserved. For example, the energy of gas-phase H_2 may be used to conserve stoichiometry to approximate the site energy as the reaction energy of:

$$moiety + surface \rightarrow \frac{moiety}{surface-2H} + H_2. \quad (1)$$

This definition corresponds to the energy of site formation; however, this does not necessarily correlate with site stability because the energy of a site at a given time is not history dependent. For example, if a Mo site forms at two silanols that are H-bonding with each other, the energy of site formation will be higher than if the silanols were not H-bonded. The increased formation energy is due an H-bond that is not present in the Mo/SiO_2 system, and hence should not have any effect on the stability of the system.

To compare site energies similar to the approach used for the cluster models, we calculated site energy as follows:

$$E_{site} = E_{Mo/SiO_2} - E_{SiO_2-OH} \quad (2)$$

where E_{Mo/SiO_2} denotes the energy of the Mo/SiO_2 system, with all atoms relaxed. E_{SiO_2-OH} denotes the silica surface, minus the two anchoring OH groups, fixed in the relaxed geometry of the bare silica surface (with all OH groups). By calculating the reference silica surface system without the anchoring OH groups, both moiety-silica interactions and moiety deformation are explicitly accounted for, and silica network deformation is estimated.

Figure 6.5 shows that the clear trends relating site and reaction energies to Si-Si distance are no longer applicable when explicitly modeling the silica surface. It is easy to distinguish between bridged and non-bridged sites, which have Si-Si distances of ~3 and > 3.5 Å, respectively. From Figure 6.5a it is clear that bridged sites have similar site energies as non-bridged sites; however, bridge sites are more likely to have significantly higher reaction energy

than non-bridged sites (Figure 6.5b). As a result, the average reactivity of bridged sites may differ significantly from non-bridged sites. Some of the sites for which the data are shown in Figure 6.5 are anchored to the same silanol group. Such Mo sites therefore cannot coexist. Using a simple Monte Carlo calculation, we simulated the formation of Mo/SiO_2 sites to estimate the ratio of bridged to non-bridged sites as a function of silica pretreatment temperature. Silica pretreatment temperatures of 200, 400, and 600 ℃ had 33, 28, and 15% bridged sites, respectively. We therefore predict that the effects of higher reaction energy will decrease as a function of silica pre-treatment temperature.

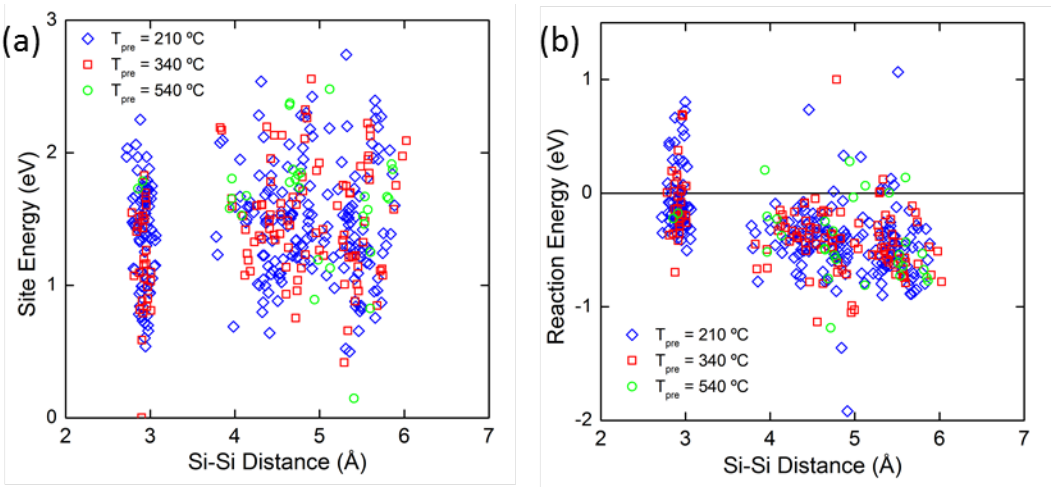

Figure 6.5. (a) Normal site energy as a function of Si-Si distance for Mo sites on full silica surface models. (b) Reaction energy as a function of Si-Si distance for Mo sites on full silica surface models.

Based on the results of cluster calculations, we hypothesized that O-Mo-O bond angles significantly impact Mo site energetics. The distance between anchoring O atoms is directly related to the O-Mo-O bond angle. Figure 6.6 shows contour plots of site energies and reaction energies for both cluster and surface models. For direct comparison, we limit the cluster model results to those with Si-Si distances observed on the full surface models. The cluster models show significantly less variation in magnitudes of both site and reaction energies than surface models. It is also clear from Figures 6.6a and 6.6b that both site energy and reaction energy generally vary more as a function of O-O distance than Si-Si distance.

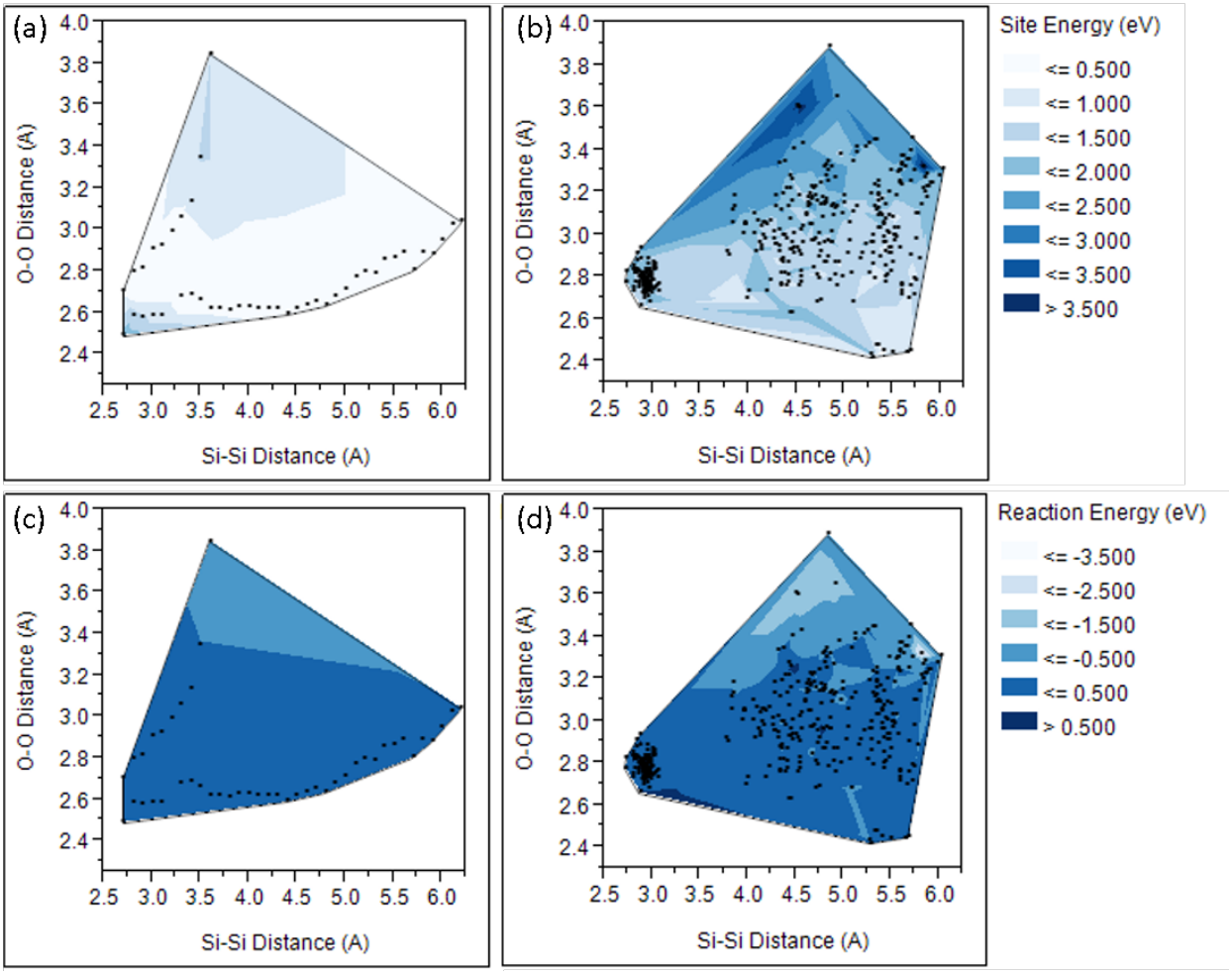

Figure 6.6. Contour plots relating calculated energies to Si-Si distance and O-O distance. Site energies for (a) cluster models and (b) surface models and reaction energies, for (c) cluster models and (d) surface models. Both bridged and non-bridged sites are included in all four contour plots.

Surface model calculations indicate that smaller O-O distances correspond to increased site stability. This can be rationalized by smaller O-Mo-O angles resulting in less steric hindrance with the moiety atoms than larger angles. Furthermore, sites with smaller O-Mo-O angles have higher reaction energies. This is because while the 'reactant' energy is significantly affected by O-Mo-O angle, the 'product' less sensitive to this because while $O{=}Mo{-}C_3H_6$ is parallel to O-Mo-O in the trigonal bipyramidal geometry, it is perpendicular in the square bipyramidal geometry. Smaller O-Mo-O angles thus lead to lower 'reactant' energies and hence increased reaction energies.

6.4 CONCLUSIONS

Amorphous surfaces exhibit a wide distribution of surface structures. An accurate description of catalysts supported on amorphous surfaces must therefore capture an entire distribution of surface sites. Recently, methods for generating cluster models that account for such a distribution have been developed.[131,167] In order to understand the limitations of such models, we examined commonly used Mo/SiO_2 cluster models[131,160,161] having a distribution of Si-Si distances. Our results indicate that an accurate model of Mo/SiO_2 catalysts should include both bridged and unbridged sites because they're energetics are dependent on very different properties. Furthermore, a non-bridged cluster model that represents the silica surface as only anchoring Si atoms their nearest neighbors does not accurately represent the real physics of Mo/SiO_2 sites.

Energetically accurate atomistic models of amorphous silica surfaces were recently developed.[103] We developed a *transferable* method for generating a large number of isolated metal atom sites on these amorphous surfaces based on constrained cluster calculations. This

approach could be applied to the development of other atomistic models of other isolated metal center catalysts on amorphous surfaces. Finally, using previously developed model surface structures, we have studied isolated Mo center catalysts on periodic amorphous silica surface models. Our results indicate that the O-Mo-O bond angle plays a crucial role in determining the Mo site energies and metallacycle reaction energies. Most importantly, the O-Mo-O angle significantly impacted by the positions of the anchoring Si atoms nearest neighbors via the Si-O bonds. Thus, the distribution of O-Mo-O angles could be accounted for using cluster models by explicitly accounting for the positions of nearest neighbors to anchoring Si atoms, e.g., by sampling a range of fixed SiF_3 and SiF_2 geometries.

7.0 SIMPLE TRANSFERABLE APPROACH FOR HIGH-YIELD SEPARATION OF STABLE NANOPARTICLES

The content of this chapter is taken from C. S. Ewing, Y. Lai, A. P. Loughner, J. J. McCarthy, and G. Veser "Simple Transferable Approach for High-Yield Separation of Stable Nanoparticles", in preparation.

7.1 INTRODUCTION

Over the past few decades, intense research developing nanomaterials has resulted in synthesis procedures for ever smaller and more precise nanostructures.[172] Very small nanoparticles (NPs) often exhibit unique properties that are fundamentally different from their bulk counterparts, allowing for new and/or improved materials and applications.[173] In order to achieve optimal performance, NPs of low polydispersity with controlled size and shape are increasingly desired.

Traditional synthetic routes, such as wet impregnation, co-precipitation, and deposition/precipitation are often scalable; however, they typically yield a broad size distribution and consequently little control over particle size and shape.[174] The use of ligand capping agents (e.g., phosphine or thiol groups) has been extensively used to achieve precise control of nanoparticle size and obtain extremely low polydispersity.[175] Furthermore, ligand selection has

been shown to allow for careful control of not only size but nanoparticle shape by inhibiting the growth of specific facets.[176-189] Importantly, the use of capping agents can be made convenient and scalable, allowing for regular use in industrial applications.[190]

Despite these advances, scaling up these methods has met with numerous engineering challenges, often related to overall efficiency and cost. For example, very small ligand-protected NPs are typically extremely stable in solution requiring tedious and expensive membrane centrifugation to achieve separation from their synthesis solution. This approach is especially problematic when synthesizing practical sample sizes (e.g., more than 100 mg) due to filter clogging and time constraints.

Furthermore, removal of capping agents requires high temperature calcination, which typically results in sintering of small nanoparticles. It has recently been shown that sintering of ~4 nm Pt_3Fe nanoparticles during high temperature calcinati0n can be avoided by embedding in KCl.[191] However, the procedure is non-transferable as the precipitation of KCl requires the use of metal-choride precursors (e.g., $PtCl_4$) in THF.

In this work, we present a rapid, transferable method for achieving high-yield separation, deposition, and protected annealing of ultra-small nanoparticles via salt recrystallization. We demonstrate that salt recrystallization can be used to efficiently separate and precipitate suspended nanoparticles in solution, circumventing the requirement of membrane centrifugation. We then show how this approach can be tuned to produce well-dispersed supported nanoparticles in a one-pot synthesis procedure, resulting in a significant reduction of time and number of required steps, compared to currently employed methods. Finally, we demonstrate that removal of capping agents can be achieved without nanoparticle sintering via protected annealing, i.e., calcination while embedded in thermally stable salts.

7.2 EXPERIMENTAL

7.2.1 Synthesis of 6 nm silica.

We synthesized 6 nm silica NPs using a two-phase variation of the Stöber method,[192] adapted by Wang *et al.*,[84] and further developed by some of us.[103] Briefly, a catalyst stock solution was prepared by mixing ammonia with deionized (DI) water to a pH of 11.4. 2.6 g of tetraethyl-orthosilicate (TEOS) was diluted in 5 ml ethanol, mixed thoroughly, and added to 34.75 g of catalyst stock solution. The solution was then stirred for 3 hours at 60 °C. Further details of the synthesis procedure can be found in the supporting information.

7.2.2 Synthesis of Silica Support Materials.

Silica supports, approximately 120 nm in diameter, were synthesized using the Stöber method. 18 mL of TEOS, 99 mL of DI water, 36 mL of ammonium hydroxide (30% by volume), and 65 mL of ethanol (190 proof) were mixed at room temperature for 1 hour. The resulting solid was separated from the solution via centrifugation and washed with three times with DI water.

7.2.3 Synthesis of platinum nanoparticles.

Pt NPs (3-5 nm in diameter) were synthesized from a solution containing 1.25 mL of 10 mM chloroplatinic acid aqueous solution and 2.5 mL of 1.39 mM polyvinylpyrrolidone (PVP, ~ 10,000 molecular weight) aqueous solution at 0 °C, which was stirred until well mixed. 1.25 mL of 0.1 M sodium borohydride aqueous solution was then added rapidly. The solution was left to

react for 30 minutes. When using the conventional method of NP separation, the NPs were then recovered and washed with water 3 times using membrane centrifugation (Centricon Ultracel-10K, Amicon Ultra Inc.).

7.2.4 Conventional synthesis of Pt/SiO_2.

Pt NPs were synthesized as described above. After washing, the Pt NPs and 240 mg of (120 nm) silica support were dispersed in 2 ml of DI water. The solution was stirred for 1 hour at room temperature and then dried in vacuum at 100 °C. The resulting Pt/SiO_2 sample was then calcined at 300 °C to remove PVP.

7.2.5 Characterization of nanomaterials.

Transmission electron microscopy (TEM) images were taken on a JEOL JEM2100F with an accelerating voltage of 200 keV. Specific surface area was measured by nitrogen adsorption using a Micromeritics ASAP 2020. The surface area of N_2 was taken to be 1.47 nm^2/mol as determined previously.[85]

7.2.6 Nanoparticle separation via salt recrystallization.

Salt was added to the solution containing NPs until the solution was saturated. Liquid in which the salt is insoluble ("precipitator") was then rapidly added to the solution and agitated to accelerate precipitation. The resulting precipitate and NPs were then recovered via

centrifugation. Finally, the salt was removed via calcination in air. Details of salt recrystallization vary with sample and are discussed in the Results and Discussion.

7.3 RESULTS AND DISCUSSION

7.3.1 Separation of 6 nm silica.

Recently, we adapted a two-phase variation of the Stöber method by Wang *et al.*[84] to achieve monodisperse silica nanoparticles approximately 6 nm in diameter. This one-pot synthesis involves only water, ethanol, ammonia and tetraethyl-orthosilicate (TEOS). While purification is theoretically simple due to the absence of surfactants, dissociation of surface hydroxyls in the aqueous synthesis environment results in strong repulsive electrostatic interparticle forces causing the silica NPs to be extremely stable in solution. As a result, high-speed centrifugation returns no solid material. Furthermore, we found centrifugation to be ineffective even after pH neutralization and traditional "salting out"–the addition of salt to screen electrostatic forces between NPs.

The standard approach for separating stable nanoparticles is the use of membrane filtered centrifugation. This approach, however, can be problematic for syntheses involving more than a few ml of solution and/or a few mg of solid NPs. The synthesis of 6 nm silica results in 43 ml of solution and 680 mg of solid NPs. As a result, membrane centrifugation requires the use of many centrifugation cycles. For our materials, removal of the solution requires four separate centrifugation cycles, which take approximately 45 minutes each because of membrane clogging due to the high volume of solids. After combining the solid materials, each subsequent wash

cycle requires an additional 45 minutes. In order to dilute any residual TEOS or contaminants by 1000 times, we washed the sample three times with 15 ml of water. One synthesis therefore results in a total centrifugation time of 5 hours and 15 minutes. Alternatively, in exchange for consuming three more centrifuge tubes, centrifugation time can be reduced to 3 hours by using four membrane centrifuge tubes simultaneously. The materials are then dried and calcined at 500 °C to remove any residual TEOS.

Table 7.1. Duration of synthesis and separation steps for producing 6 nm silica NPs using conventional and salt methods.

	Centricon	Centricon	Salt Method
Membranes Used	1	4	0
Synthesis (min)	180	180	185
Centrifugation (min)	315	180	20
Total Time (min)	*495*	*360*	*205*

As an alternative approach, we separated the silica NPs from solution using salt recrystallization, achieving the same SiO_2 yield as the conventional approach: 90%. We first added ~5 g of ammonium chloride (NH_4Cl) to saturate the solution. We then rapidly added 35 ml of ethanol while stirring. The solution was then separated by regular centrifugation using two 50 ml centrifuge tubes. The solid materials were then combined and washed three times. Due to the

insolubility of NH_4Cl in ethanol, complete separation was achieved using centrifugation at 4000 rpm in under 4 minutes. One synthesis with three wash cycles can thus be achieved using only 20 minutes of total centrifugation time. Table 1 shows the duration of synthesis and separation steps using the “centricon” (using either 1 or 4 membrane centrifuge tubes) and salt methods for NP separation. The salt method requires 5 additional minutes during synthesis, in order to add, mix, and precipitate the salt; however, the reduction in separation time is far more significant. Use of the salt method results in a 43 - 59% reduction in total preparation time compared to the conventional approach.

Following the salt separation procedure, the resulting silica NPs are encapsulated in NH_4Cl salt. Because NH_4Cl dissociates into gaseous NH_3 and HCl at 338 °C, after calcination at 500 °C (required for removing residual TEOS) the pure silica NPs are obtained. This approach also does not require the use of membrane centrifuge tubes, which are costly and have finite lifetimes. Although the salt recrystallization approach requires the addition of a significant amount of salt, NH_4Cl is easily condensed at room temperature and can thus be recycled.

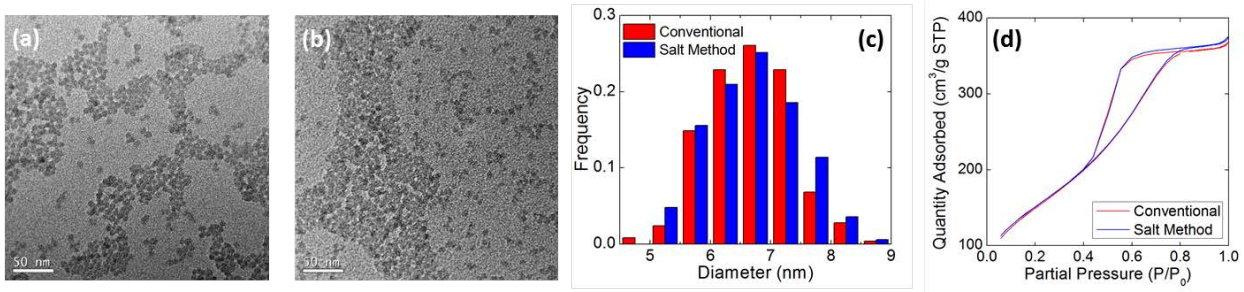

Figure 7.1. TEM images of silica NPs separated using (a) membrane centrifugation and (b) our salt recrystallization method. (c) NP size distributions taken from TEM images. NP diameters for conventional (N=249) and salt method (N=167) were 6.18 ± 0.69 and 6.18 ± 0.74 nm, respectively. (d) N2 isotherms of silica nanoparticles produced using both separation methods. BET specific surface areas of NPs produced using the conventional and salt separated methods were 488 and 484 m2g-1, respectively.

To demonstrate the non-destructive nature of the salt recrystallization approach, i.e. that the particle size distribution is unchanged from the conventional approach when using the proposed approach; we characterized the obtained NPs using TEM and BET N_2 adsorption. Figure 7.1a and 7.1b show TEM images of silica NPs separated using conventional and salt methods, respectively. Size distributions and N_2 adsorption isotherms, shown in Figures 7.1c and 1d, respectively, confirm that the salt recrystallization method does not alter the physical properties of the NPs. Furthermore energy dispersive X-ray spectroscopy confirmed that there no Cl remained after calcination.

7.3.2 Separation of 4 nm Pt.

We have demonstrated the use of salt recrystallization for isolating NPs that are stabilized by ionic interactions (i.e., silica). However, metal NPs in particular are more commonly stabilized by non-ionic capping agents, such as polymers.[175] Furthermore, the 6 nm silica synthesis described above has few reactants, and hence a relatively simple synthesis solution. To demonstrate the transferability of NP separation via salt recrystallization, we applied this approach to the separation of 4 nm Pt NPs stabilized by polyvinylpyrrolidone (PVP).

A small quantity of Pt NPs (~2.4 mg) was synthesized in a 15 ml solution that is relatively complex, containing: Cl^-, H^+, Na^+, $BH4^-$, platinum NPs, and PVP. After NP growth, the synthesis bath was saturated with NH_4Cl (2 g). Ethanol (30 ml) was rapidly added and the solution was agitated, resulting in precipitation of the salt. Pure Pt NPs were recovered at a yield of 83% after NH_4Cl was removed by calcination in air at 350 ℃. The yield is significantly less than the 90% yield obtained using membrane centrifugation. However, PVP is burned off during calcination at 350 ℃ (required for removing NH_4Cl) resulting in significant sintering of Pt NPs, so no further optimization was performed. Thus, while this result demonstrates the transferability of the method to NPs composed of other materials, it also reveals the need for tuning the salt dissociation temperature based on NP composition.

7.3.3 Synthesis of Pt/SiO_2 Catalyst.

Using a salt with a low dissociation temperature, NP separation via salt recrystallization method can be used to synthesize 4 nm Pt/SiO_2 in significantly less time than the conventional approach. To minimize sintering the NPs should be in direct contact with the support and isolated from

each other at the time of calcination. Ammonium bicarbonate (NH_5CO_3) was chosen for the salt because it dissociates at a temperature of about 50 °C, allowing for the removal of salt while leaving PVP intact. The Pt NPs–still protected by PVP–can then be dispersed onto the support and subsequently calcined to remove PVP. Finally, to reduce the number of steps required, addition of support material was integrated into the NP separation procedure as follows.

After Pt NP growth, enough salt was added to saturate the solution (~2 g). Isopropanol (30 ml) containing well dispersed 120 nm silica NPs (240 mg) was then rapidly added to the synthesis bath and agitated. The solution was then centrifuged to give a dark solid containing NH_5CO_3, silica, and platinum, which was then dried in a vacuum oven at 60 °C to dissociate the salt. The Pt/SiO_2 mixture was then briefly mechanically mixed using mortar and pestle to disperse the Pt NPs on the silica surface. Finally, the sample was calcined at 300 °C to remove PVP. Figure 7.2a shows the Pt NPs as-synthesized, prior to any calcination. From Figures 7.2b and c we see that despite some particle growth during calcination, Pt/SiO_2 produced using both conventional and salt recrystallization methods have the same average NP size and size distribution. Furthermore, energy dispersive X-ray spectroscopy confirms similar weight loadings of 0.68 and 0.64 wt% Pt achieved using conventional and salt methods, respectively.

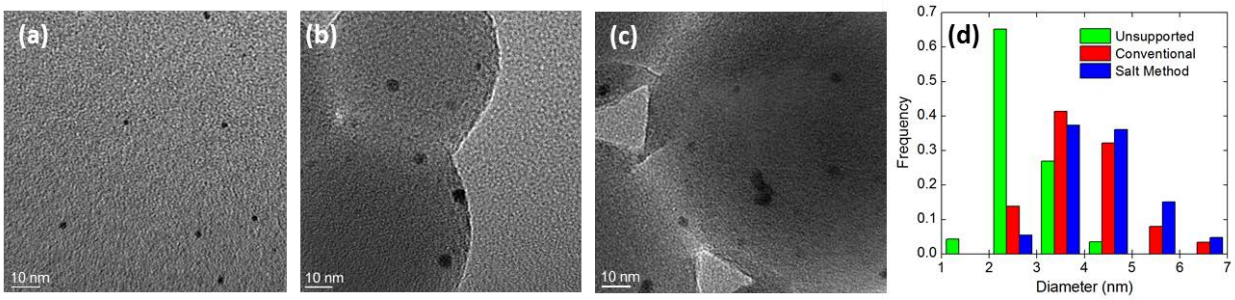

Figure 7.2. Representative TEM images of (a) as-synthesized Pt NPs deposited on TEM grid and Pt/SiO2 synthesized using (b) the conventional method and (c) the salt recrystallization method (d) The corresponding size distributions. NP diameters were (a) 2.8 ± 0.5, (b) 4.1 ± 1.0, and (c) 4.3 ± 1.0 nm.

Flow charts of the conventional and salt recrystallization procedures, along with the total time per step are shown in Figure 7.3. The conventional approach takes almost 4-times as long as the salt recrystallization method due to three major differences. First, membrane centrifugation is replaced with regular centrifugation for both initial separation and washing with the salt method (which not only cuts time, but also cost of this separation step). Second, NPs are deposited onto supports using mechanical mixing rather than wet deposition. Finally, while the conventional approach requires removal of water after wet deposition, the final wet step in the salt method is only washing, and hence acetone can be used, which dramatically reduces drying time.

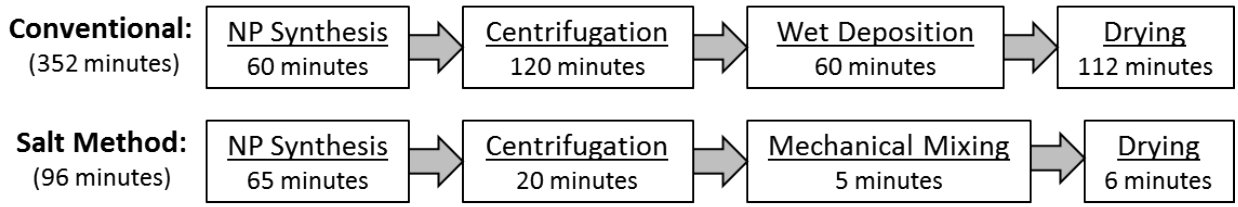

Figure 7.3. Flow chart depiction of the conventional and salt recrystallization methods for synthesizing Pt/SiO2. The charts include approximate times to complete each step. Drying times were calculated for 2 ml of solution at 100 °C assuming a 1 cm2 exposed surface area.

7.3.4 Protected Annealing of 2.5 nm Pt.

We have shown that salts with low dissociation temperatures can be used to efficiently separate NPs from solution, and even synthesize supported NPs. Thermally stable salts, however, can stabilize NPs that are sufficiently separated within the salt matrix. Chen *et al.* demonstrated that 4 nm Pt_3Fe NPs grown within a KCl matrix are protected from sintering when the ratio of salt to NP is sufficiently large.[191] Using our salt recrystallization method, we embedded 4 nm Pt in KCl as follows. After growth, the 15 ml solution of Pt NPs was diluted with 15 ml of water in order to allow for a sufficiently large ratio of salt to NP ratio. About 9 g of KCl was then added to the solution and rapidly precipitated by adding 60 ml of ethanol. The sample was then dried and calcined at 500 ℃ for two hours.

Figures 7.4a and b show Pt NPs embedded in KCl before and after calcination, respectively. As-synthesized Pt NPs (Figure 7.2a) were less than 3 nm in diameter. However,

after calcination in air at only 300 ℃, the Pt NPs on silica supports grow to over 4 nm. Figure 7.4a shows that the NPs did not agglomerate during KCl precipitation, which is expected because they were still stabilized by PVP. Figure 7.4b shows that Pt NPs embedded in KCl were completely protected from sintering during calcination for two hours at 500 ℃.

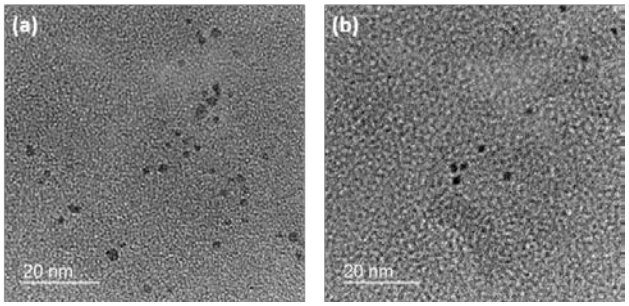

Figure 7.4. TEM images of 2.5 nm Pt embedded in KCl (a) before and (b) after calcination at 500 °C. NP diameters were (a) 2.2 ± 0.4 and (b) 2.4 ± 0.7 nm.

Chen *et al.* further demonstrated that the embedded NPs can then be transferred to a support material by dissolving the salt in a solution of water and ethylene glycol, which temporarily stabilizes the NPs.[191] It is thus likely that the salt recrystallization method, using a thermally stable salt (e.g., KCl) can be used to remove surfactant (through pores in the salt matrix) while protecting NPs from sintering. Additionally, high temperature treatment is often

used to represent long time scales, and hence we expect that embedding in salt may be an excellent method for maintaining NP stability for indefinite storage times.

7.4 CONCLUSIONS

Despite extraordinary developments in NP synthesis, the potential industrial (large-scale) use of very small and precisely controlled NPs is hindered by difficulties in scaling up their synthesis. Most effort has been focused on the development of well-defined NPs, while the problem of scalability and cost of nanomaterials synthesis has been largely overlooked.[176-189] Most small, mono-disperse NPs are extremely stable in solution and require the use of costly and time consuming membrane centrifugation to separate them from the synthesis solution. We present a novel, scalable, and very straightforward approach for separation of NPs from solution via salt recrystallization that circumvents the need for membrane centrifugation. This approach is applicable to both metal and oxide NPs stabilized by ionic and non-ionic interactions. Furthermore, we demonstrate that this approach can be tailored, by choice of salt, for separation of bare NPs, synthesis of supported NPs, or even for protected annealing. Additionally, this method significantly reduces the number of steps and total time required for both separation of NPs from solution and for synthesis of supported NPs. Remarkably, the same size distributions of Pt/SiO_2 produced via membrane centrifugation and wet deposition are achieved using salt recrystallization and mechanical mixing alone, making this approach far more favorable for scaling up.

8.0 FUTURE WORK

8.1 EFFECTS OF NANOPARTICLE SUPPORT EFFECTS

In chapters 3, 4, and 5, we explained how adhesion energy can be used to predict the stability of supported nanoparticles (NPs). In order to understand the effects of NP-support interactions on reactivity, however, correlations relating the reaction intermediate adsorption energetics and catalyst-support effects much first be first be ascertained. We have calculated adsorption energies for CO and O on amorphous silica supported Pt_{13}, Pt_{55}, and Pt_{147}. CO and O adsorption energies can be used to predict reaction barriers for CO oxidation.[12]

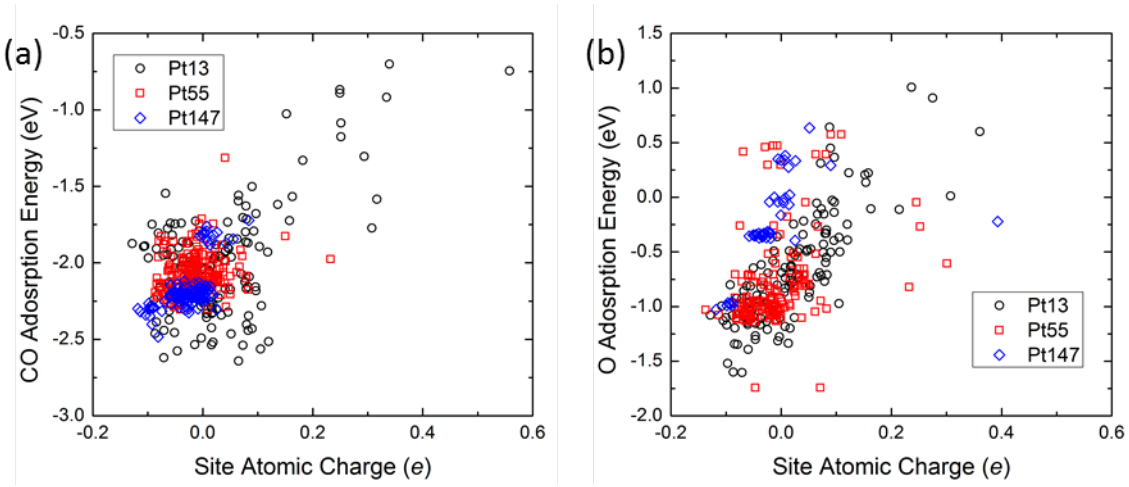

Figure 8.1. CO and O adsorption energies on top sites of amorphous silica supported Pt_{13}, Pt_{55}, and Pt_{147}.

We found that both CO and O adsorption strengths did not correlate with the coordination number or d-band center of the metal atom to which they are adsorbed. However, some trends emerge when plotting adsorption energies of CO and O as a function of the atomic charge of the site to which they are adsorbed, shown in Figure 8.1. Although there is significant scatter for all NP sizes, O adsorption energy is generally weaker with increasing atomic charge of the adsorption site. Furthermore, both CO and O bind weakly to sites with an atomic charge of ~0.2 *e* or higher, which are Pt atoms bonded to an O atom on the silica surface. Importantly, weaker binding of both CO and O has been shown to correlate with smaller reaction barriers for CO oxidation, for crystalline Pt surfaces.[12] In future work, the validity of this statement for disordered Pt NPs (those on amorphous surfaces) can be checked by calculating reaction barriers using nudged elastic band calculations.

8.2 PREDICTING NANOPARTICLE-SUPPORT INTERACTIONS

After examining metal nanoparticle (MNP)-support interactions with an electronic structure level of theory, we have developed an approach for predicting MNP-support effects for a wide range of NP sizes and geometries on amorphous silica. The next logical step is to apply this methodology towards screening various MNPs in order to map their charge and adhesion properties. Figures 5.3 and 5.4 compare MNP charge and adhesion energies for a handful of small Pt NP geometries. However, in order to apply this methodology to MNPs larger than ~3 nm, some further approximations must be made. Surface energies of the MNP could be calculated using periodic density functional theory. The number of metal-oxygen bonds can be approximated based on the hydroxyl density of the surface. Finally, the total system energy would be calculated using a Wulff construction, which can be easily implemented without costly calculations.

APPENDIX A

SUPPORTING INFORMATION

A.1 ACCURATE AMORPHOUS SILICA SURFACE MODELS FROM FIRST PRINCIPLES THERMODYNAMICS OF SURFACE DEHYDROXYLATION

A.1.1 Silanol number calculation procedure.

The silanol number as a function of temperature plotted in Figure 2.4 is computed by the following procedures:

1. The initial silanol number is computed for each surface by counting the number of silanol groups and dividing by the geometric surface area of each sample. The initial silanol number is determined by the structure of the cleaved surface coupled with saturation of all under-coordinated O atoms with H atoms, as described in the paper.
2. The lowest dehydroxylation energy computed for the surface is used in eq 1.2 and the temperature is adjusted so that $\Delta G_{rxn} = 0$.
3. The silanol number is recomputed for the new surface by reducing the number of silanol groups by two and dividing by the same surface area.

4. Steps 2 and 3 are repeated using the lowest energy for the next step for that surface until no more silanol pairs can condense from the modified surface.

Table A1.1. Comparison of bulk system properties computed from DFT in this work to experiments and other modeling results.

	This Work	Other DFT	Experiment
ρ (g/cm^3)	2.15	2.20[193]	2.20[194]
Si-O dist (Å)	1.66	1.65[193]	1.61,[194] 1.62[195]
Si-O-Si angle (°)	141.9	134[193]	144,[195] 153[196]
O-Si-O angle (°)	109.4	---	109.5,[195] 109.4[196]

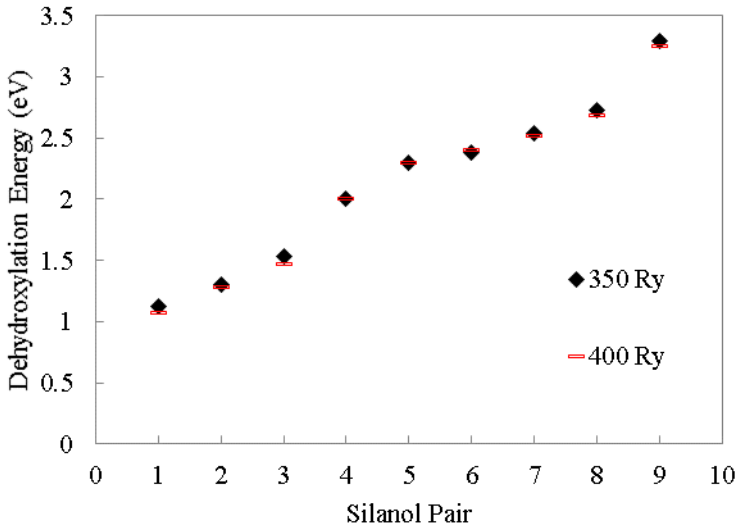

Figure A1.1. Calculated dehdroxylation energies for each silanol pair dehydroxylated on a fully hydroxylated surface using either 350 or 400 Ry planewave energy cut-off. Change in planewave energy cut-off resulted in negligible changes to dehydroxylation energies.

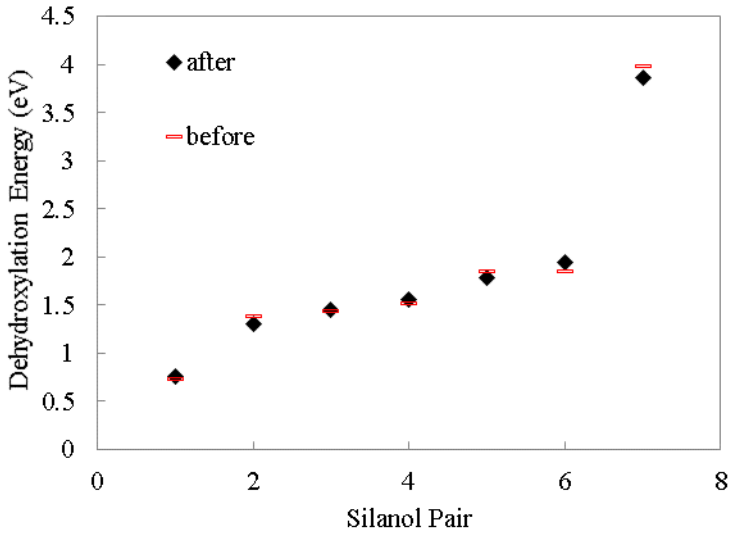

Figure A1.2. Calculated dehydroxylation energies for a fully hydroxylated surface before and after condensing a silanol pair from the bottom surface. Structural changes to the bottom surface resulted in negligible changes to the dehydroxylation energies of silanols on the top surface, indicating that the slab is sufficiently thick that chemical changes to the bottom surface do not affect the top surface, where dehydroxylation is studied. The disordered structure does not allow for simple addition or removal of extra layers, so generation of a whole new surface structure is required, and hence prohibits the direct comparison of dehydroxylation with different surface thicknesses. As the system size is already fairly large (almost 300 atoms), larger systems would have significantly increased the time of the current study. We therefore relied on the above test as well as the results of Goumans *et al.* for quartz surfaces.[79]

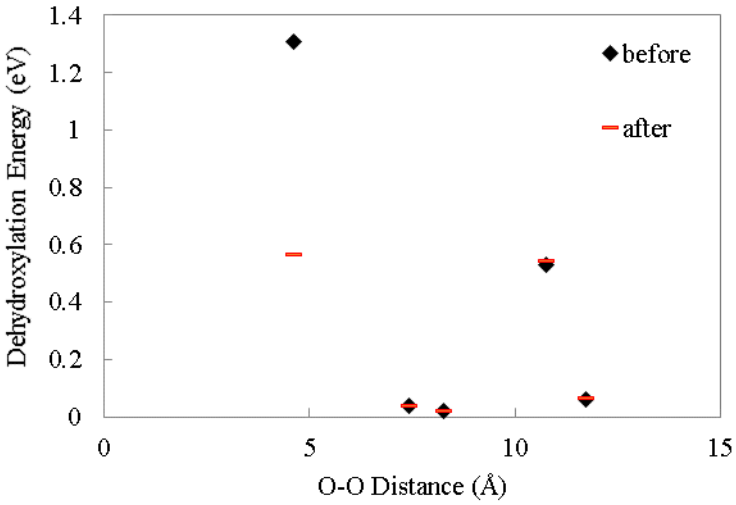

Figure A1.3. Dehydroxylation energies of a silanol pair before and after condensation of a neighboring silanol pair as a function of the distance between the two condensing silanol pairs. Condensation of a neighboring silanol pair with separation greater than 7 Å resulted in negligible changes to dehydroxylation energy, which indicates that the lateral dimensions of our supercell are sufficiently large.

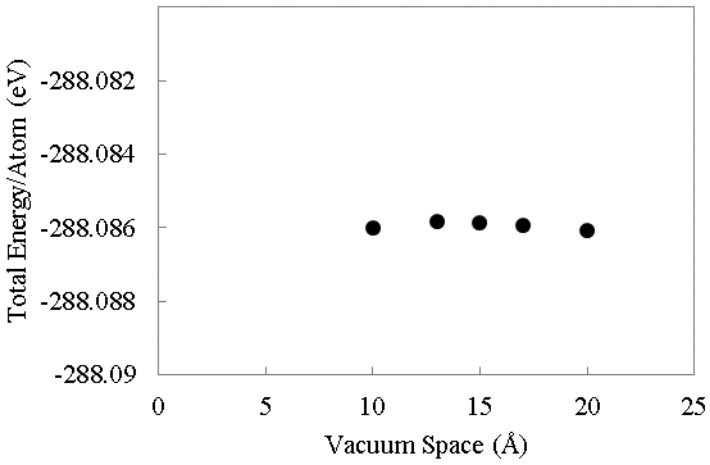

Figure A1.4. Total energy per atom as a function of vacuum spacing between silica slabs in the z-direction. Change in vacuum spacing resulted in negligible change to the system energy.

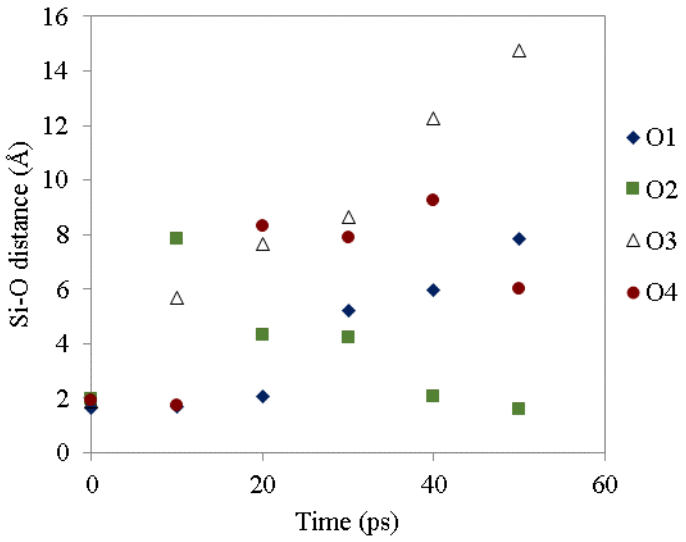

Figure A1.5. Si-O distances for four O atoms initially bonded to a reference Si atom as a function of simulation time. Note that the average Si-O bond length is 1.66 Å. This figure indicates that at each geometry snapshot for slab generation, the reference Si atom had different neighboring oxygen atoms, and hence will relax to an independent structure. We examined multiple other reference Si atoms and the results were consistent.

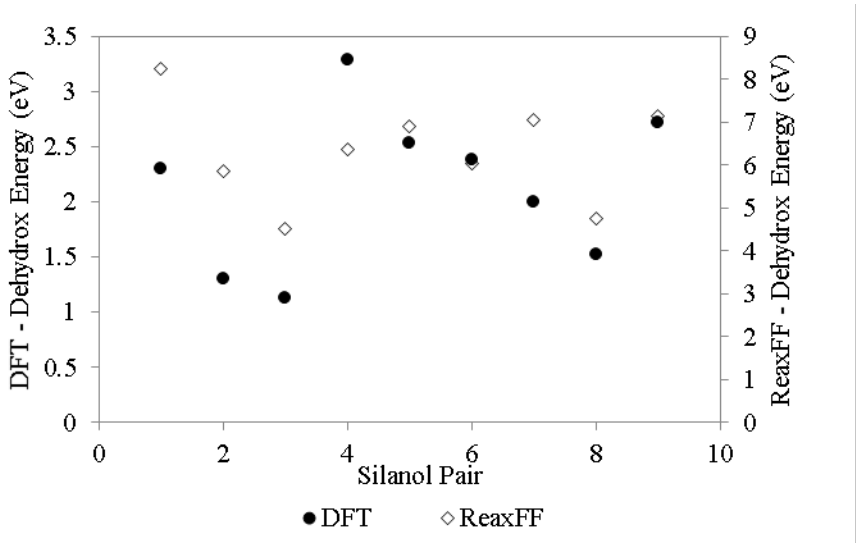

Figure A1.6. Dehydroxylation energies for all silanol pairs on one surface calculated using ReaxFF and DFT. The lack of agreement between DFT and ReaxFF indicates that ReaxFF is inadequate for computing dehydroxylation energies.

A.1.2 Details of synthesis procedure.

TEOS, ethanol (200 proof) and ammonia (%) were obtained from Sigma-Aldrich and used as received. Catalyst stock solution was prepared by adding ammonia to DI water until a pH of 11.4 was reached. 34.75 g of catalyst stock solution was added to a 100 ml round bottom flask, stirred at 550 rpm, and heated to 60 °C. 2.8 g of tetraethyl-orthosilicate (TEOS) was added to 5 ml of ethanol and shaken vigorously for about 30 seconds. After about five minutes the ethanol/TEOS mixture was poured into the round bottom flask. After three hours the solution was removed,

separated using a filtered centrifuge, and dried at 50 °C. The dry particles were then calcined at 350 °C and soaked in water for 24 hours, at room temperature.

A.1.3 Details of Thermogravimetric Analysis.

Sample weight as a function of temperature was measured using a thermogravimetric analyzer (Perkin-Elmer TGA-7). Approximately 6 mg of sample was heated inside the TGA cradle in a stream of air (Grade 0.1; 20 sccm). The sample was heated to 200 °C at a ramp rate of 10 °C/min and then held isothermal for approximately one hour, in order to remove all physisorbed water. The sample was then heated to 900 °C at a rate of 5 °C/min.

A.1.4 Detailed Derivation of the Statistical Thermodynamics Model (Eq. 1.2).

The Gibbs free energy associated with a dehydroxylation step (i.e., the condensation of one water molecule) is

$$\Delta G_{rxn} = G_{s-H_2O} + G_{H_2O} - G_s. \quad \text{(A1.1)}$$

The subscripts *s* and *s*-H_2O denote the surface before and after removal of a water molecule and H_2O is a single ideal gas water molecule. The Gibbs free energy each system, *i*, can be written as

$$G_i = H_i - TS_i = E_i + U_i - TS_i, \quad \text{(A1.2)}$$

where H_i, E_i, and U_i are the enthalpy, DFT electronic energy, and the statistical mechanical internal energy for system *i*, respectively. We have assumed that the pressure-volume terms are negligible in eq 2. We write the entropy term using the statistical mechanics identity,

$$TS_i = kT\ln Q_i + U_i, \tag{A1.3}$$

where Q_i is the partition function for system *i*. Substituting eq 3 into 2, we obtain

$$G_i = E_i - kT\ln Q_i. \tag{A1.4}$$

Substituting eq 4 into 1 gives

$$\Delta G_{rxn} = \Delta E_{DFT} + kT\ln\left(\frac{Q_{s-H_2O}Q_{H_2O}}{Q_s}\right). \tag{A1.5}$$

In eq 5 $\Delta E_{\mathrm{DFT}} = E_{s-H_2O} + E_{H_2O} - E_s$. The partition functions for the solid phases are due solely to vibrational (phonon) modes in the solid, but the partition function of water contains contributions from the translational and rotational modes in addition to vibrations, so that $Q_{H_2O} = q_t q_r q_v$, where the molecular partition functions have been used since we have assumed the loss of a single water molecule from the surface. We now make the assumption that the difference in the phonon modes of the surface is balanced by the vibrational modes of the free water molecule, so that

$\frac{Q_{s-H_2O}q_v}{Q_s} \approx 1$. The translational partition function for water, assuming ideal gas behavior, is given by $q_t = \frac{kT}{P_{H_2O}\Lambda^3}$, where P_{H_2O} is the partial pressure of water in equilibrium with the silica surface and Λ^3 is the thermal de Broglie wavelength of water. The final expression for the free energy change of dehydroxylation is therefore given by

$$\Delta G_{rxn} = \Delta E_{DFT} - kT\ln\left(\frac{kTq_v}{P_{H_2O}\Lambda^3}\right). \qquad \text{(A1.6)}$$

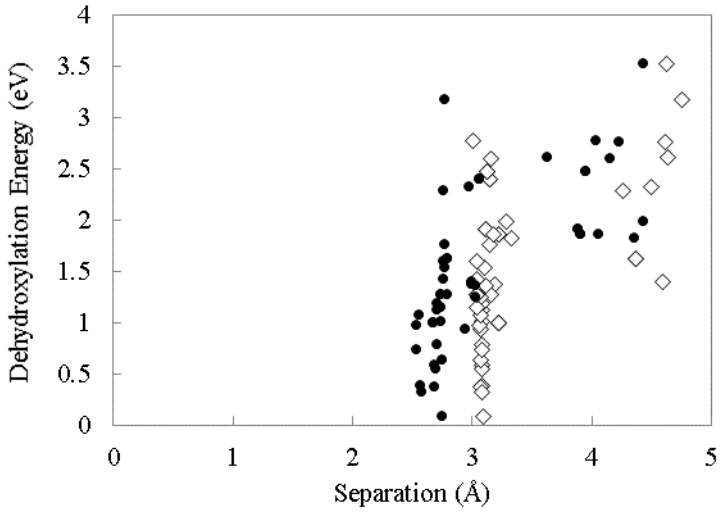

Figure A1.7. Dehydroxylation energy vs. separation between silanols that are condensed (filled circles: Si-Si distance; open diamonds: O-O distance).

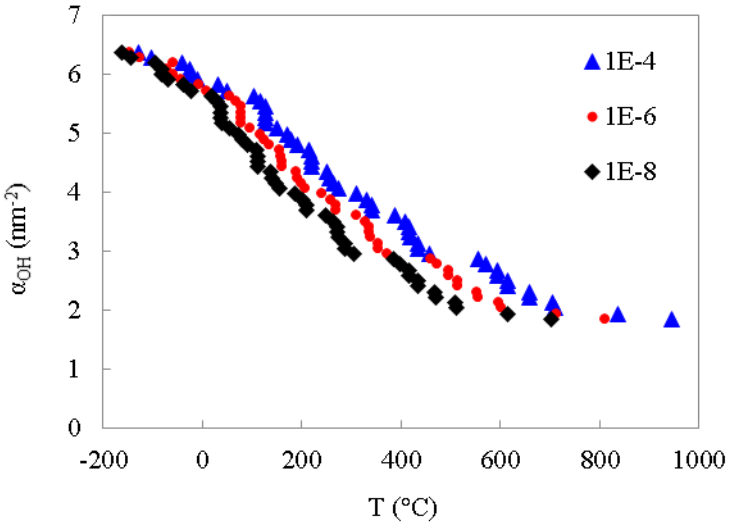

Figure A1.8. Silanol number vs. temperature for different values of P_{H_2O} Triangles, $P_{H_2O} = 10^{-4}$ bar. Circles, $P_{H_2O} = 10^{-6}$ bar. Diamonds, $P_{H_2O} = 10^{-8}$ bar.

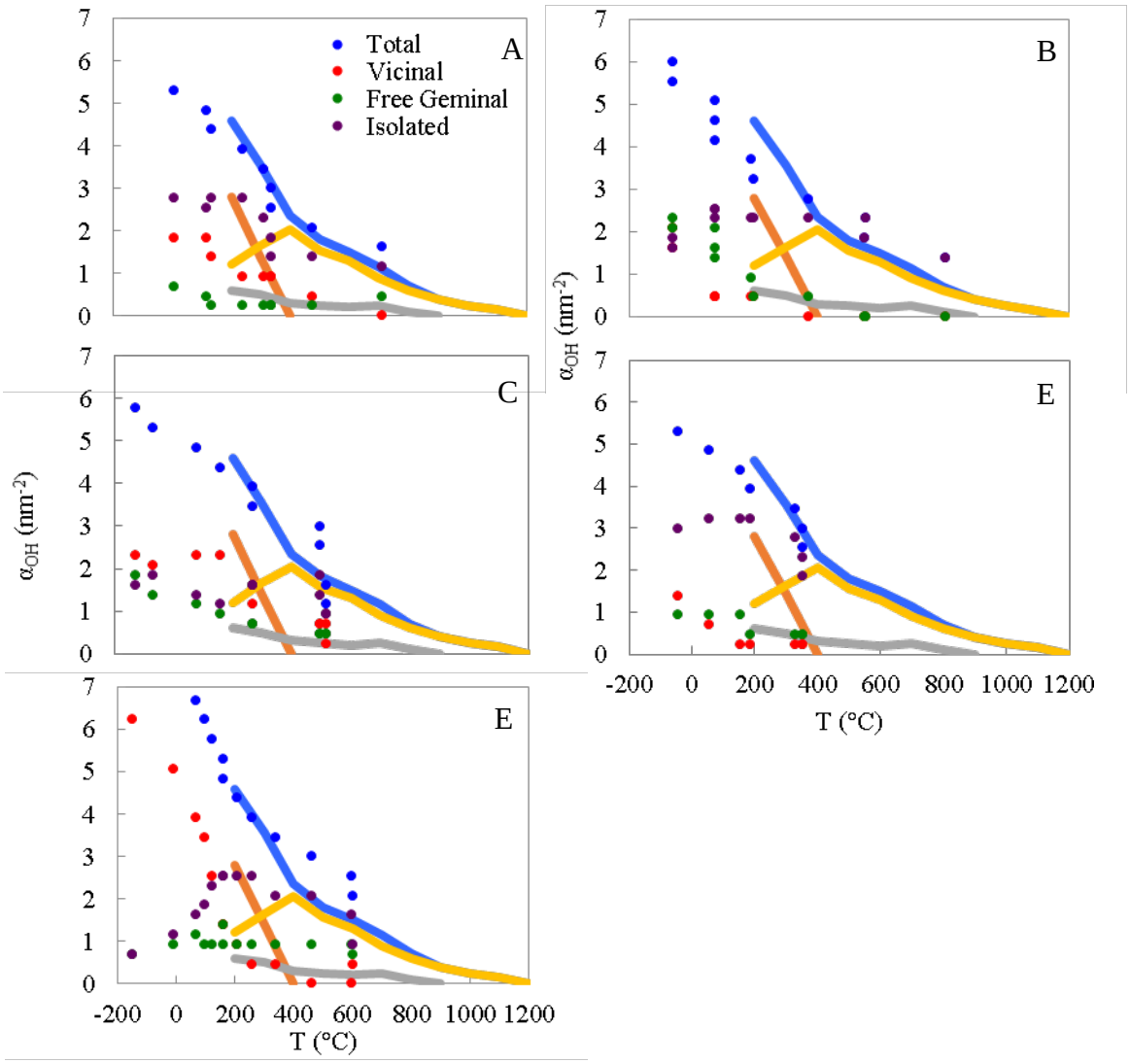

Figure A1.9. Silanol distribution for each of the five surfaces studied: A, B, C, D, and E. Solid lines are experimentally reported silanol distributions from Zhuravlev.[52]

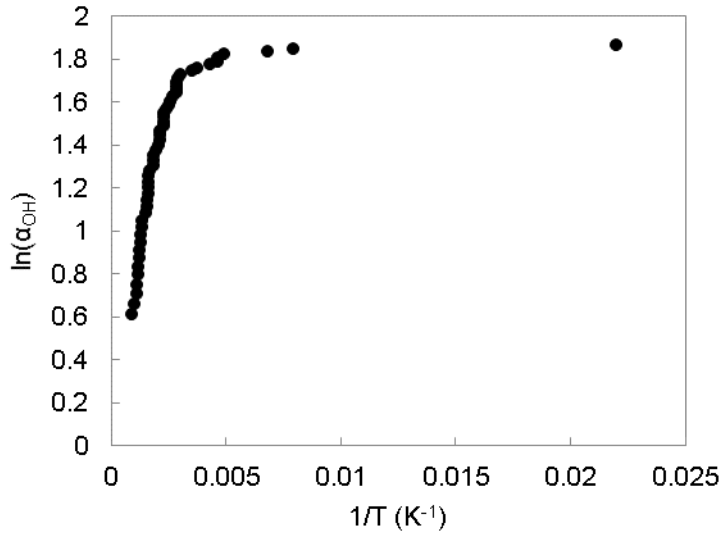

Figure A1.10. Van't Hoff plot for silanol numbers of all surfaces combined. Here we considered silanol number as analogous to the equilibrium constant in the Van't Hoff equation. The non-linearity of this plot indicates a strong temperature dependence of the energy of dehydroxylation.

A.1.5 Procedure for calculating silanol numbers from TGA curves.

The silanol number (α_{OH}) is defined as the number of silanols per square nanometer. This can be calculated as follows:

$$\alpha_{OH} = \frac{2(M_{dry} - M(T))}{SA \times MW_{H_2O}} \quad \text{(A1.7)}$$

where M_{dry} sample mass after drying at 200 °C for one hour, $M(T)$ is the sample mass at temperature T, SA is the specific surface area and MW_{H_2O} denotes the molecular weight of water.

We assumed no silanols were present at temperatures greater than 900 °C. Previous experimental studies have indicated that the silanol number is less than one at temperatures greater than 900 °C.[52] Our assumption, therefore, has negligible effect on the order of magnitude of the silanol number and does not affect the qualitative features of the silanol number curve.

A.2 STRUCTURAL AND ELECTRONIC PROPERTIES OF PT_{13} NANOCLUSTERS ON AMORPHOUS SILICA SUPPORTS

A.2.1 Simulating NP Adsorption.

After dropping the Pt cluster onto the silica surface, we checked for hydroxyl groups within range to bond to a Pt atom. Hydroxyl groups were determined to be within range to bond if the distance between Pt and O or Pt and H was less than 110% of the sum of the two atoms respective van der Waals radii.

A.2.2 Computational Details.

For all DFT calculations we used the CP2K code, which employs a Quickstep[78] implementation of the DFT method using plane waves/pseudopotentials and localized Gaussian basis sets. Calculations used the revised PBE functional (revPBE)[104] and GTH pseudopotentials[81,82] in

conjunction with short range double-ζ basis sets with polarization functions (SR-DZVP).[105] We used a 350 Rydberg energy cutoff for the plane wave basis set. All surface slabs were relaxed using CP2K treated as periodic in all directions with at least 20 Å of vacuum between slabs to eliminate interactions between the periodic images of the surface slabs. To reduce computational cost, all relaxation calculations were spin-restricted. Electronic analysis calculations (frontier orbital analysis) were performed with spin-polarized DFT. Validation of the planewave energy cutoff, basis sets, vacuum spacing and spin-restricted relaxation are shown below. Atomic partial charges were calculated using the Bader Charge Analysis code (version 0.28a) from the Henkelman Group.[135,136] All other post-processing analyses were calculated using in-house Python codes.

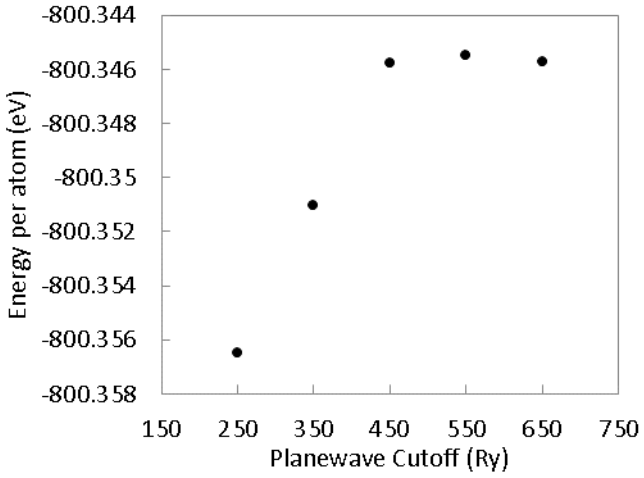

Figure A2.1. System energy per atom vs plane wave energy cutoff. Total system energy converges at 450 Ry plane wave energy cut-off; however, in order to allow for reasonable relaxation times we compromised with a 350 Ry plane wave cutoff. This is close to completely converged plane wave energy cutoff and resulted in a per atom energy error of only ~0.005 eV.

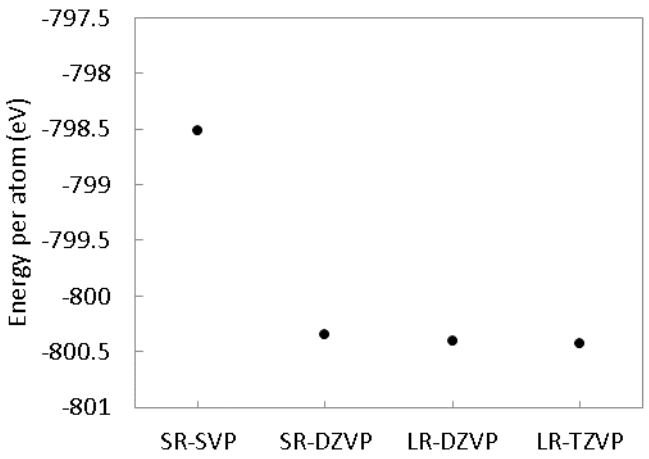

Figure A2.2. System energy per atom for different basis sets. System energy is clearly converged for the LR-DZVP basis set. Plane wave cut-off was 350 Ry for all systems. SR and LR denote Short Range and Long Range, respectively.

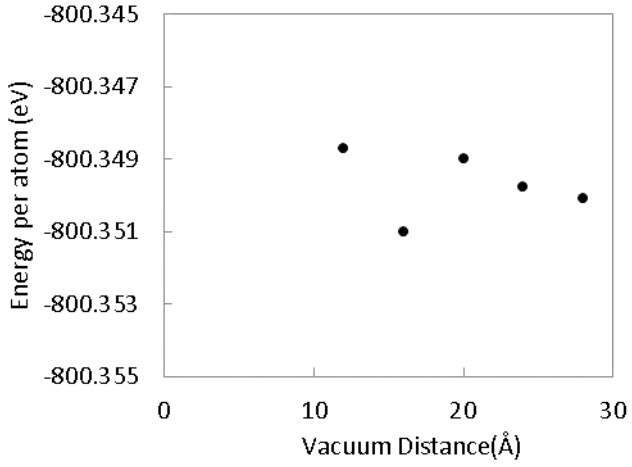

Figure A2.3. System energy per atom vs vacuum distance. The system energy per atom varies by only ~0.002 eV, and is thus not sensitive to vacuum distance between 10 and 30 Å. We therefore conclude that the vacuum distance is sufficiently converged at 20 Å.

A.2.3 Spin-restricted validation.

We relaxed all systems in this study using spin-restricted DFT. To test the validity of this approximation, we first calculated single-point energies of some of the final structures using spin-polarized DFT and found that the system was not spin polarized, having energies that are essentially identical. We also allowed final structures to further relax using spin-polarized DFT and again found no spin in these systems.

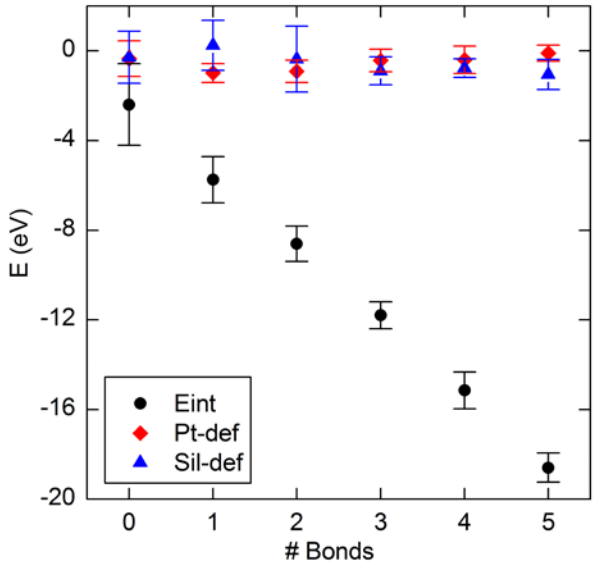

Figure A2.4: Deformation energies for Pt and Silica and Pt-silica interaction energies vs number of Pt-silica bonds. For systems with Pt-silica bonds H atoms were removed from the silica surface during the Pt adsorption procedure. For the silica surface, we therefore calculated the reference energy as the single point energy of the surface at its initial configuration with the H atoms removed. It is clear that both Pt and Silica deformation energies are close to zero and negligible when compared to the interaction energy in almost all cases.

Table A2.1: Percent contribution of deformation energy to the adsorption energy $E_{def} + E_{int}$, *defined as* $\frac{E_{def}}{(E_{int}+E_{def})}$.

# Bonds	% Contribution
0	21.2
1	11.6
2	13.0
3	10.1
4	7.2
5	5.9

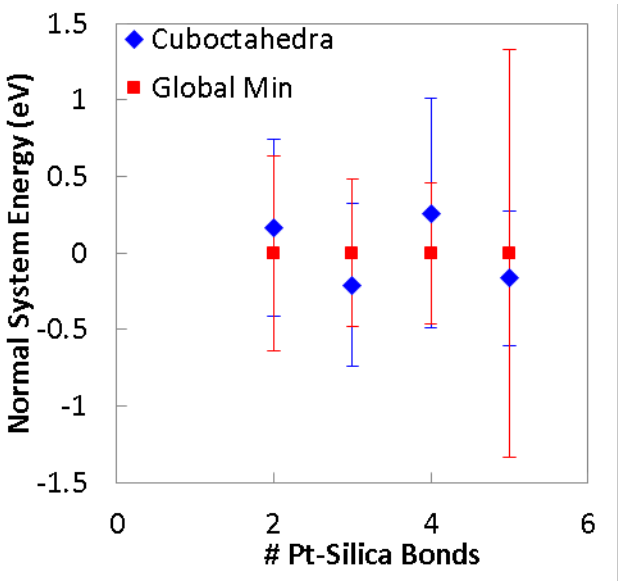

Figure A2.5. Normalized system energy ($E - E_{GM}$) as a function of the number of Pt-silica bonds. E is the average energy all systems with a given number of Pt-silica bonds and a given initial structure. E_{GM} is the average energy of all systems with a given number of Pt-silica bonds and the global minimum initial structure.

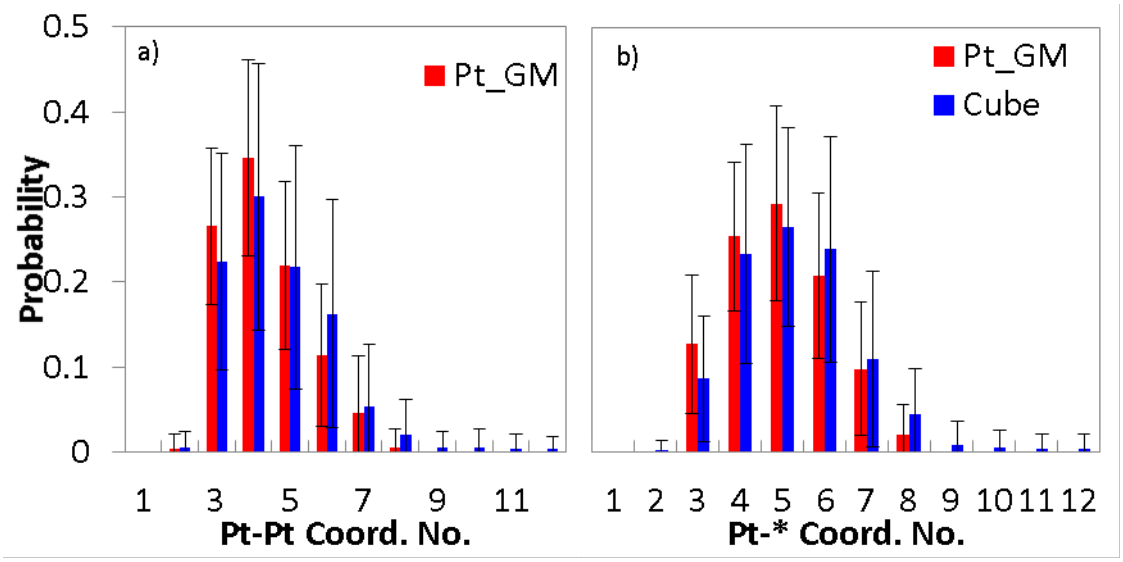

Figure A2.6. Distribution of atomic coordination numbers for theoretical global minimum (red) and cuboctahedral (blue) Pt_{13} clusters. (* denotes any atom type).

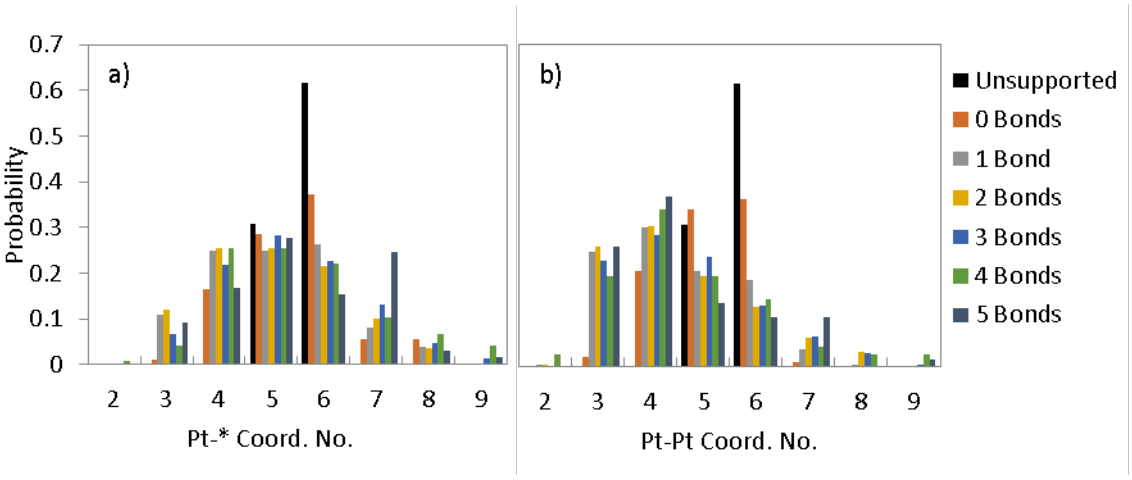

Figure A2.7. Distribution of Pt-* (a) and Pt-Pt (b) atomic coordination numbers for Pt_{13} clusters as a function of number of Pt-Silica bonds.

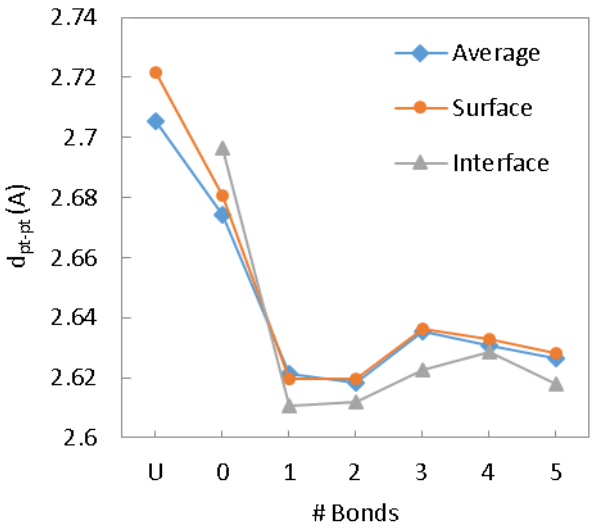

Figure A2.8. Mean Pt-Pt bond length as a function of number of bonds between Pt and silica. Surface and Interface values were calculated for atoms at the Pt-vacuum interface and the Pt-silica interface, respectively. U indicates the unsupported NP.

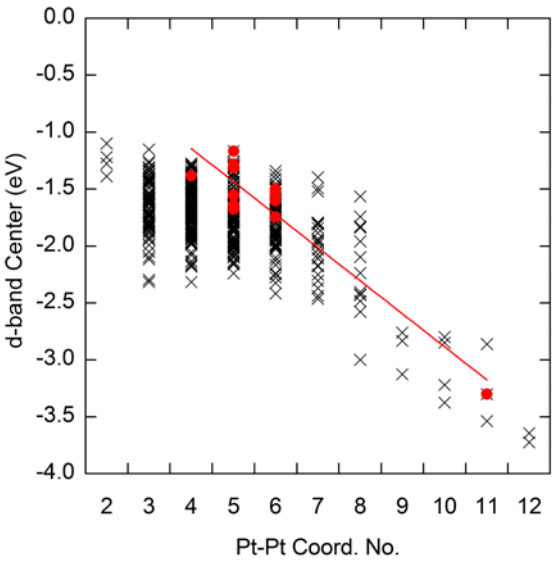

Figure A2.9. d-band center as a function of coordination number for all Pt atoms in this study (shown as black x symbols) and the unsupported cuboctahedral Pt_{13} cluster (shown as red dots). The d-band center for the isolated cluster roughly correlates with the Pt-Pt coordination number, as illustrated by a linear fir with $R^2 = 0.87$. Values were calculated considering eigenvalues between -8 and 6 eV for the d-states projected onto the individual Pt atom.

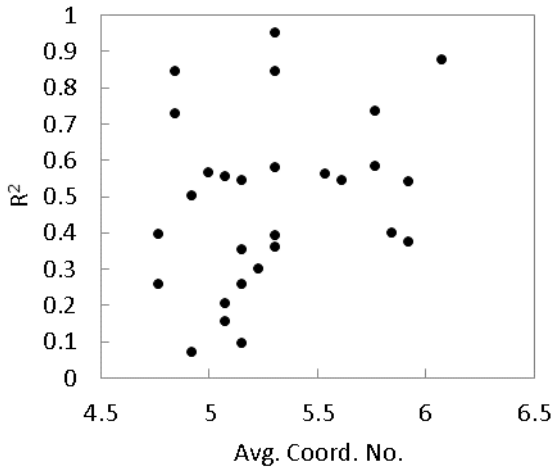

Figure A2.10. We plotted d-band center vs Pt-Pt coordination number for each Pt/silica system in this study. We then fitted a line to each data set and calculated the resulting coefficient of determination (R^2). This figure shows the values of R^2 for each Pt/silica system in this study as a function of the average Pt-Pt coordination number of the cluster. This clearly demonstrates that there is no universal correlation between d-band center and CN for silica-supported Pt_{13} clusters.

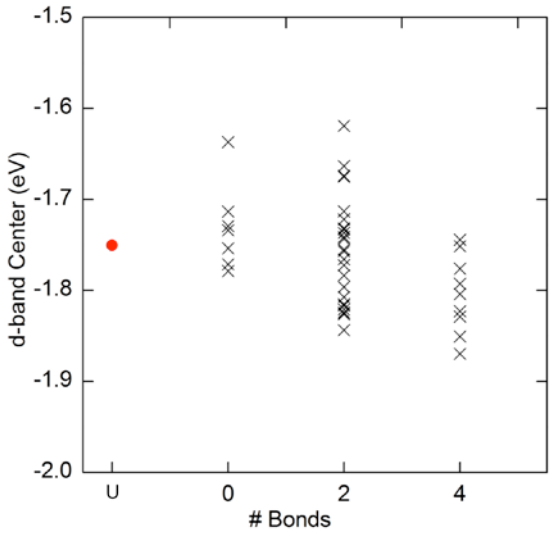

Figure A2.11. The d-band center calculated from d-DOS for entire Pt clusters vs number of Pt-silica bonds. Red circle indicates the d-band center for the unsupported cuboctahedral Pt_{13} cluster.

Table A2.2: HOMO of representative supported and unsupported Pt_{13} clusters. (iso-value: 0.05)

	Cuboctahedral Pt_{13}	Physisorbed; restructured	4 Pt-O Bonds; restructured
Unsupported	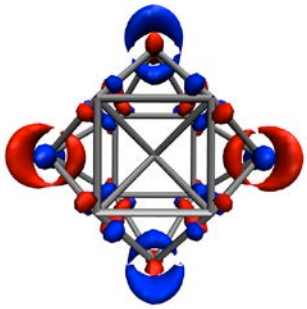	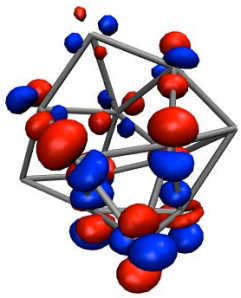	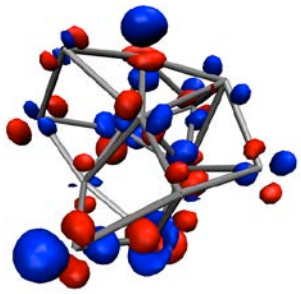
Supported	N/A	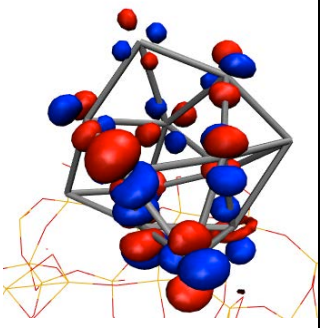	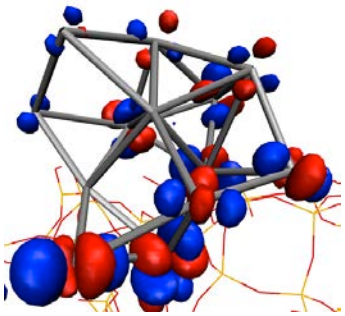
Difference*	N/A	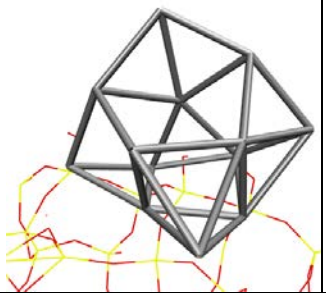	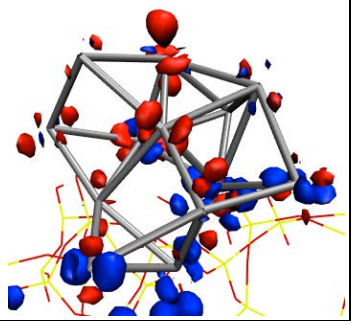

*Difference = Supported - Unsupported (red indicates orbital depletion; blue indicates orbital accumulation)

Table A2.3: LUMO of representative supported and unsupported Pt_{13} clusters. (iso-value: 0.05)

	Cuboctahedral Pt13	Physisorbed; restructured	4 Pt-O Bonds; restructured
Unsupported	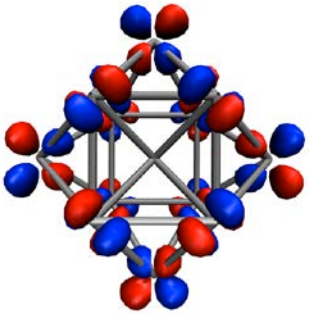	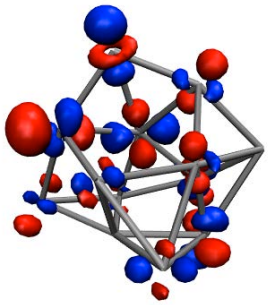	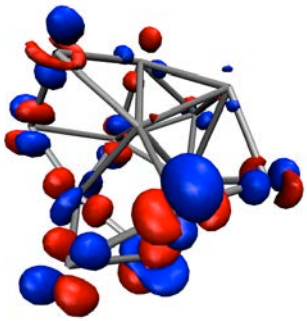
Supported	N/A	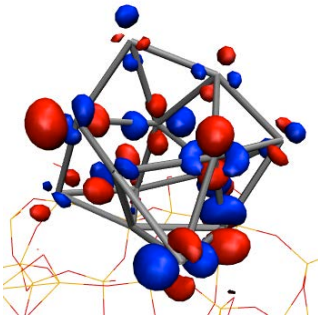	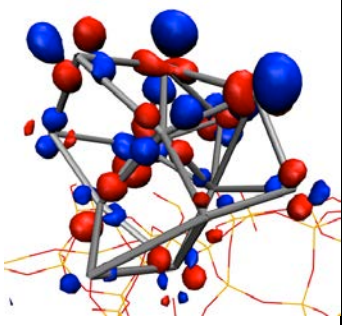
Difference*	N/A	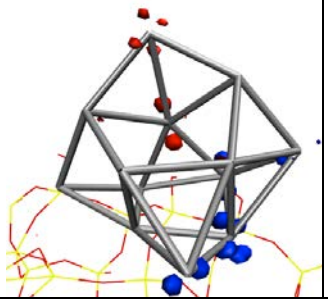	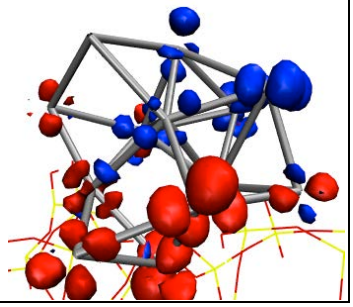

*Difference = Supported – Unsupported (red indicates orbital depletion; blue indicates orbital accumulation)

A.3 EFFECT OF SUPPORT PREPARATION AND NANOPARTICLE SIZE ON CATALYST-SUPPORT INTERACTIONS BETWEEN PT AND AMORPHOUS SILICA

A.3.1 Validation of cell dimensions.

We confirmed that a minimum distance of 6.7 angstroms between Pt_{147} and its periodic image is sufficient by calculating the single-point energy of unsupported Pt_{147} cell dimensions of 24.74 x 36.55 x 47 Å and 28.74 x 36.55 x 47 Å. We can neglect interactions through the silica slab because of its very low dielectric constant (~3). The total system energy and per-atom energy differ by 0.049 and 0.00034 eV, respectively. Table A3.1 shows the corresponding energies.

Table A3.1. Energy of unsupported Pt_{147} for different minimum cell dimension.

x dimension	System Energy (eV)	Energy per atom (eV)
23.75	-480802.9023	-3270.768043
28.74	-480802.853	-3270.767708

A.3.2 Computational Details.

For all DFT calculations we used the CP2K code, which employs a Quickstep[78] implementation of the DFT method using plane waves/pseudopotentials and localized Gaussian basis sets. Calculations used the revised PBE functional (revPBE)[104] and GTH pseudopotentials[81,82] in

conjunction with short range double-ζ basis sets with polarization functions (SR-DZVP).[105] We used a 350 Ry energy cutoff and a 40 Ry rel_cutoff for the plane wave basis set. All surface slabs were relaxed using CP2K treated as periodic in all directions with at least 20 Å of vacuum between slabs to eliminate interactions between the periodic images of the surface slabs. To reduce computational cost, all relaxation calculations were spin-restricted. Electronic analysis calculations (frontier orbital analysis) were performed with spin-polarized DFT. Validation of the planewave energy cutoff, basis sets, vacuum spacing and spin-restricted relaxation have been reported elsewhere.[152] Atomic partial charges were calculated using the Bader Charge Analysis code (version 0.28a) from the Henkelman Group.[135,136] All other post-processing analyses were calculated using in-house Python codes.

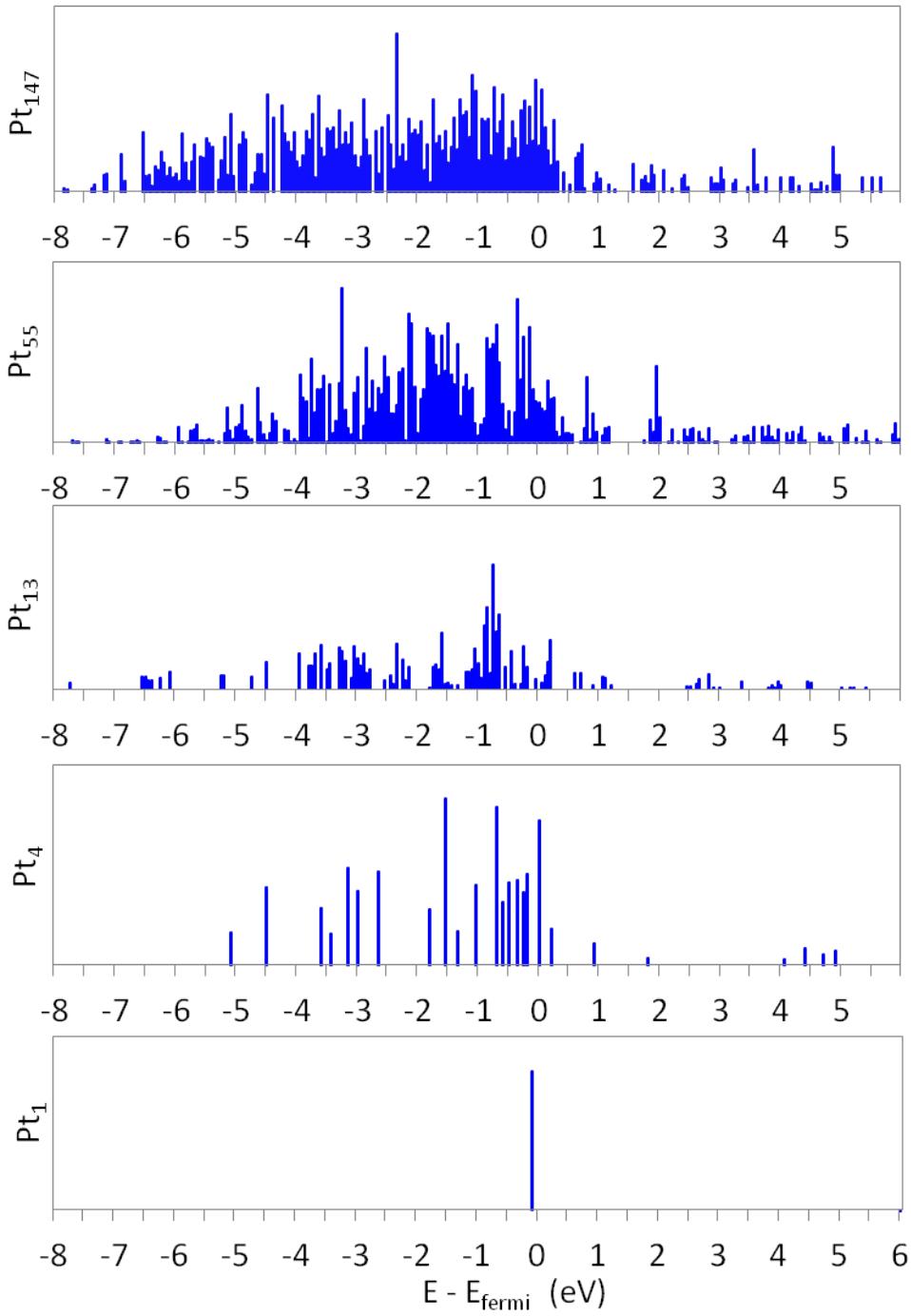

Figure A3.1. The d-density of states for 1, 4, 13, 55, and 147 atom Pt clusters/nanoparticles. Pt_{147} and Pt_{55} have metallic electronic structure: continuous band structure that extends above the Fermi level. The Pt_{13} DOS has a finite gap at the Fermi level.

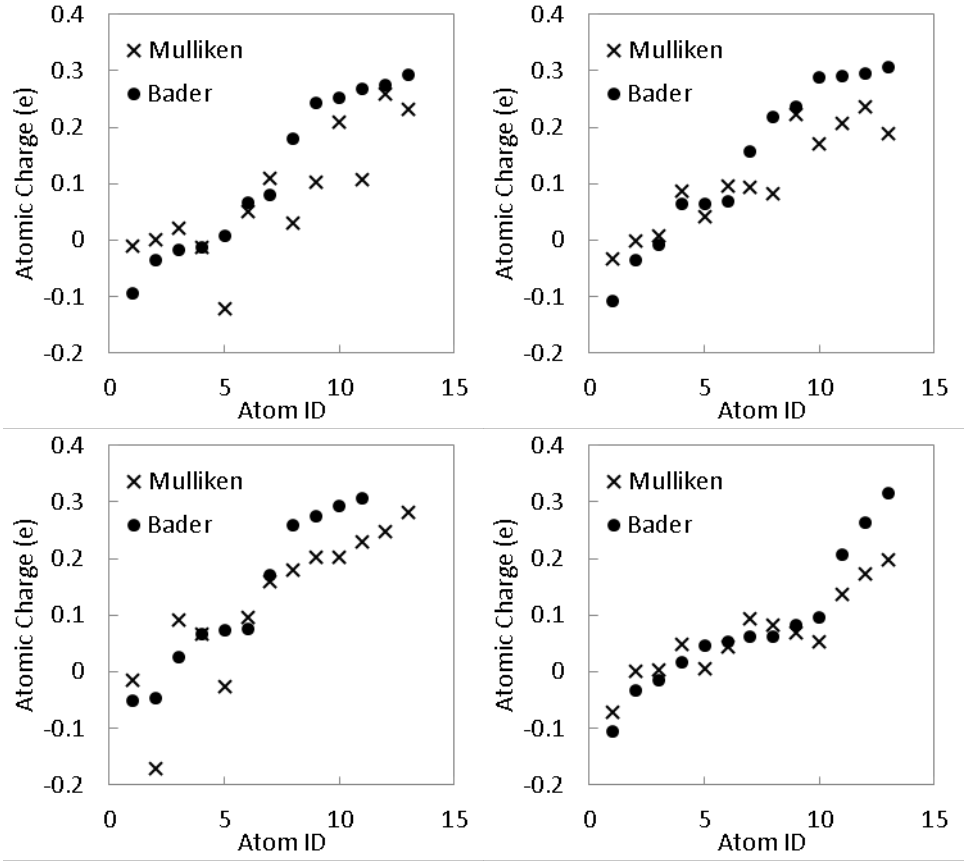

Figure A3.2. Mulliken and Bader charges for four different randomly chosen Pt/SiO_2 systems showing qualitative agreement between the two methods.

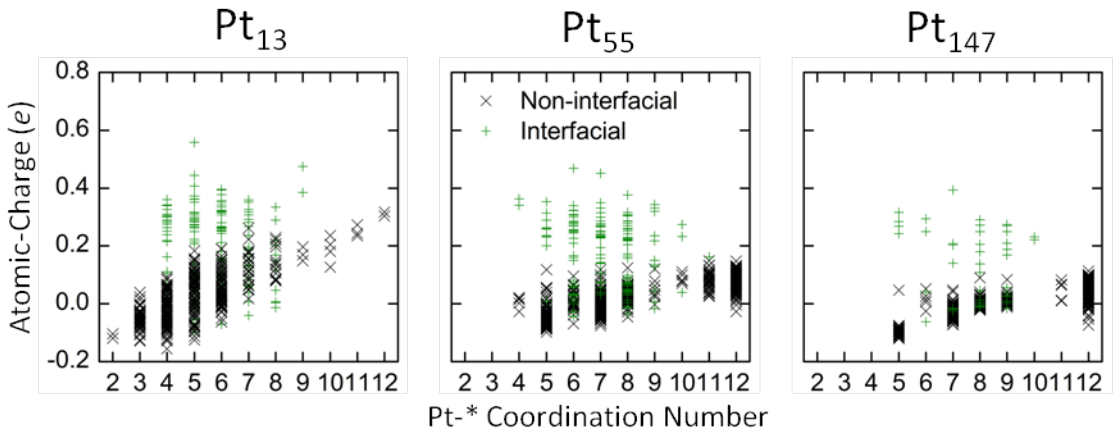

Figure A3.3. Atomic charge vs coordination number for all 13, 55, and 147 atom Pt NPs in this study. Black x symbols and red circles represent interfacial and non-interfacial Pt atoms, respectively. Charge data are from Bader charges calculated using electron density cube files obtained using the same parameters used to for system relaxations.

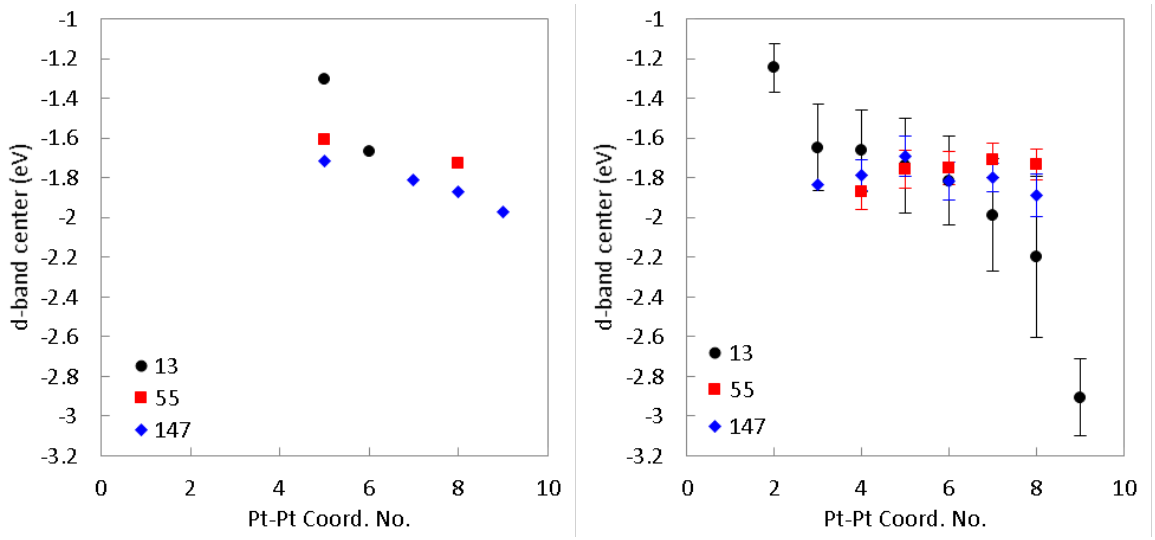

Figure A3.4. d-band centers for individual Pt atoms as a function of Pt coordination number for (a) unsupported and (b) silica-supported, Pt_{13}, Pt_{55}, and Pt_{147}.

A.3.3 d-band center calculation.

The d-band center for each individual Pt atom, d_c, was calculated from the d-density of states of the respective atom as follows:

$$d_c = \frac{\sum \varepsilon_i \rho_i}{\sum \rho_i} \qquad \text{(A3.1)}$$

where ε_i is the eigenvalue of state *i* and ρ_i is the density of state *i*. We considered states with eigenvalues between -8 eV and +6 eV. In agreement with previous studies,[12,15] the d-band center generally correlates with coordination number for the unsupported NPs in Figure A3.4a, where higher coordination numbers generally correspond to lower d-band center. The Pt-silica

interaction clearly introduces some scatter in the d-band center values, however, the general trend is also either reduced significantly (in the case of Pt_{13}) or completely diminished (in the case of Pt_{55} and Pt_{147}). The d-band center and any reliant correlations are thus not applicable to predicting properties of silica-supported Pt nanoparticles

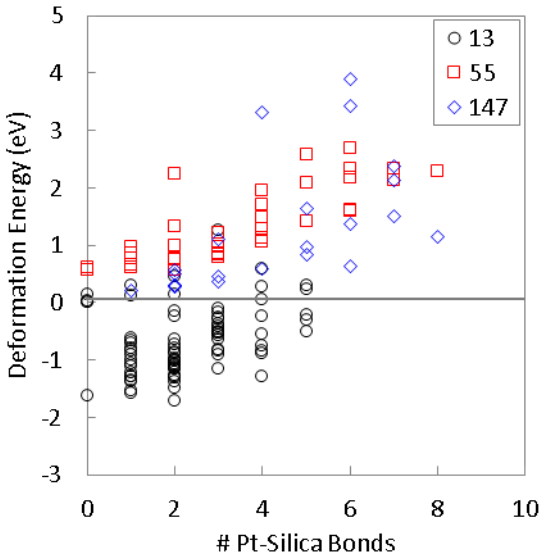

Figure A3.5. Deformation energies for Pt_{13}, Pt_{55}, and Pt_{147}, defined as the change in energy of the Pt atoms associated with relaxation on the silica support.

Table A3.2. Linear fits (second row) of the adhesion energy (y) as a function of the number of Pt-silica bonds (x) and the net NP charge (y') as a function of the number of Pt-silica bonds (x).

	Adhesion	**Charge**
	y = -3.285x – 2.053	y' = 0.457x + 0.0577
Pt_{13}	0.965	0.978
Pt_{55}	0.994	0.992
Pt_{147}	0.969	0.993

The fits were performed only on the Pt_{13} data. Coefficients of determination (R^2) (rows 3-5) computed using the data for the NP in that row using the equation fitted to the Pt_{13} data in the second row.

A.4 PREDICTING CATALYST-SUPPORT INTERACTIONS BETWEEN METAL NANOPARTICLES AND AMORPHOUS SILICA SUPPORTS

A.4.1 Density functional theory calculations.

All DFT calculations performed in this work used the CP2K code, which employs a Quickstep[78] implementation of the DFT method using plane waves/pseudopotentials and localized gaussian basis sets. Calculations used the revised PBE functional (revPBE)[104] and GTH pseudopotentials[81,82] in conjunction with short range double-ζ basis sets with polarization

functions (SR-DZVP).[105] All surface slabs were relaxed using CP2K treated as periodic in all directions with at least 20 Å of vacuum between periodic images in the *z* dimension to eliminate interactions between the periodic images of the surface slabs. The plane wave energy cutoff, basis sets, vacuum spacing and spin-restricted relaxation for these systems have been validated for these systems previously.[130]

A.4.2 Model amorphous silica surfaces.

We used periodic amorphous silica surface structures constructed from a model developed by Ewing *et al.*[103] to investigate NP-surface interactions. These model surface structures are based on first-principles simulations and have been found to accurately predict hydroxyl density and distribution of hydroxyl groups as a function of temperature without any adjustable parameters.[103] Five distinct model surfaces were generated and the hydroxyl density of each system was adjusted using an algorithm to mimic a range of silica pretreatment temperatures T_{pre}, giving a total of 56 different surface structures.[103] For the DFT calculations in this work, we use surface structures having high (4.5 nm^{-2}) and low (1.6 nm^{-2}) hydroxyl densities, corresponding to low (200 °C) and high (570 °C) T_{pre}, respectively. For the discrete element method calculations described below we use all 56 surface structures. The size of the unit cell we used for Pt_{13} calculations was 23.7 Å × 18.3 Å × 32 Å having between 260 and 290 atoms, depending on the corresponding T_{pre} . For 55- and 147-atom NPs we doubled the unit cell size and used two identical copies of the silica slab side-by-side in the *y* direction (resulting in unit cells containing 550 or 690 atoms and having dimensions of 23.7 Å × 36.6 Å × 37 Å for 55-atom NP and 23.7 Å × 36.6 Å × 42 Å for 147-atom NP). The minimum distances between NPs and their periodic images were 11.3, 11.7, and 6.7 Å for 13-, 55-, and 147-atom NPs, respectively.

We recently confirmed that 6.7 Å is sufficient separation to avoid significant error due to self-interaction of the cluster with its periodic image.[150]

A.4.3 Metal nanoparticles.

For the majority of calculations in the present study we use magic number cuboctahedral NPs because the symmetry is independent of size. To investigate the effects of NP geometry on the catalyst-support interactions we also used a theoretical global minimum for Pt_{13} and slab (elongated in the *y* dimension; 3 atomic layers thick) Pt_{55} and Pt_{147}. All NP geometries used in this study are shown in Figure 1. To calculate electronic structure correlations for NPs of different composition we used 13-atom cuboctahedral NPs (Au, Pd, Fe, and Ni) and 147-atom cuboctahedral NPs (Au and Pd).

We divided each of the silica surfaces for Pt_{13}, Pt_{55}, and Pt_{147} into grids of 20 (5×4), 9 (3×3) and 6 (3×2) adsorption locations, respectively. Taking into account the 4 different sets of initial conditions (two NP orientations and two silica surface structures) we generated 80, 36, and 24 systems for DFT calculations of cuboctahedral Pt_{13}, Pt_{55}, and Pt_{147}, respectively. Globaal minimum Pt_{13}Silica surfaces for all 13- and 147-atom Au, Pd, Ni, and Fe NPs were divided into grids of 9 (3×3) and 6 (3×2), respectively. Taking into account two silica surface structures, we generated 18 and 12 systems for DFT calculations of 13- and 147-atom Au, Pd, Ni, and Fe, respectively. More details regarding our general methodology can be found in a previous publication.[130] Expedited DEM simulations were performed for all Pt NPs in this study. For all of these DEM simulations, we divided each silica surface into grids of 80 (10×8) adsorption locations.

A.4.4 Simulating NP adsorption.

We simulated the adsorption of NPs onto the silica surface using discrete element method[110] (DEM) simulations followed by DFT calculations, as described in detail previously.[130] Particle trajectories were obtained in DEM simulations via Newton's laws of motion for each particle at discrete time. For the purpose of our study, the forces in DEM were limited to only gravity, hard-sphere interactions, [115] and tangential friction, where rebounding of particles (atoms) is completely avoided by tuning the viscoelasticity of the particles in the simulations. This allowed for the generation of reasonable initial structures, using negligible computational effort.

Experiments have indicated that noble metal clusters supported on silica form metal-oxygen bonds with the surface hydroxyls during preparation of the NP-silica catalyst systems, whereas metal-silicon bonds are only formed at higher temperatures than typical for post-synthesis calcination.[100,119,134] To best represent experimentally observed metal/silica systems we therefore facilitate M-O bond formation between the NP and any surface hydroxyls that are in contact with metal atoms in the NP by removing the H atom from those hydroxyl groups and reducing the hard-sphere interactions between the interacting M and O atoms to their covalent rather than van der Waals radii. Each of the initialized geometries generated for the DFT studies was fully relaxed to its local minimum using DFT. In addition, we generated many other structures on each of the 56 surfaces using DEM in order to more fully explore the number of metal-silica bonds as a function of NP size and geometry (see below).

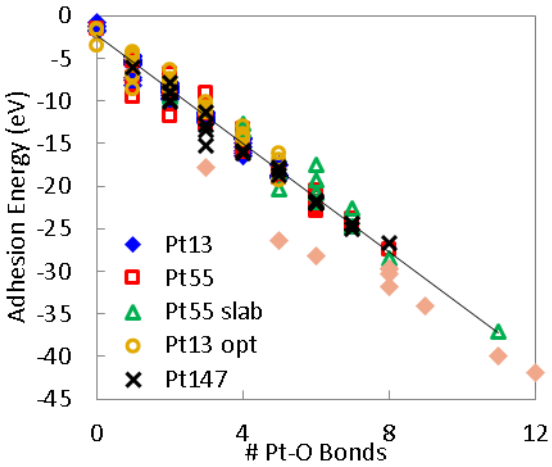

Figure A4.1: Adhesion energy as a function of number of Pt-O bonds for Pt NPs of different size and shape.

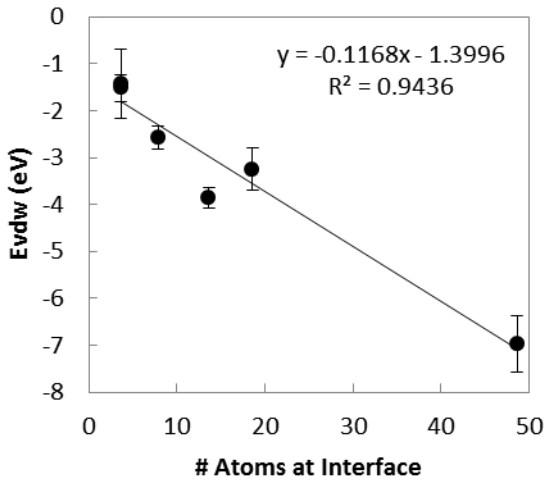

Figure A4.2: Van der Waals forces contributing to NP-silica adhesion energy as a function of number of metal atoms in contact with the support, for all DFT calculations in this study. Each data point corresponds to the average NP-silica van der Waals energy for all systems of a particular NP geometry.

Table A4.1. Linear fits (second row) of the adhesion energy (y) as a function of the number of Pt-silica bonds (x) and the net NP charge (y') as a function of the number of Pt-silica bonds (x).

	Non-vdW Adhesion	Charge
	y = -3.2991 – 0.3752	y' = 0.457x + 0.0577
Pt_{13}	0.979	0.995
Pt_{13} opt	0.924	0.997
Pt_{55}	0.968	0.994
Pt_{55} slab	0.954	0.984
Pt_{147}	0.981	0.994
Pt_{147} slab	0.976	0.969

The fits were performed only on the Pt_{13} data. Coefficients of determination (R^2) (rows 3-5) computed using the data for the NP in that row using the equation fitted to the Pt_{13} data in the second row.

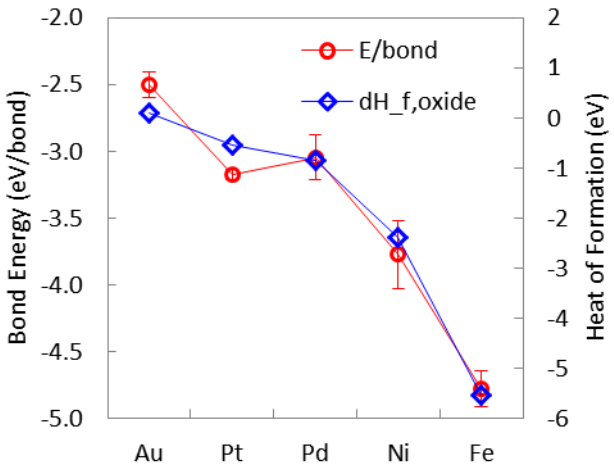

Figure A4.3: Comparing bond energy trend to heats of formation for different metals. Heat of oxide formation values of Au, Pt, Pd,[11] Ni,[153] Fe,[154] are from experimental literature.

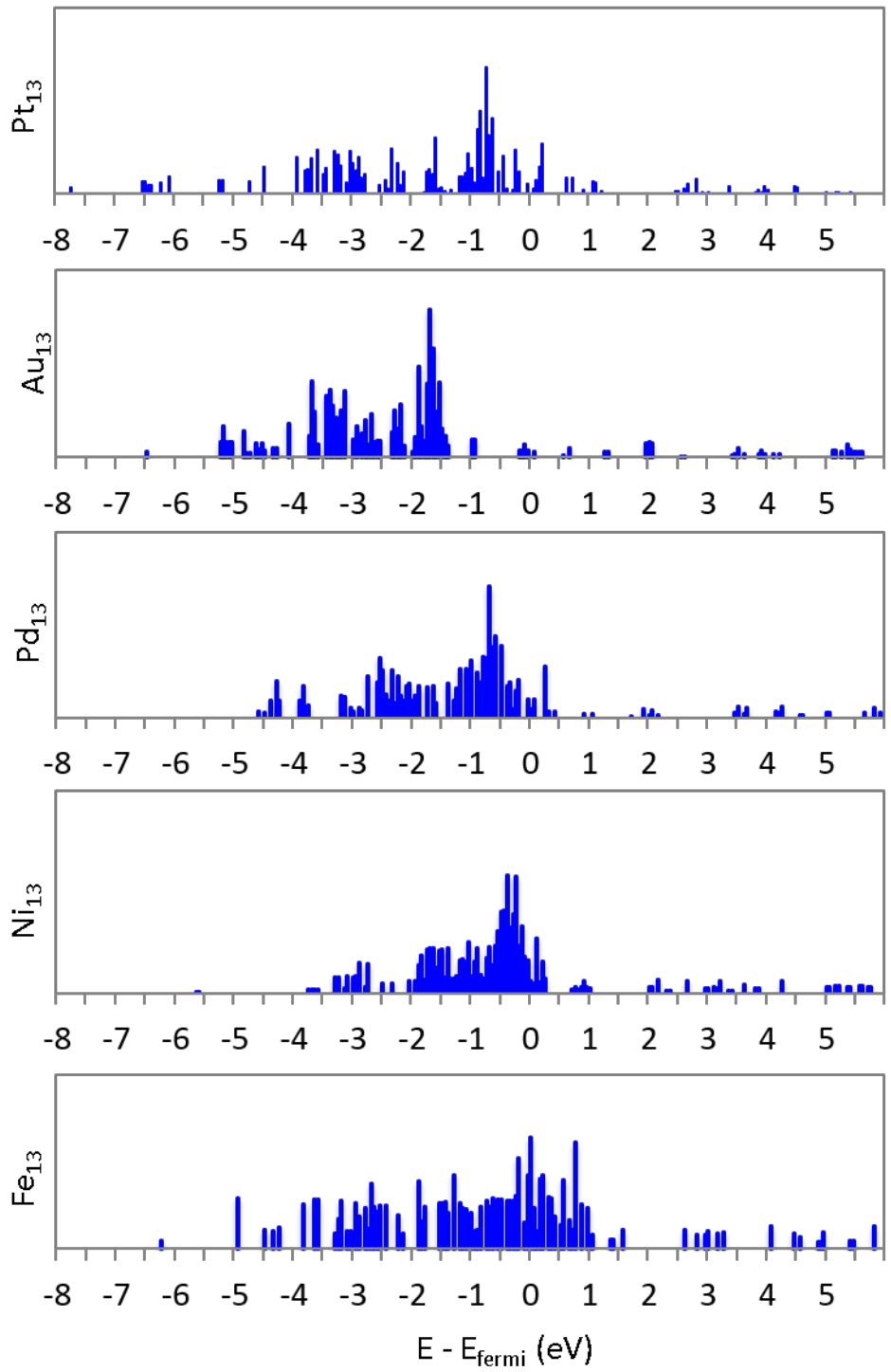

Figure A4.4: The d-density of states for 13 atom Pt, Au, Pd, Ni, and Fe clusters.

Table A4.2: Coefficients of determination (R2) for Au and Pd NPs computed using the data for the NP in that row and a linear fit to the corresponding 13-atom NP data.

	Non-vdW Adhesion	Charge
Pd13	0.959	0.943
Pd147	0.958	0.894
Au13	0.984	0.973
Au147	0.946	0.985

Table A4.3: Parameters for linear fits to the non-vdW adhesion energy per bond for all NPs calculated using DFT in this study.

	Slope (eV/bond)		sdtev(slope)	intercept
Au	-2.335	±	0.088	-2.596
Pt	-3.175	±	0.039	-2.308
Pd	-3.057	±	0.134	-3.468
Ni	-3.771	±	0.255	-2.087
Fe	-4.778	±	0.136	-1.427

Table A4.4: Parameters for linear fits to the net charge per bond for all NPs calculated using DFT in this study.

	Slope (eV/bond)		sdtev(slope)	intercept
Au	0.52	±	0.015	0.146
Pt	0.478	±	0.004	0.001
Pd	0.54	±	0.027	0.269
Ni	0.467	±	0.019	0.462
Fe	0.527	±	0.041	0.518

A.5 ATOMISTIC DESCRIPTION OF ISOLATED MO CENTER CATALYST SITES ON AMORPHOUS SILICA SUPPORTS

A.5.1 Site generation procedure.

In order to allow for easy transformation of these coordinates into surface site structures, the O-O midpoint was placed at the origin, and both Si-bonded O atoms were at $y = z = 0$, and the Si-Si midpoint was at $x = y = 0$. This allowed for calculating atomic coordinates *relative to easily identified structures present in the surface model (i.e., the line between the Si-Si and O-O midpoints and the plane also containing both Si-bonded O atoms).* After identifying silanol pairs on the silica surface models, we generated Mo sites based on the atomic positions of the corresponding cluster models (i.e., bridged or non-bridged and having similar Si-Si distance). First, hydrogen was removed from the anchoring silanol groups. Then, the distance between silanol group O atom positions was reduced to that of the corresponding cluster model. Coordinates for the moiety atoms were then generated from the corresponding cluster model, and then geometrically transformed in accordance with the surface site location.

Geometric transformation was carried out by simple rotation and translation of the moiety, from its initial configuration centered at the origin. Based on the positions of the Si-bonded O atoms and the O-O and Si-Si midpoints, the moiety was rotated about the *x*-axis, rotated about the *y*-axis, rotated about the *z*-axis, and then translated. This procedure produces

atomic coordinates, relative to the Si-O atoms, that are identical to those of the corresponding cluster model. As a result, the initial structures for geometry optimization are rather close to the relaxed structure.

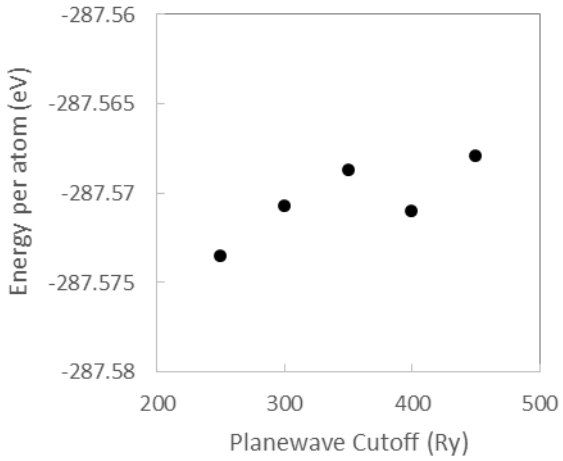

Figure A5.1. Energy per atom vs plane wave energy cutoff for a Mo site on an extended silica surface. All calculations used a plane wave energy relative cutoff of 40 Ry.

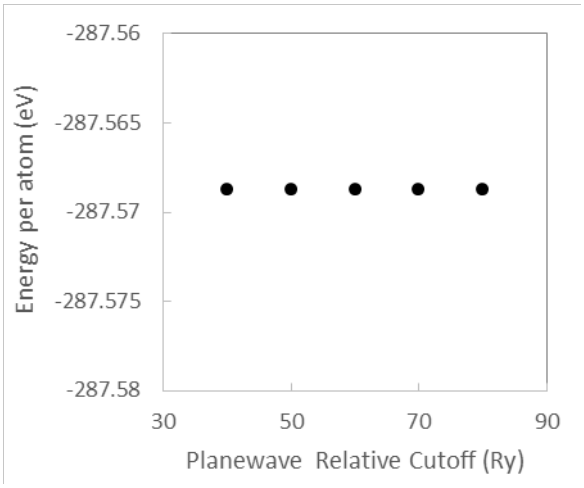

Figure A5.2. Energy per atom vs plane wave energy relative cutoff (REL_CUTOFF) for a Mo site on an extended silica surface. All calculations used a plane wave energy cutoff of 350 Ry.

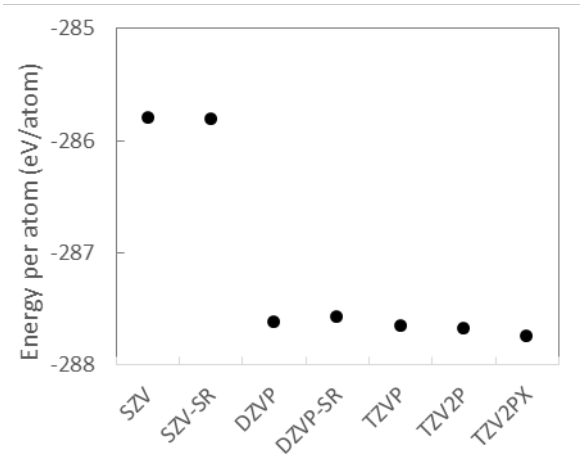

Figure A5.3. Energy per atom of a Mo site on an extended silica surface for different basis sets.

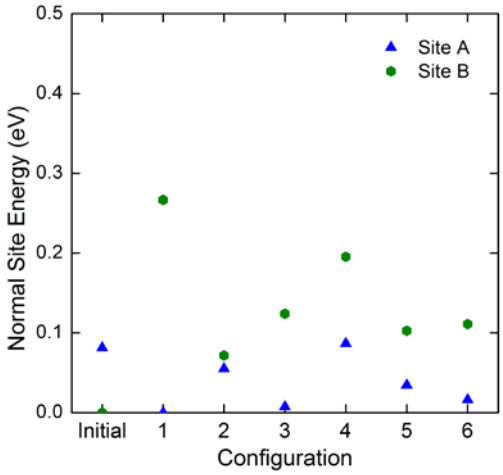

Figure A5.4. Energies of sites generated using our method compared to those after annealing, for two different sites.

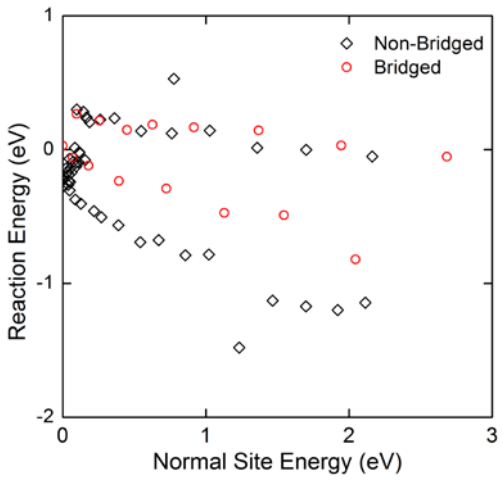

Figure A5.5. Reaction energy vs normal site energy for both bridged and non-bridged cluster models.

A.5.2 Monte Carlo Simulations.

Monte Carlo simulations were performed for three silica pretreatment temperatures. All sites on three silica surface structures were treated as a single sample at each temperature. During each iteration, sites in a sample were randomly populated, consuming the respective silanol group anchors. Full coverage was achieved by populating all sites for which neither silanol group had been consumed. The results were averaged over 1000 iterations for each sample.

BIBLIOGRAPHY

1 Thomas, J. M. & Thomas, W. J. (Wiley-VCH, 1997).

2 Elliott, J. A. Novel approaches to multiscale modelling in materials science. *International Materials Reviews* **56**, 207-225, doi:10.1179/1743280410y.0000000002 (2011).

3 Bromley, S. T., Moreira, I. D. R., Neyman, K. M. & Illas, F. Approaching nanoscale oxides: models and theoretical methods. *Chemical Society Reviews* **38**, 2657-2670, doi:10.1039/b806400h (2009).

4 Fujita, M. & Yamaguchi, Y. Mesoscale modeling for self-organization of colloidal systems. *Current Opinion in Colloid & Interface Science* **15**, 8-12, doi:10.1016/j.cocis.2009.06.001 (2010).

5 Izvekov, S., Violi, A. & Voth, G. A. Systematic coarse-graining of nanoparticle interactions in molecular dynamics simulation. *Journal of Physical Chemistry B* **109**, 17019-17024, doi:10.1021/jp0530496 (2005).

6 Lyubartsev, A., Mirzoev, A., Chen, L. J. & Laaksonen, A. Systematic coarse-graining of molecular models by the Newton inversion method. *Faraday Discussions* **144**, 43-56, doi:10.1039/b901511f (2010).

7 Norskov, J. K., Bligaard, T., Rossmeisl, J. & Christensen, C. H. Towards the computational design of solid catalysts. *Nature Chemistry* **1**, 37-46, doi:10.1038/nchem.121 (2009).

8 Thiel, W. Computational Catalysis-Past, Present, and Future. *Angewandte Chemie-International Edition* **53**, 8605-8613, doi:10.1002/anie.201402118 (2014).

9 Frenkel, A. I. *et al.* An in Situ Study of Bond Strains in 1 nm Pt Catalysts and Their Sensitivities to Cluster-Support and Cluster-Adsorbate Interactions. *Journal of Physical Chemistry C* **117**, 23286-23294, doi:10.1021/jp4062658 (2013).

10 Li, L. *et al.* Noncrystalline-to-Crystalline Transformations in Pt Nanoparticles. *Journal of the American Chemical Society* **135**, 13062-13072, doi:10.1021/ja405497p (2013).

11 Campbell, C. T. & Sellers, J. R. V. Anchored metal nanoparticles: Effects of support and size on their energy, sintering resistance and reactivity. *Faraday Discussions* **162**, 9-30, doi:10.1039/c3fd00094j (2013).

12 Jiang, T. *et al.* Trends in CO Oxidation Rates for Metal Nanoparticles and Close-Packed, Stepped, and Kinked Surfaces. *Journal of Physical Chemistry C* **113**, 10548-10553, doi:10.1021/jp811185g (2009).

13 Li, L. *et al.* Investigation of Catalytic Finite-Size-Effects of Platinum Metal Clusters. *Journal of Physical Chemistry Letters* **4**, 222-226, doi:10.1021/jz3018286 (2013).

14 Lopez, N. *et al.* On the origin of the catalytic activity of gold nanoparticles for low-temperature CO oxidation. *Journal of Catalysis* **223**, 232-235, doi:10.1016/j.jcat.2004.01.001 (2004).

15 Peterson, A. A. *et al.* Finite-Size Effects in O and CO Adsorption for the Late Transition Metals. *Topics in Catalysis* **55**, 1276-1282, doi:10.1007/s11244-012-9908-x (2012).

16 Campbell, C. T., Parker, S. C. & Starr, D. E. The effect of size-dependent nanoparticle energetics on catalyst sintering. *Science* **298**, 811-814, doi:10.1126/science.1075094 (2002).

17 Campbell, C. T. The Energetics of Supported Metal Nanoparticles: Relationships to Sintering Rates and Catalytic Activity. *Accounts of Chemical Research* **46**, 1712-1719, doi:10.1021/ar3003514 (2013).

18 Kim, H. Y. & Henkelman, G. CO Oxidation at the Interface between Doped CeO2 and Supported Au Nanoclusters. *Journal of Physical Chemistry Letters* **3**, 2194-2199, doi:10.1021/jz300631f (2012).

19 Kim, H. Y., Lee, H. M. & Henkelman, G. CO Oxidation Mechanism on CeO2-Supported Au Nanoparticles. *Journal of the American Chemical Society* **134**, 1560-1570, doi:10.1021/ja207510v (2012).

20 Mpourmpakis, G., Andriotis, A. N. & Vlachos, D. G. Identification of Descriptors for the CO Interaction with Metal Nanoparticles. *Nano Letters* **10**, 1041-1045, doi:10.1021/nl904299c (2010).

21 Mpourmpakis, G. & Vlachos, D. G. The Effects of the MgO Support and Alkali Doping on the CO Interaction with Au. *Journal of Physical Chemistry C* **113**, 7329-7335, doi:10.1021/jp900198m (2009).

22 Stamatakis, M., Christiansen, M. A., Vlachos, D. G. & Mpourmpakis, G. Multiscale Modeling Reveals Poisoning Mechanisms of MgO-Supported Au Clusters in CO Oxidation. *Nano Letters* **12**, 3621-3626, doi:10.1021/nl301318b (2012).

23 Yaguee, C., Moros, M., Grazu, V., Arruebo, M. & Santamaria, J. Synthesis and stealthing study of bare and PEGylated silica micro- and nanoparticles as potential drug-delivery vectors. *Chem. Eng. J.* **137**, 45-53, doi:10.1016/j.cej.2007.07.088 (2008).

24 Deak, A., Bancsi, B., Toth, A. L., Kovacs, A. L. & Horvolgyi, Z. Complex Langmuir-Blodgett films from silica nanoparticles: An optical spectroscopy study. *Colloids Surf., A* **278**, 10-16, doi:10.1016/j.colsurfa.2005.11.070 (2006).

25 Deak, A. *et al.* Nanostructured silica Langmuir-Blodgett films with antireflective properties prepared on glass substrates. *Thin Solid Films* **484**, 310-317, doi:10.1016/j.tsf.2005.01.096 (2005).

26 Wang, S. F. *et al.* Silica coating on ultrafine alpha-alumina particles. *Mater. Sci. Eng., A* **395**, 148-152, doi:10.1016/j.msea.2004.12.007 (2005).

27 Yang, H. P. & Zhu, Y. F. Size dependence of SiO2 particles enhanced glucose biosensor. *Talanta* **68**, 569-574, doi:10.1016/j.talanta.2005.04.057 (2006).

28 An, N. H. *et al.* Catalytic oxidation of formaldehyde over different silica supported platinum catalysts. *Chemical Engineering Journal* **215**, 1-6, doi:10.1016/j.cej.2012.10.096 (2013).

29 Kim, M. Y. *et al.* Platinum catalysts supported on silicas: effect of silica characteristics on their catalytic activity in carbon monoxide oxidation. *Reaction Kinetics Mechanisms and Catalysis* **103**, 463-479, doi:10.1007/s11144-011-0324-1 (2011).

30 Rozanska, X., Delbecq, F. & Sautet, P. Reconstruction and stability of beta-cristobalite 001, 101, and 111 surfaces during dehydroxylation. *Physical Chemistry Chemical Physics* **12**, 14930-14940, doi:10.1039/c0cp00287a (2010).

31 Tielens, F., Gervais, C., Lambert, J. F., Mauri, F. & Costa, D. Ab initio study of the hydroxylated surface of amorphous silica: A representative model. *Chemistry of Materials* **20**, 3336-3344, doi:10.1021/cm8001173 (2008).

32 Ugliengo, P. *et al.* Realistic Models of Hydroxylated Amorphous Silica Surfaces and MCM-41 Mesoporous Material Simulated by Large-scale Periodic B3LYP Calculations. *Adv. Mater.* **20**, 4579-4583, doi:10.1002/adma.200801489 (2008).

33 Zhuravlev, L. T. The surface chemistry of amorphous silica. Zhuravlev model. *Colloids and Surfaces a-Physicochemical and Engineering Aspects* **173**, 1-38, doi:10.1016/s0927-7757(00)00556-2 (2000).

34 Puurunen, R. L., Lindblad, M., Root, A. & Krause, A. O. I. Successive reactions of gaseous trimethylaluminium and ammonia on porous alumina. *Physical Chemistry Chemical Physics* **3**, 1093-1102, doi:10.1039/b007249o (2001).

35 Sindorf, D. W. & Maciel, G. E. SI-29 NMR-STUDY OF DEHYDRATED REHYDRATED SILICA-GEL USING CROSS POLARIZATION AND MAGIC-ANGLE SPINNING. *Journal of the American Chemical Society* **105**, 1487-1493, doi:10.1021/ja00344a012 (1983).

36 Sindorf, D. W. & Maciel, G. E. SI-29 NUCLEAR MAGNETIC-RESONANCE STUDY OF HYDROXYL SITES ON DEHYDRATED SILICA-GEL SURFACES, USING SILYLATION AS A PROBE. *Journal of Physical Chemistry* **87**, 5516-5521, doi:10.1021/j150644a041 (1983).

37 Wang, Y., Zahid, F., Wang, J. & Guo, H. Structure and dielectric properties of amorphous high-kappa oxides: HfO2, ZrO2, and their alloys. *Physical Review B* **85**, 5, doi:10.1103/PhysRevB.85.224110 (2012).

38 Campbell, C. T. & Sellers, J. R. V. Anchored metal nanoparticles: Effects of support and size on their energy, sintering resistance and reactivity. *Faraday Discussions* **162**, 9-30, doi:10.1039/c3fd00094j (2013).

39 Chretien, S., Buratto, S. K. & Metiu, H. Catalysis by very small Au clusters. *Current Opinion in Solid State & Materials Science* **11**, 62-75, doi:10.1016/j.cossms.2008.07.003 (2007).

40 Jiang, C. X., Hara, K. & Fukuoka, A. Low-Temperature Oxidation of Ethylene over Platinum Nanoparticles Supported on Mesoporous Silica. *Angewandte Chemie, International Edition* **52**, 6265-6268, doi:10.1002/anie.201300496 (2013).

41 Jiang, T. *et al.* Trends in CO Oxidation Rates for Metal Nanoparticles and Close-Packed, Stepped, and Kinked Surfaces. *The Journal of Physical Chemistry C* **113**, 10548-10553, doi:10.1021/jp811185g (2009).

42 Kim, M.-Y. *et al.* Preparation of Highly Dispersive and Stable Platinum Catalysts Supported on Siliceous SBA-15 Mesoporous Material: Roles of Titania Layer Incorporation and Hydrogen Peroxide Treatment. *Catal Lett* **129**, 194-206, doi:10.1007/s10562-008-9790-0 (2009).

43 Kim, M.-Y., Park, J.-H., Shin, C.-H., Han, S.-W. & Seo, G. Dispersion Improvement of Platinum Catalysts Supported on Silica, Silica-Alumina and Alumina by Titania Incorporation and pH Adjustment. *Catalysis Letters* **133**, 288-297, doi:10.1007/s10562-009-0188-4 (2009).

44 Peterson, A. *et al.* Finite-Size Effects in O and CO Adsorption for the Late Transition Metals. *Top Catal* **55**, 1276-1282, doi:10.1007/s11244-012-9908-x (2012).

45 Mpourmpakis, G. & Vlachos, D. G. The Effects of the MgO Support and Alkali Doping on the CO Interaction with Au. *The Journal of Physical Chemistry C* **113**, 7329-7335, doi:10.1021/jp900198m (2009).

46 Kim, H. Y., Lee, H. M. & Henkelman, G. CO Oxidation Mechanism on CeO2-Supported Au Nanoparticles. *Journal of the American Chemical Society* **134**, 1560-1570, doi:10.1021/ja207510v (2011).

47 Li, L. *et al.* Investigation of Catalytic Finite-Size-Effects of Platinum Metal Clusters. *The Journal of Physical Chemistry Letters* **4**, 222-226, doi:10.1021/jz3018286 (2012).

48 Huang, S., Hara, K. & Fukuoka, A. Intrinsic Catalytic Role of Mesoporous Silica in Preferential Oxidation of Carbon Monoxide in Excess Hydrogen. *Chemistry – A European Journal* **18**, 4738-4747, doi:10.1002/chem.201102256 (2012).

49 Kleis, J. *et al.* Finite Size Effects in Chemical Bonding: From Small Clusters to Solids. *Catalysis Letters* **141**, 1067-1071, doi:10.1007/s10562-011-0632-0 (2011).

50 Mowbray, D. J. *et al.* Trends in Metal Oxide Stability for Nanorods, Nanotubes, and Surfaces. *Journal of Physical Chemistry C* **115**, 2244-2252, doi:10.1021/jp110489u (2011).

51 Korach, L., Czaja, K. & Kovaleva, N. Y. Sol-gel material as a support of organometallic catalyst for ethylene polymerization. *European Polymer Journal* **44**, 889-903, doi:10.1016/j.eurpolymj.2007.11.037 (2008).

52 Zhuravlev, L. T. The surface chemistry of amorphous silica. Zhuravlev model. *Colloids Surf., A* **173**, 1-38, doi:10.1016/s0927-7757(00)00556-2 (2000).

53 Zhuravlev, L. T. STRUCTURALLY BOUND WATER AND SURFACE CHARACTERIZATION OF AMORPHOUS SILICA. *Pure and Applied Chemistry* **61**, 1969-1976, doi:10.1351/pac198961111969 (1989).

54 Zhuravlev, L. T. Surface characterization of amorphous silica - A review of work from the former USSR. *Colloids Surf., A* **74**, 71-90, doi:10.1016/0927-7757(93)80399-y (1993).

55 Sindorf, D. W. & Maciel, G. E. ^{29}Si nuclear magnetic-resonance study of hydroxyl sites on dehydrated silica-gel surfaces, using silylation as a probe. *J. Phys. Chem.* **87**, 5516-5521, doi:10.1021/j150644a041 (1983).

56 Wang, Y., Zahid, F., Wang, J. & Guo, H. Structure and dielectric properties of amorphous high-kappa oxides: HfO_2, ZrO_2, and their alloys. *Phys. Rev. B* **85**, 224110, doi:10.1103/PhysRevB.85.224110 (2012).

57 Butenuth, A. *et al.* Ab initio derived force-field parameters for molecular dynamics simulations of deprotonated amorphous-SiO2/water interfaces. *Physica Status Solidi B-Basic Solid State Physics* **249**, 292-305, doi:10.1002/pssb.201100786 (2012).

58 Cruz-Chu, E. R., Aksimentiev, A. & Schulten, K. Water-silica force field for simulating nanodevices. *Journal of Physical Chemistry B* **110**, 21497-21508, doi:10.1021/jp063896o (2006).

59 Du, J. C. & Cormack, A. N. Molecular dynamics simulation of the structure and hydroxylation of silica glass surfaces. *Journal of the American Ceramic Society* **88**, 2532-2539, doi:10.1111/j.1551-2916.2005.00352.x (2005).

60 Fogarty, J. C., Aktulga, H. M., Grama, A. Y., van Duin, A. C. T. & Pandit, S. A. A reactive molecular dynamics simulation of the silica-water interface. *J. Chem. Phys.* **132**, 174704, doi:10.1063/1.3407433 (2010).

61 Hassanali, A. A. & Singer, S. J. Model for the water-amorphous silica interface: The undissociated surface. *Journal of Physical Chemistry B* **111**, 11181-11193, doi:10.1021/jo062971s (2007).

62 Hassanali, A. A., Zhang, H., Knight, C., Shin, Y. K. & Singer, S. J. The Dissociated Amorphous Silica Surface: Model Development and Evaluation. *Journal of Chemical Theory and Computation* **6**, 3456-3471, doi:10.1021/ct100260z (2010).

63 Pedone, A. *et al.* FFSiOH: a new force field for silica polymorphs and their hydroxylated surfaces based on periodic B3LYP calculations. *Chemistry of Materials* **20**, 2522-2531, doi:10.1021/cm703437y (2008).

64 Kramer, G. J., Farragher, N. P., van Beest, B. W. H. & van Santen, R. A. Interatomic force fields for silicas, aluminophosphates, and zeolites: Derivation based on ab initio calculations *Phys. Rev. B* **43**, 5068-5080, doi:10.1103/PhysRevB.43.5068 (1991).

65 Heinz, H., Lin, T. J., Mishra, R. K. & Emami, F. S. Thermodynamically Consistent Force Fields for the Assembly of Inorganic, Organic, and Biological Nanostructures: The INTERFACE Force Field. *Langmuir* **29**, 1754-1765, doi:10.1021/la3038846 (2013).

66 Digne, M., Sautet, P., Raybaud, P., Euzen, P. & Toulhoat, H. Use of DFT to achieve a rational understanding of acid-basic properties of gamma-alumina surfaces. *Journal of Catalysis* **226**, 54-68, doi:10.1016/j.jcat.2004.04.020 (2004).

67 Aktulga, H. M., Fogarty, J. C., Pandit, S. A. & Grama, A. Y. Parallel reactive molecular dynamics: Numerical methods and algorithmic techniques. *Parallel Computing* **38**, 245-259, doi:10.1016/j.parco.2011.08.005 (2012).

68 Plimpton, S. FAST PARALLEL ALGORITHMS FOR SHORT-RANGE MOLECULAR-DYNAMICS. *Journal of Computational Physics* **117**, 1-19, doi:10.1006/jcph.1995.1039 (1995).

69 Siboulet, B., Coasne, B., Dufreche, J. F. & Turq, P. Hydrophobic Transition in Porous Amorphous Silica. *Journal of Physical Chemistry B* **115**, 7881-7886, doi:10.1021/jp203193k (2011).

70 Bakaev, V. A. & Steele, W. A. On the computer simulation of a hydrophobic vitreous silica surface. *Journal of Chemical Physics* **111**, 9803-9812, doi:10.1063/1.480317 (1999).

71 Bolt, G. H. DETERMINATION OF THE CHARGE DENSITY OF SILICA SOLS. *Journal of Physical Chemistry* **61**, 1166-1169, doi:10.1021/j150555a007 (1957).

72 Patwardhan, S. V. *et al.* Chemistry of Aqueous Silica Nanoparticle Surfaces and the Mechanism of Selective Peptide Adsorption. *Journal of the American Chemical Society* **134**, 6244-6256, doi:10.1021/ja211307u (2012).

73 Zerrouk, R., Foissy, A., Mercier, R., Chevallier, Y. & Morawski, J. C. Study of Ca^{2+}-induced silica coagulation by small angle scattering. *J. Colloid Interface Sci.* **139**, 20-29, doi:10.1016/0021-9797(90)90441-p (1990).

74 Krack, M. & Parrinello, M. All-electron ab-initio molecular dynamics. *Physical Chemistry Chemical Physics* **2**, 2105-2112, doi:10.1039/b001167n (2000).

75 Lippert, G., Hutter, J. & Parrinello, M. A hybrid Gaussian and plane wave density functional scheme. *Molecular Physics* **92**, 477-487, doi:10.1080/002689797170220 (1997).

76 Lippert, G., Hutter, J. & Parrinello, M. The Gaussian and augmented-plane-wave density functional method for ab initio molecular dynamics simulations. *Theoretical Chemistry Accounts* **103**, 124-140, doi:10.1007/s002140050523 (1999).

77 VandeVondele, J. & Hutter, J. An efficient orbital transformation method for electronic structure calculations. *Journal of Chemical Physics* **118**, 4365-4369, doi:10.1063/1.1543154 (2003).

78 VandeVondele, J. *et al.* QUICKSTEP: Fast and accurate density functional calculations using a mixed Gaussian and plane waves approach. *Computer Physics Communications* **167**, 103-128, doi:10.1016/j.cpc.2004.12.014 (2005).

79 Goumans, T. P. M., Wander, A., Brown, W. A. & Catlow, C. R. A. Structure and stability of the (001) alpha-quartz surface. *Physical Chemistry Chemical Physics* **9**, 2146-2152, doi:10.1039/b701176h (2007).

80 Perdew, J. P., Burke, K. & Ernzerhof, M. Generalized gradient approximation made simple. *Physical Review Letters* **77**, 3865-3868, doi:10.1103/PhysRevLett.77.3865 (1996).

81 Goedecker, S., Teter, M. & Hutter, J. Separable dual-space Gaussian pseudopotentials. *Physical Review B* **54**, 1703-1710, doi:10.1103/PhysRevB.54.1703 (1996).

82 Krack, M. Pseudopotentials for H to Kr optimized for gradient-corrected exchange-correlation functionals. *Theoretical Chemistry Accounts* **114**, 145-152, doi:10.1007/s00214-005-0655-y (2005).

83 VandeVondele, J. & Hutter, J. Gaussian basis sets for accurate calculations on molecular systems in gas and condensed phases. *Chem. Phys.* **127**, 114105 (2007).

84 Wang, J. Z. *et al.* Two-Phase Synthesis of Monodisperse Silica Nanospheres with Amines or Ammonia Catalyst and Their Controlled Self-Assembly. *Acs Applied Materials & Interfaces* **3**, 1538-1544, doi:10.1021/am200104m (2011).

85 Ismail, I. M. K. CROSS-SECTIONAL AREAS OF ADSORBED N2, AR, KR, AND O2 ON CARBONS AND FUMED SILICAS AT LIQUID-NITROGEN TEMPERATURE. *Langmuir* **8**, 360-365, doi:10.1021/la00038a006 (1992).

86 Digne, M., Sautet, P., Raybaud, P., Euzen, P. & Toulhoat, H. Hydroxyl groups on gamma-alumina surfaces: A DFT study. *Journal of Catalysis* **211**, 1-5, doi:10.1006/jcat.2002.3741 (2002).

87 Digne, M., Sautet, P., Raybaud, P., Toulhoat, H. & Artacho, E. Structure and stability of aluminum hydroxides: A theoretical study. *Journal of Physical Chemistry B* **106**, 5155-5162, doi:10.1021/jp014182a (2002).

88 Krokidis, X. *et al.* Theoretical study of the dehydration process of boehmite to gamma-alumina. *Journal of Physical Chemistry B* **105**, 5121-5130, doi:10.1021/jp0038310 (2001).

89 Arunan, E. *et al.* Defining the hydrogen bond: An account (IUPAC Technical Report). *Pure and Applied Chemistry* **83**, 1619-1636, doi:10.1351/pac-rep-10-01-01 (2011).

90 Aguiar, H., Serra, J., Gonzalez, P. & Leon, B. Structural study of sol-gel silicate glasses by IR and Raman spectroscopies. *Journal of Non-Crystalline Solids* **355**, 475-480, doi:10.1016/j.jnoncrysol.2009.01.010 (2009).

91 Burneau, A., Barres, O., Gallas, J. P. & Lavalley, J. C. Comparative-study of the surface hydroxyl-groups of fumed and precipitated silicas 2. Characterization by infrared-spectroscopy of the interactions with water. *Langmuir* **6**, 1364-1372, doi:10.1021/la00098a008 (1990).

92 Morrow, B. A., Cody, I. A. & Lee, L. S. M. Infrared studies of reactions on oxide surfaces. 7. Mechanism of adsorption of water and ammonia on dehydroxylated silica. *J. Phys. Chem.* **80**, 2761-2767, doi:10.1021/j100566a009 (1976).

93 Musso, F., Sodupe, M., Corno, M. & Ugliengo, P. H-Bond Features of Fully Hydroxylated Surfaces of Crystalline Silica Polymorphs: A Periodic B3LYP Study. *Journal of Physical Chemistry C* **113**, 17876-17884, doi:10.1021/jp905325m (2009).

94 D'Souza, A. S. & Pantano, C. G. Hydroxylation and dehydroxylation behavior of silica glass fracture surfaces. *Journal of the American Ceramic Society* **85**, 1499-1504 (2002).

95 Gallas, J. P. *et al.* Quantification of Water and Silanol Species on Various Silicas by Coupling IR Spectroscopy and in-Situ Thermogravimetry. *Langmuir* **25**, 5825-5834, doi:10.1021/la802688w (2009).

96 Mrowiec-Bialon, J. Determination of hydroxyls density in the silica-mesostructured cellular foams by thermogravimetry. *Thermochimica Acta* **443**, 49-52, doi:10.1016/j.tca.2005.12.014 (2006).

97 Kim, M.-Y. *et al.* Preparation of Highly Dispersive and Stable Platinum Catalysts Supported on Siliceous SBA-15 Mesoporous Material: Roles of Titania Layer Incorporation and Hydrogen Peroxide Treatment. *Catalysis Letters* **129**, 194-206, doi:10.1007/s10562-008-9790-0 (2009).

98 Hu, C. H. *et al.* Modulation of catalyst particle structure upon support hydroxylation: Ab initio insights into Pd-13 and Pt-13/gamma-Al2O3. *Journal of Catalysis* **274**, 99-110, doi:10.1016/j.jcat.2010.06.009 (2010).

99 Eswaramoorthy, M. *et al.* The conversion of methane with silica-supported platinum catalysts: the effect of catalyst preparation method and platinum particle size. *Catalysis Letters* **71**, 55-61, doi:10.1023/a:1016652207819 (2001).

100 Min, B. K., Santra, A. K. & Goodman, D. W. Understanding silica-supported metal catalysts: Pd/silica as a case study. *Catalysis Today* **85**, 113-124, doi:10.1016/s0920-5861(03)00380-8 (2003).

101 Huang, S. J., Hara, K. & Fukuoka, A. Intrinsic Catalytic Role of Mesoporous Silica in Preferential Oxidation of Carbon Monoxide in Excess Hydrogen. *Chemistry--A European Journal* **18**, 4738-4747, doi:10.1002/chem.201102256 (2012).

102 Cargnello, M. *et al.* Control of Metal Nanocrystal Size Reveals Metal-Support Interface Role for Ceria Catalysts. *Science* **341**, 771-773, doi:10.1126/science.1240148 (2013).

103 Ewing, C. S., Bhavsar, S., Veser, G., McCarthy, J. J. & Johnson, J. K. Accurate Amorphous Silica Surface Models from First-Principles Thermodynamics of Surface Dehydroxylation. *Langmuir* **30**, 5133-5141, doi:10.1021/la500422p (2014).

104 Hammer, B., Hansen, L. B. & Norskov, J. K. Improved adsorption energetics within density-functional theory using revised Perdew-Burke-Ernzerhof functionals. *Physical Review B* **59**, 7413-7421, doi:10.1103/PhysRevB.59.7413 (1999).

105 VandeVondele, J. & Hutter, J. Gaussian basis sets for accurate calculations on molecular systems in gas and condensed phases. *Journal of Chemical Physics* **127**, doi:10.1063/1.2770708 (2007).

106 Fogarty, J. C., Aktulga, H. M., Grama, A. Y., van Duin, A. C. T. & Pandit, S. A. A reactive molecular dynamics simulation of the silica-water interface. *Journal of Chemical Physics* **132**, doi:10.1063/1.3407433 (2010).

107 Chou, J. P., Hsing, C. R., Wei, C. M., Cheng, C. & Chang, C. M. Ab initio random structure search for 13-atom clusters of fcc elements. *Journal of Physics-Condensed Matter* **25**, doi:10.1088/0953-8984/25/12/125305 (2013).

108 Cuenya, B. R. *et al.* Solving the Structure of Size-Selected Pt Nanocatalysts Synthesized by Inverse Micelle Encapsulation. *Journal of the American Chemical Society* **132**, 8747-8756, doi:10.1021/ja101997z (2010).

109 Cuenya, B. R. *et al.* Anomalous lattice dynamics and thermal properties of supported size- and shape-selected Pt nanoparticles. *Physical Review B* **82**, doi:10.1103/PhysRevB.82.155450 (2010).

110 Cuenya, B. R. *et al.* Thermodynamic properties of Pt nanoparticles: Size, shape, support, and adsorbate effects. *Physical Review B* **84**, doi:10.1103/PhysRevB.84.245438 (2011).

111 Mostafa, S. *et al.* Shape-Dependent Catalytic Properties of Pt Nanoparticles. *Journal of the American Chemical Society* **132**, 15714-15719, doi:10.1021/ja106679z (2010).

112 Xu, D., Liu, Y. J., Zhao, J. X., Cai, Q. H. & Wang, X. Z. Theoretical Study of the Deposition of Pt Clusters on Defective Hexagonal Boron Nitride (h-BN) Sheets: Morphologies, Electronic Structures, and Interactions with 0. *Journal of Physical Chemistry C* **118**, 8868-8876, doi:10.1021/jp4087943 (2014).

113 Bartolome, J. *et al.* Magnetization of Pt-13 clusters supported in a NaY zeolite: A XANES and XMCD study. *Physical Review B* **80**, 10, doi:10.1103/PhysRevB.80.014404 (2009).

114 Cundall, P. A. & Strack, O. D. L. DISCRETE NUMERICAL-MODEL FOR GRANULAR ASSEMBLIES. *Geotechnique* **29**, 47-65 (1979).

115 Johnson, K. L. *Contact Mechanics*. (Cambridge: Cambridge University Press, 1987).

116 Humphrey, W., Dalke, A. & Schulten, K. VMD: Visual molecular dynamics. *Journal of Molecular Graphics & Modelling* **14**, 33-38, doi:10.1016/0263-7855(96)00018-5 (1996).

117 McCarthy, J. J. & Ottino, J. M. Particle dynamics simulation: a hybrid technique applied to granular mixing. *Powder Technology* **97**, 91-99, doi:10.1016/s0032-5910(97)03391-3 (1998).

118 Moroz, E. M., Kriventsov, V. V. & Kochubei, D. I. EuroPt-1 catalyst: Radial distribution of electron density X-ray diffraction and EXAFS studies. *Journal of Structural Chemistry (Translation of Zhurnal Strukturnoi Khimii)* **50**, 1082-1087, doi:10.1007/s10947-009-0159-z (2009).

119 Schwartz, J. M. & Schmidt, L. D. MICROSTRUCTURES OF PT-CE AND RH-CE PARTICLES ON ALUMINA AND SILICA. *Journal of Catalysis* **138**, 283-293, doi:10.1016/0021-9517(92)90023-b (1992).

120 Kalakkad, D., Datye, A. K. & Robota, H. INTERACTION OF PLATINUM AND CERIA PROBED BY TRANSMISSION ELECTRON-MICROSCOPY AND CATALYTIC REACTIVITY. *Applied Catalysis, B: Environmental* **1**, 191-219, doi:10.1016/0926-3373(92)80023-s (1992).

121 Libuda, J. *et al.* Interaction of rhodium with hydroxylated alumina model substrates. *Surface Science* **384**, 106-119, doi:10.1016/s0039-6028(97)00170-2 (1997).

122 Luo, Y. R. (CRC Press, Boca Raton, FL, 2007).

123 Mavrikakis, M., Hammer, B. & Norskov, J. K. Effect of strain on the reactivity of metal surfaces. *Physical Review Letters* **81**, 2819-2822, doi:10.1103/PhysRevLett.81.2819 (1998).

124 Wallace, W. T. & Whetten, R. L. Carbon monoxide adsorption on selected gold clusters: Highly size-dependent activity and saturation compositions. *Journal of Physical Chemistry B* **104**, 10964-10968, doi:10.1021/jp002889b (2000).

125 Rodriguez, J. A., Truong, C. M. & Goodman, D. W. INFRARED VIBRATIONAL STUDIES OF CO ADSORPTION ON CU/PT(111) AND CUPT(111) SURFACES. *Journal of Chemical Physics* **96**, 7814-7825, doi:10.1063/1.462378 (1992).

126 Hammer, B. & Norskov, J. K. Electronic factors determining the reactivity of metal surfaces. *Surface Science* **343**, 211-220, doi:10.1016/0039-6028(96)80007-0 (1995).

127 Nilsson, A. *et al.* The electronic structure effect in heterogeneous catalysis. *Catalysis Letters* **100**, 111-114, doi:10.1007/s10562-004-3434-9 (2005).

128 Lee, C. K. & Hua, C. C. Nanoparticle interaction potentials constructed by multiscale computation. *Journal of Chemical Physics* **132**, doi:10.1063/1.3447890 (2010).

129 Kleis, J. *et al.* Finite-size effects in surface chemistry of gold nanoparticles. *Abstracts of Papers of the American Chemical Society* **242** (2011).

130 Ewing, C. S. *et al.* Structural and Electronic Properties of Pt13 Nanoclusters on Amorphous Silica Supports. *The Journal of Physical Chemistry C* **119**, 2503-2512, doi:10.1021/jp5105104 (2015).

131 Goldsmith, B. R., Sanderson, E. D., Bean, D. & Peters, B. Isolated catalyst sites on amorphous supports: A systematic algorithm for understanding heterogeneities in structure and reactivity. *Journal of Chemical Physics* **138**, doi:10.1063/1.4807384 (2013).

132 Cuenya, B. R. Synthesis and catalytic properties of metal nanoparticles: Size, shape, support, composition, and oxidation state effects. *Thin Solid Films* **518**, 3127-3150, doi:10.1016/j.tsf.2010.01.018 (2010).

133 Garnier, A., Sall, S., Garin, F., Chetcuti, M. J. & Petit, C. Site effects in the adsorption of carbon monoxide on real 1.8 nm Pt nanoparticles: An Infrared investigation in time and temperature. *Journal of Molecular Catalysis a-Chemical* **373**, 127-134, doi:10.1016/j.molcata.2013.02.029 (2013).

134 Moroz, E. M., Kriventsov, V. V. & Kochubei, D. I. EuroPt-1 catalyst: Radial distribution of electron density X-ray diffraction and EXAFS studies. *Journal of Structural Chemistry* **50**, 1082-1087, doi:10.1007/s10947-009-0159-z (2009).

135 Henkelman, G., Arnaldsson, A. & Jonsson, H. A fast and robust algorithm for Bader decomposition of charge density. *Computational Materials Science* **36**, 354-360, doi:10.1016/j.commatsci.2005.04.010 (2006).

136 Tang, W., Sanville, E. & Henkelman, G. A grid-based Bader analysis algorithm without lattice bias. *Journal of Physics-Condensed Matter* **21**, doi:10.1088/0953-8984/21/8/084204 (2009).

137 Mulliken, R. S. ELECTRONIC POPULATION ANALYSIS ON LCAO-MO MOLECULAR WAVE FUNCTIONS .4. BONDING AND ANTIBONDING IN LCAO AND VALENCE-BOND THEORIES. *Journal of Chemical Physics* **23**, 2343-2346, doi:10.1063/1.1741877 (1955).

138 Pacchioni, G. Electronic interactions and charge transfers of metal atoms and clusters on oxide surfaces. *Physical Chemistry Chemical Physics* **15**, 1737-1757, doi:10.1039/c2cp43731g (2013).

139 Shekhar, M. *et al.* Size and Support Effects for the Water-Gas Shift Catalysis over Gold Nanoparticles Supported on Model Al2O3 and TiO2. *Journal of the American Chemical Society* **134**, 4700-4708, doi:10.1021/ja210083d (2012).

140 Williams, W. D. *et al.* Metallic Corner Atoms in Gold Clusters Supported on Rutile Are the Dominant Active Site during Water-Gas Shift Catalysis. *Journal of the American Chemical Society* **132**, 14018-14020, doi:10.1021/ja1064262 (2010).

141 Campbell, C. T. Ultrathin metal films and particles on oxide surfaces: Structural, electronic and chemisorptive properties. *Surface Science Reports* **27**, 1-111, doi:10.1016/s0167-5729(96)00011-8 (1997).

142 Zheng, Z., Wang, X., Liu, J., Xiao, J. & Hu, Z. Si doping influence on the catalytic performance of Pt/TiO2 mesoporous film catalyst for low-temperature methanol combustion. *Applied Surface Science* **309**, 144-152, doi:http://dx.doi.org/10.1016/j.apsusc.2014.04.208 (2014).

143 Zheng, G. *et al.* Parameter Calibration of Transition-Metal Elements for the Spin-Polarized Self-Consistent-Charge Density-Functional Tight-Binding (DFTB) Method: Sc, Ti, Fe, Co, and Ni. *Journal of chemical theory and computation* **3**, 1349-1367, doi:10.1021/ct600312f (2007).

144 Lægsgaard, J. & Stokbro, K. Hole Trapping at Al impurities in Silica: A Challenge for Density Functional Theories. *Physical Review Letters* **86**, 2834-2837 (2001).

145 To, J., Sokol, A. A., French, S. A., Kaltsoyannis, N. & Catlow, C. R. A. Hole localization in [AlO4]0 defects in silica materials. *The Journal of Chemical Physics* **122**, 144704, doi:doi:http://dx.doi.org/10.1063/1.1880972 (2005).

146 Roma, G. & Limoge, Y. Density functional theory investigation of native defects in SiO_2: Self-doping and contribution to ionic conductivity. *Physical Review B* **70**, 174101 (2004).

147 Venezia, A. M., Di Carlo, G., Liotta, L. F., Pantaleo, G. & Kantcheva, M. Effect of Ti(IV) loading on CH4 oxidation activity and SO2 tolerance of Pd catalysts supported on silica SBA-15 and HMS. *Applied Catalysis B: Environmental* **106**, 529-539, doi:http://dx.doi.org/10.1016/j.apcatb.2011.06.013 (2011).

148 Nguyen Dinh, M. T. *et al.* Tuning Hydrodesulfurization Active-Phase Dispersion using Optimized Mesoporous Titania-Doped Silica Supports. *ChemCatChem* **6**, 328-338, doi:10.1002/cctc.201300521 (2014).

149 Schwartz, V. *et al.* Structural Investigation of Au Catalysts on TiO2−SiO2 Supports: Nature of the Local Structure of Ti and Au Atoms by EXAFS and XANES. *The Journal of Physical Chemistry C* **111**, 17322-17332, doi:10.1021/jp074426c (2007).

150 Ewing, C. S., Veser, G., McCarthy, J. J., Johnson, J. K. & Lambrecht, D. S. Effect of Support Preparation and Nanoparticle Size on Catalyst-Support Interactions between Pt and Amorphous Silica. *J. Phys. Chem, submitted* (2015).

151 Grimme, S., Antony, J., Ehrlich, S. & Krieg, H. A consistent and accurate ab initio parametrization of density functional dispersion correction (DFT-D) for the 94 elements H-Pu. *Journal of Chemical Physics* **132**, doi:10.1063/1.3382344 (2010).

152 Ewing, C. S. *et al.* Structural and Electronic Properties of Pt-13 Nanoclusters on Amorphous Silica Supports. *Journal of Physical Chemistry C* **119**, 2503-2512, doi:10.1021/jp5105104 (2015).

153 Boyle, B. J., King, E. G. & Conway, K. C. HEATS OF FORMATION OF NICKEL AND COBALT OXIDES (NIO AND COO) OF COMBUSTION CALORIMETRY. *Journal of the American Chemical Society* **76**, 3835-3837, doi:10.1021/ja01643a072 (1954).

154 Chase, M. W., Jr. NIST-JANAF Themochemical Tables, Fourth Edition. *J. Phys. Chem. Ref. Data* **9**, 1-1951 (1998).

155 Komiyama, M. & Shimaguchi, T. Partial reduction of Si(IV) in SiO2 thin film by deposited metal particles: an XPS study. *Surface and Interface Analysis* **32**, 189-192, doi:10.1002/sia.1034 (2001).

156 Venezia, A. M. *et al.* Oxidation of CH4 over Pd supported on TiO2-doped SiO2: Effect of Ti(IV) loading and influence of SO2. *Applied Catalysis B: Environmental* **88**, 430-437, doi:http://dx.doi.org/10.1016/j.apcatb.2008.10.023 (2009).

157 Venezia, A. M. *et al.* Effect of Ti(IV) loading on CO oxidation activity of gold on TiO2 doped amorphous silica. *Applied Catalysis A: General* **310**, 114-121, doi:http://dx.doi.org/10.1016/j.apcata.2006.05.027 (2006).

158 Peters, B. & Scott, S. L. Single atom catalysts on amorphous supports: A quenched disorder perspective. *The Journal of Chemical Physics* **142**, 104708, doi:doi:http://dx.doi.org/10.1063/1.4914145 (2015).

159 Guesmi, H. & Tielens, F. Chromium Oxide Species Supported on Silica: A Representative Periodic DFT Model. *Journal of Physical Chemistry C* **116**, 994-1001, doi:10.1021/jp209680r (2012).

160 Handzlik, J., Grybos, R. & Tielens, F. Structure of Monomeric Chromium(VI) Oxide Species Supported on Silica: Periodic and Cluster DFT Studies. *Journal of Physical Chemistry C* **117**, 8138-8149, doi:10.1021/jp3103035 (2013).

161 Handzlik, J. & Ogonowski, J. Structure of Isolated Molybdenum(VI) and Molybdenum(IV) Oxide Species on Silica: Periodic and Cluster DFT Studies. *Journal of Physical Chemistry C* **116**, 5571-5584, doi:10.1021/jp207385h (2012).

162 Iwasawa, Y. & Hamamura, H. MECHANISM FOR INITIAL CARBENE FORMATION IN OLEFIN METATHESIS OVER FIXED MO CATALYSTS. *Journal of the Chemical Society-Chemical Communications*, 130-132, doi:10.1039/c39830000130 (1983).

163 Iwasawa, Y., Ichinose, H., Ogasawara, S. & Soma, M. OLEFIN METATHESIS OVER WELL-DEFINED ACTIVE FIXED MOLYBDENUM CATALYSTS - STRUCTURE AND OXIDATION-STATE OF THE ACTIVE-SITE AND REACTION-MECHANISM. *Journal of the Chemical Society-Faraday Transactions I* **77**, 1763-1777, doi:10.1039/f19817701763 (1981).

164 Iwasawa, Y., Kubo, H. & Hamamura, H. OLEFIN METATHESIS OVER AL2O3-ATTACHED OR SIO2-ATTACHED MOLYBDENUM CATALYSTS - ACTIVE STRUCTURES AND MECHANISM FOR INITIAL CARBENE FORMATION. *Journal of Molecular Catalysis* **28**, 191-208, doi:10.1016/0304-5102(85)87028-0 (1985).

165 Bell, A. T. Single iron sites for catalytic, nonoxidative conversion of methane. *Science China-Chemistry* **57**, 923-923, doi:10.1007/s11426-014-5148-1 (2014).

166 Guo, X. G. *et al.* Direct, Nonoxidative Conversion of Methane to Ethylene, Aromatics, and Hydrogen. *Science* **344**, 616-619, doi:10.1126/science.1253150 (2014).

167 Peters, B. & Scott, S. L. Single atom catalysts on amorphous supports: A quenched disorder perspective. *Journal of Chemical Physics* **142**, doi:10.1063/1.4914145 (2015).

168 Guesmi, N., Grybos, R., Handzlik, J. & Tielens, F. Characterization of molybdenum monomeric oxide species supported on hydroxylated silica: a DFT study. *Physical Chemistry Chemical Physics* **16**, 18253-18260, doi:10.1039/c4cp02296c (2014).

169 Grimme, S. Semiempirical GGA-type density functional constructed with a long-range dispersion correction. *Journal of Computational Chemistry* **27**, 1787-1799, doi:10.1002/jcc.20495 (2006).

170 Ding, H., Ray, K. G., Ozolins, V. & Asta, M. Structural and vibrational properties of alpha-MoO3 from van der Waals corrected density functional theory calculations. *Physical Review B* **85**, doi:10.1103/PhysRevB.85.012104 (2012).

171 Zhuravlev, L. T. SURFACE CHARACTERIZATION OF AMORPHOUS SILICA - A REVIEW OF WORK FROM THE FORMER USSR. *Colloids and Surfaces a-Physicochemical and Engineering Aspects* **74**, 71-90, doi:10.1016/0927-7757(93)80399-y (1993).

172 Bishop, K. J. M., Wilmer, C. E., Soh, S. & Grzybowski, B. A. Nanoscale Forces and Their Uses in Self-Assembly. *Small* **5**, 1600-1630, doi:10.1002/smll.200900358 (2009).

173 Tiede, K. *et al.* Detection and characterization of engineered nanoparticles in food and the environment. *Food Additives and Contaminants Part a-Chemistry Analysis Control Exposure & Risk Assessment* **25**, 795-821, doi:10.1080/02652030802007553 (2008).

174 Campelo, J. M., Luna, D., Luque, R., Marinas, J. M. & Romero, A. A. Sustainable Preparation of Supported Metal Nanoparticles and Their Applications in Catalysis. *Chemsuschem* **2**, 18-45, doi:10.1002/cssc.200800227 (2009).

175 Kim, B. H., Hackett, M. J., Park, J. & Hyeon, T. Synthesis, Characterization, and Application of Ultrasmall Nanoparticles. *Chemistry of Materials* **26**, 59-71, doi:10.1021/cm402225z (2014).

176 Caswell, K. K., Bender, C. M. & Murphy, C. J. Seedless, surfactantless wet chemical synthesis of silver nanowires. *Nano Letters* **3**, 667-669, doi:10.1021/nl0341178 (2003).

177 Henglein, A. & Giersig, M. Formation of colloidal silver nanoparticles: Capping action of citrate. *Journal of Physical Chemistry B* **103**, 9533-9539, doi:10.1021/jp9925334 (1999).

178 Jin, R. C. *et al.* Photoinduced conversion of silver nanospheres to nanoprisms. *Science* **294**, 1901-1903, doi:10.1126/science.1066541 (2001).

179 Mpourmpakis, G. & Vlachos, D. G. Insights into the early stages of metal nanoparticle formation via first-principle calculations: the roles of citrate and water. *Langmuir* **24**, 7465-7473, doi:10.1021/la800135s (2008).

180 Mpourmpakis, G. & Vlachos, D. G. Growth Mechanisms of Metal Nanoparticles via First Principles. *Physical Review Letters* **102**, doi:10.1103/PhysRevLett.102.155505 (2009).

181 Munro, C. H., Smith, W. E., Garner, M., Clarkson, J. & White, P. C. CHARACTERIZATION OF THE SURFACE OF A CITRATE-REDUCED COLLOID OPTIMIZED FOR USE AS A SUBSTRATE FOR SURFACE-ENHANCED RESONANCE RAMAN-SCATTERING. *Langmuir* **11**, 3712-3720, doi:10.1021/la00010a021 (1995).

182 Pillai, Z. S. & Kamat, P. V. What factors control the size and shape of silver nanoparticles in the citrate ion reduction method? *Journal of Physical Chemistry B* **108**, 945-951, doi:10.1021/jp037018r (2004).

183 Redmond, P. L., Wu, X. & Brus, L. Photovoltage and photocatalyzed growth in citrate-stabilized colloidal silver nanocrystals. *Journal of Physical Chemistry C* **111**, 8942-8947, doi:10.1021/jp0710436 (2007).

184 Sun, X. M. & Li, Y. D. Cylindrical silver nanowires: Preparation, structure, and optical properties. *Advanced Materials* **17**, 2626-+, doi:10.1002/adma.200500957 (2005).

185 Sun, Y. G., Gates, B., Mayers, B. & Xia, Y. N. Crystalline silver nanowires by soft solution processing. *Nano Letters* **2**, 165-168, doi:10.1021/nl010093y (2002).

186 Sun, Y. G., Mayers, B., Herricks, T. & Xia, Y. N. Polyol synthesis of uniform silver nanowires: A plausible growth mechanism and the supporting evidence. *Nano Letters* **3**, 955-960, doi:10.1021/nl034312m (2003).

187 Sun, Y. G., Mayers, B. & Xia, Y. N. Transformation of silver nanospheres into nanobelts and triangular nanoplates through a thermal process. *Nano Letters* **3**, 675-679, doi:10.1021/nl034140t (2003).

188 Sun, Y. G. & Xia, Y. N. Shape-controlled synthesis of gold and silver nanoparticles. *Science* **298**, 2176-2179, doi:10.1126/science.1077229 (2002).

189 Wiley, B., Sun, Y. G., Mayers, B. & Xia, Y. N. Shape-controlled synthesis of metal nanostructures: The case of silver. *Chemistry-a European Journal* **11**, 454-463, doi:10.1002/chem.200400927 (2005).

190 Brust, M., Walker, M., Bethell, D., Schiffrin, D. J. & Whyman, R. SYNTHESIS OF THIOL-DERIVATIZED GOLD NANOPARTICLES IN A 2-PHASE LIQUID-LIQUID SYSTEM. *Journal of the Chemical Society-Chemical Communications*, 801-802, doi:10.1039/c39940000801 (1994).

191 Chen, H. *et al.* A Surfactant-Free Strategy for Synthesizing, and Processing Intermetallic Platinum-Based Nanoparticle Catalysts. *Journal of the American Chemical Society* **134**, 18453-18459, doi:10.1021/ja308674b (2012).

192 Stober, W., Fink, A. & Bohn, E. CONTROLLED GROWTH OF MONODISPERSE SILICA SPHERES IN MICRON SIZE RANGE. *Journal of Colloid and Interface Science* **26**, doi:10.1016/0021-9797(68)90272-5 (1968).

193 Dracinsky, M., Benda, L. & Bour, P. Ab initio modeling of fused silica, crystal quartz, and water Raman spectra. *Chemical Physics Letters* **512**, 54-59, doi:10.1016/j.cplett.2011.06.077 (2011).

194 Grimley, D. I., Wright, A. C. & Sinclair, R. N. Neutron-scattering from vitreous silica. 4. Time-of-flight diffraction. *J. Non-Cryst. Solids* **119**, 49-64, doi:10.1016/0022-3093(90)90240-m (1990).

195 Mozzi, R. L. & Warren, B. E. STRUCTURE OF VITREOUS SILICA. *Journal of Applied Crystallography* **2**, 164-&, doi:10.1107/s0021889869006868 (1969).

196 Da Silva, J. R. G., Pinatti, D. G., Anderson, C. E. & Rudee, M. L. A refinement of the structure of vitreous silica. *Philos. Mag.* **31**, 713-717 (1975).